

**Experimental Characterization of Scale Model Wave Energy
Converter Hydrodynamics**

by

Kendra Mercedes Sunshine McCullough
B.Eng., University of Victoria, 2005

A Dissertation Submitted in Partial Fulfillment
of the Requirements for the Degree of

MASTER OF APPLIED SCIENCE

in the Department of Mechanical Engineering

© Kendra Mercedes Sunshine McCullough, 2013

University of Victoria

All rights reserved. This thesis may not be reproduced in whole or in part, by photocopy or other means, without the permission of the author.

Supervisory Committee

Experimental Characterization of Scale Model Wave Energy Converter Hydrodynamics

by

Kendra Mercedes Sunshine McCullough
B.Eng., University of Victoria, 2005

Supervisory Committee

Dr. Brad Buckham, Department of Mechanical Engineering

Co-Supervisor

Dr. Peter Oshkai, Department of Mechanical Engineering

Co- Supervisor

Dr. Peter Wild, Department of Mechanical Engineering

Departmental Member

Abstract

Supervisory Committee

Dr. Brad Buckham, Department of Mechanical Engineering

Co-Supervisor

Dr. Peter Oshkai, Department of Mechanical Engineering

Co-Supervisor

Dr. Peter Wild, Department of Mechanical Engineering

Departmental Member

A prototype point absorber style wave energy converter has been proposed for deployment off the West coast of Vancouver Island near the remote village of Hotsprings Cove in Hesquiaht Sound; a site identified as having significant wave energy potential. The proposed design consists of two components, a long unique cylindrical spar and a concentric toroid float. To serve ongoing wave energy converter (WEC) dynamics modelling and control research in support of that project, an experimental facility for small scale physical model testing is desired at UVIC. In the immediate term, the facility could be used to determine the hydrodynamic coefficients over a range of wave frequencies. Refined estimates of the hydrodynamic coefficients would be exploited in the optimisation of the WEC geometry. To date, WEC research at UVIC has neglected the frequency dependence of the hydrodynamic coefficients, relying on limited experimental results to provide a single frequency invariant set of coefficient estimates.

The research detailed in this thesis was focused on developing an experimental testing system to characterize the hydrodynamic coefficients for added mass and damping for a

point absorber type wave energy converter. The point absorber design consists of two main components whose geometry interacts with the surrounding fluid, the deep cylindrical spar and concentric toroidal float. The design is representative of the technology being considered at Hesquiaht Sound. An initial batch of experiments was also conducted for a scale model of one design of the wave energy converter. The program of study included the design and manufacture of the wave tank and the WEC scale model, a validation of the facility against existing hydrodynamic coefficient predictions for simple floating geometries, and hydrodynamic characterization experiments in which the lumped parameter hydrodynamic coefficients were identified for the scaled model WEC and comparison of the results to existing simplified models at UVIC.

The development of the test facility first involved ascertaining and accommodating the constraints of an existing fluid tunnel that had to accommodate a wave maker and the physical WEC models. The test facility incorporated a low friction mechanism to maintain single degree of freedom motion, heave, for the WEC model motions. A forcing mechanism was created for the generation of sinusoidal, linear, oscillations of the model; a piston style wave maker was also constructed for the generation of sinusoidal, linear waves. Measurement transducers for the wave regime, hydrodynamic loading and the model motion were installed including: a wave gauge, a torsional load cell and a 3D camera, respectively. The facility is designed to accommodate four different experiments: a naturally damped oscillation in quiescent fluid, a forced oscillation of the model components in quiescent fluid, free oscillations driven by a generated wave field, and fixed model tests in a generated wave field. The quiescent fluid methods were used to identify the reactionary forces, whereas the wave field tests allow for the identification of the excitation force coefficients. Three model arrangements were considered: a simple cylinder for validation purposes, the WEC spar alone, and the spar with a fixed or motionless float. The wave regime generated in the 3rd and 4th tests were a scale replication of wave data previously identified at UVIC for the Hesquiaht Sound WEC deployment site location. To determine the coupling effects

between components of the scale model WEC, the spar hull was tested in isolation and with the outer concentric float present.

The experiment established that the test facility is sufficient for the desired scale range for the three methods tested, based on comparison with an established numerical results for the simple cylinder geometry. The experimental data indicates that the numerical model utilized for simple cylinders cannot be used for the unique spar geometry. The non-dimensional lumped added mass hydrodynamic coefficients for the spar in the presence of the float were found to be overall lower than when the float is absent, although different trends were identified for wave field versus quiescent fluid. The non-dimensional lumped damping hydrodynamic coefficient was higher for the spar alone configuration than the spar-float model configuration in the wave field experiments but lower in quiescent fluid.

Table of Contents

Supervisory Committee	ii
Abstract	iii
Table of Contents	vi
List of Tables	x
List of Figures	xii
Chapter 1: Introduction.....	1
1.1 Wave Energy.....	1
1.2 Wave Energy Conversion Technology	2
1.2.1 WEC Technology: Conversion Classes	2
1.2.2 WEC Technology: Historical Context	4
1.3 Two Body Point Absorbers.....	7
1.4 Point Absorber Hydrodynamics Modelling	12
1.5 Hydrodynamic Characterization for Point Absorbers.....	14
1.6 Research Objectives.....	15
1.7 Thesis Overview	17
Chapter 2: Equation of Motion and Hydrodynamic Coefficients.....	19
2.1 Overview.....	19
2.2 Wave Kinematics and Small Body Approximation.....	19
2.3 Floating Body Kinetics	24
2.3.1 Wave Excitation Force.....	27

2.3.2	WEC Reaction Forces.....	29
2.4	Equations of motion.....	31
2.4.1	Equation of motion of a 1-DOF system.....	31
2.4.2	Equation of motion of a 2-DOF system.....	32
2.5	Closing.....	35
Chapter 3:	Experimental Considerations and Constraints.....	38
3.1	Overview.....	38
3.2	The Fluid Tunnel.....	38
3.3	Environmental Conditions	42
3.3.1	Hesquiaht Sound - Offshore Conditions.....	43
3.3.2	Hesquiaht Sound – Near Shore Conditions	44
3.4	Full Scale WEC Prototype Physical Parameters.....	47
3.5	WEC Model Scaling.....	49
3.5.1	Dynamic Scaling Parameters	50
3.5.2	Choice of WEC Spar Geometric Scaling factor	52
3.5.3	Enforcing WEC Spar Dynamic Scaling.....	53
Chapter 4:	Experimental Apparatus Specification	57
4.1	Wave Maker Specifications	57
4.2	Scale Model WEC Forcing Mechanism	63
4.3	Measurements and Instrumentation	67
4.3.1	Force Measurement.....	67
4.3.2	Displacement Measurement.....	68
4.3.3	Wave Measurement	68
4.4	Experimental Procedures	69

4.4.1	Natural Oscillations in Quiescent Fluid.....	69
4.4.2	Forced Oscillations in Quiescent fluid.....	74
4.4.3	Wave Excitation Forces on a fixed body	77
4.4.4	Reaction Forces of a Free Body in Waves.....	81
4.5	Non-dimensional Hydrodynamic Coefficients	82
Chapter 5:	Experimental Results	83
5.1	Overview.....	83
5.2	Wave Maker Validation.....	84
5.3	Simple Cylinder Model Tests	88
5.3.1	Free Oscillations in Quiescent Fluid.....	89
5.3.2	Forced Oscillations in Quiescent Fluid.....	90
5.3.3	Fixed Model in Wave Field	91
5.3.4	Free Model in Wave Field	92
5.4	Spar-Only Model Configuration.....	94
5.4.1	Free Oscillations in Quiescent Fluid.....	95
5.4.2	Forced Oscillations in Quiescent Fluid.....	96
5.4.3	Fixed Model in Wave Field	98
5.4.4	Free Model in Wave Field	99
5.5	Spar-Float Model Configuration.....	101
5.5.1	Free Oscillations in Quiescent Fluid.....	103
5.5.2	Forced Oscillations in Quiescent Fluid.....	103
5.5.3	Fixed Model in Wave Field	105
5.5.4	Free Model in Wave Field	107
5.6	Spar-Only model to Spar-Float model Comparisons.....	109

5.6.1	Free Oscillations in Quiescent Fluid.....	109
5.6.2	Forced Oscillations in Quiescent Fluid.....	110
5.6.3	Fixed Model in Wave Field	111
5.6.4	Free Model in Wave Field	112
5.7	Reaction Force Comparison: Forced in Quiescent Fluid vs. Free in Wave Field	113
Chapter 6:	Conclusions and Recommendations	117
6.1	Test Setup.....	117
6.1.1	Wave Maker Operation.....	117
6.1.2	Model Guides and Forcing Mechanism.....	117
6.1.3	Validation of Facility and Experimental Methods.....	119
6.2	Hydrodynamic Coefficients of Point Absorbing Wave Energy Converter Model Geometry	120
6.3	Spar Design Considerations.....	121
6.3.1	Geometric Effects: Spar Versus cylinder.....	121
6.3.2	Geometric Effects: Combination of spar and float	122
6.3.3	Frequency and Amplitude Effects	123
Bibliography	125
Appendix A	131

List of Tables

Table 1 – Experimentally Determined 1-DOF Spar Excitation Coefficients	35
Table 2 - Experimentally Determined 1-DOF Spar Reaction Coefficients	35
Table 3 - 1-DOF Float Excitation Coefficients (not experimentally evaluated in this research).....	36
Table 4 - 1-DOF Float Reaction Coefficients (not experimentally evaluated in this research).....	36
Table 5 - Experimentally Determined 2-DOF Spar Excitation Coefficients	36
Table 6 - Experimentally Determined 2-DOF Spar Reaction Coefficients	36
Table 7 - 2-DOF Float Excitation Coefficients (not experimentally evaluated in this research).....	37
Table 8 - 2-DOF Float Reaction Coefficients (not experimentally evaluated in this research).....	37
Table 9 - Wave Breaking: Deep Water.....	42
Table 10 - Wave Breaking: Shallow Water	42
Table 11 - Deployment Site Locations	45
Table 12 Scaled Geometry Values.....	53
Table 13 - Froude Scale Factors	55
Table 14 - Froude Scaled Wave Regime	56
Table 15 - Stroke requirements(mm) over range of wave heights(m) and periods(s)	60

Table 16 - Measurement Tool Specifications	69
Table 17 – Natural Oscillation Experimental Reaction Coefficients.....	73
Table 18 – Forced Oscillation Experimental Hydrodynamic Coefficients.....	77
Table 19 – Fixed Body in Wave Experimental Excitation Coefficients.....	81
Table 20 – Free Oscillation of Body in Wave Experimental Reaction Coefficients	82
Table 21 - Experimentally determined hydrodynamic coefficients for a simple cylinder	88
Table 22 - Experimentally determined hydrodynamic coefficients for a spar-only model	95
Table 23 - Experimentally determined hydrodynamic coefficients for a spar-float model	102

List of Figures

Figure 1 - A summary of the wave excited class of WEC technologies, where the wave direction is left to right.....	3
Figure 2 – Sample century old WEC patents.....	6
Figure 3 - WEC Type by functionality	7
Figure 4 - the OPT PowerBuoy.	8
Figure 5 – WaveBob	9
Figure 6 - SWELS Unit Diagram showing the reaction mass and ballscrew operation and connections.....	11
Figure 7 - Wave Parameter Definitions	20
Figure 8 - Definition of floating body motions.....	25
Figure 9 - Mechanical Oscillator Analogy of Floating Body.	26
Figure 10 - UVIC fluid tunnel	39
Figure 11 - Test Facility Length Constraints	40
Figure 12 – Hesquiaht Sound (a) Location of Hesquiaht Sound on Vancouver Island (b) Wave Energy Converter Test Site Location in Hesquiaht Sound.....	43
Figure 13 - Bathymetric data in Hesquiaht Sound and selected near-shore sites A-E. ..	45
Figure 14 - H_s , T_p and θ_p offshore and for selected near-shore points A-E	46
Figure 15 - SyncWave Point Absorbing WEC	48

Figure 16 - WEC Prototype Design Parameters	49
Figure 17 - Wave Maker Types.	58
Figure 18 - Modified Piston Flap Wave maker [38].....	59
Figure 19 - Piston Wave-maker: Wave Height to Stroke ratios versus relative depths..	60
Figure 20 - Piston Wave-maker: Dimensionless mean power as a function of water depth.....	61
Figure 21 - Volume Displacement Box and Piston Face Motion	62
Figure 22 - Wave Maker 3D Model.....	62
Figure 23 - Wave Make Setup	63
Figure 24 - WEC Model Mount and Forcing Mechanism.....	65
Figure 25 - Combined view of linear guides and WEC Model with Linear Actuator..	66
Figure 26 – Scale model WEC Forcing Mechanism	66
Figure 27 - Load Cell Arrangement.....	67
Figure 28 - Natural Decay Curve for a sample spar test.....	73
Figure 29 – Model Displacement and Force data used in identification of Reaction Force coefficients.....	74
Figure 30 - VisualEyez: Displacement	75
Figure 31 - VisualEyez: Velocity	75
Figure 32 - VisualEyez: Acceleration.....	76
Figure 33 - Load Cell Torsion Data.....	76

Figure 34 - Wave Gauge Data	78
Figure 35 - Calculated Wave Free Surface Velocity	79
Figure 36 - Calculated Wave Free Surface Acceleration.....	79
Figure 37 - Wave Field Experimental Setup.....	80
Figure 38 – Small scale model configurations.....	84
Figure 39 - Wave Form at 1.6rad/s	86
Figure 40 - Wave Form at 3.7 rad/s	87
Figure 41 - Wave Form at 6.8 rad/s	87
Figure 42 - Naturally Damped, Cylinder in Quiescent Fluid.....	89
Figure 43 - Hydrodynamic Coefficients of Free cylinder in Quiescent Fluid.	90
Figure 44 - Reaction Coefficients of Forced Cylinder in Quiescent Fluid.....	91
Figure 45 - Excitation Coefficients of Fixed Cylinder in Wave Field.....	92
Figure 46 - Reaction Coefficients of Free Simple Cylinder in Wave Field.....	93
Figure 47 - Hydrodynamic Coefficients of Free Spar-Only model in Quiescent Fluid..	96
Figure 48 - Reaction Coefficients of Forced Spar-Only model in Quiescent Fluid	97
Figure 49 - Forced Spar-Only in Quiescent Fluid: Added Mass	98
Figure 50 - Forced Spar-Only in Quiescent Fluid: Damping Coefficient	98
Figure 51 - Excitation Coefficients of Fixed Spar-only model in Wave Field.....	99
Figure 52 - Reaction Coefficients of Free Spar-Only model in Wave Field	100

Figure 53 - Sample of Experimental Errors: Spar-only model at 2.6rad/s	101
Figure 54 - Spar and Float combination	102
Figure 55 – Hydrodynamic Coefficients for Free Spar-Float model in Quiescent Fluid	103
Figure 56 - Reaction Coefficients for Forced Spar-Float model in Quiescent Fluid....	104
Figure 57 - Forced Spar-Float in Quiescent Fluid: Added Mass	104
Figure 58 - Forced Spar-Float in Quiescent Fluid: Damping Coefficient	105
Figure 59 - Excitation Coefficients of Fixed Spar-Float model in Wave Field.....	106
Figure 60 - Fixed Spar-float model in Waves: Added mass	106
Figure 61 - Fixed Spar-float model in Waves: damping coefficient	107
Figure 62 - Reaction Coefficients of Free Spar-Float model in Wave Field.....	108
Figure 63 - Free Spar-Float in waves: Added Mass	108
Figure 64 - Hydrodynamic Coefficients for Spar-only model and Spar-float model configurations for free, naturally damped system in Quiescent Fluid.....	110
Figure 65 - Hydrodynamic Coefficients for Spar-only model and Spar-float model configurations for forced model in Quiescent Fluid.....	111
Figure 66 - Hydrodynamic Coefficients for Spar-only model and Spar-float model configurations for fixed model in Wave Field.....	112
Figure 67 - Hydrodynamic Coefficients for Spar-only model and Spar-float model configurations for Free body tests in Wave Field.....	113
Figure 68 – Reactive Hydrodynamic Coefficients of Cylinder, comparison between forced and free in wave field tests	114

Figure 69 – Reactive Hydrodynamic Coefficients of Spar-only model, comparison between forced and free in wave field tests	115
Figure 70 – Reactive Hydrodynamic Coefficient of Spar with float, comparison between forced and free in wave field tests	115
Figure 71 - Wave Form at 1.6rad/s	131
Figure 72 - Wave Form at 1.9rad/s	131
Figure 73 - Wave Form at 2.3 rads/s.....	132
Figure 74 - Wave Form at 2.6rad/s	132
Figure 75 - Wave Form at 3.0 rad/s	133
Figure 76 - Wave Form at 3.3 rad/s	133
Figure 77 - Wave Form at 3.7 rad/s	134
Figure 78 - Wave Form at 4.0 rad/s	134
Figure 79 - Wave Form at 4.4rad/s	135
Figure 80 - Wave Form at 4.7 rad/s	135
Figure 81 - Wave form at 5.4 rad/s	136
Figure 82 - Wave Form at 5.8 rad/s	136
Figure 83 - Wave Form at 6.3 rad/s	137
Figure 84 - Wave Form at 6.8 rad/s	137

Chapter 1: Introduction

1.1 Wave Energy

Energy is one of the most significant determining factors in one's quality of life in the modern world. It is a necessary component in the delivery of our basic needs such as food, shelter and water. It is widely recognized that in the near future there will no longer be a sufficient supply of conventional energy sources. At present, most existing energy conversion technologies are not considered environmentally adequate or sustainable. At a recent workshop for the Natural Resources Canada Marine Renewable Energy Technology Roadmap Project it was stated that energy demands will exceed conventional hydrocarbon supplies in the next 10-40 years. Prevailing opinion is that achievement of the "Peak Oil" condition will result in a dramatic increase in the price of energy, as well as instability of that price.¹

To diversify energy supply, scientists and engineers all over the world are investigating methods of extracting, storing and utilizing energy from numerous emerging clean or renewable sources such as wind and hydrogen, while also attempting to optimize or eliminate toxic by-products of conventional extraction from tar sands, coal and internal combustion. All of these areas of research are required if developed societies are going to avoid the negative environmental circumstances that are expected should trends in energy demand remain unchanged. As was stated in the World Energy Outlook 2006 by the International Energy Agency, "The need to curb the growth in fossil-energy demand, to increase geographic and fuel-supply diversity and to mitigate climate-destabilising emissions is more urgent than ever." [1]

In order to meet GHG emission targets of 20% below 2006 levels by 2020, and 60-70% below 2006 by 2050, Canada's federal government committed to a low emission culture with the *Turning the Corner* policy statement [2]. Based on the extent of the Canadian

¹ http://www.oreg.ca/web_documents/vancouver_meeting_summary.pdf accessed 15/01/2012

raw wave energy resource, ocean waves could play a significant role in the nation's pursuit of these targets. The Canadian eastern and western shorelines are estimated to have a wave energy potential of 16.1 GW with shore based technology alone [3].

Wave energy is sometimes referred to as a storage mechanism for solar energy. Waves are mainly generated from wind which in turn is generated from the differential heating of the earth that causes unimpeded air flow across expansive bodies of water. These winds transfer the solar energy to the formation of water waves. The wind speed, fetch, and duration are all major factors in determining the amount of energy transferred from the sun. One of the great benefits of ocean waves is that they can travel long distances very efficiently. Although weather driven resources are unpredictable on a short timescale, waves are a regular and predictable source of energy over a period of days [4].

From [5], one can observe that the Canadian National Roundtable on the Environment and the Economy (NRTEE) suggests that 10GW of wave energy generation will be needed, in an overall renewables portfolio of 70GW supply in order to meet the 60% GHG reduction target. However, while wave energy converters are seen as a promising technology component of a national sustainable energy plan by groups like the NRTEE, it remains one of the least investigated [5]. Although it has been projected that the global energy potential in ocean waves around the world lies between 1-10TW [6], wave energy conversion has not been achieved on a commercial scale and there is no standardized concept for wave energy conversion.

1.2 Wave Energy Conversion Technology

1.2.1 WEC Technology: Conversion Classes

Wave energy converter (WEC) designs can be distinguished by their operational and directional characteristics. Operationally, there are three classes of converters. First, is the oscillating water column class of technology: waves drive free surface oscillations

that directly push or pull air through a Wells turbine to generate electricity. Second, is the overtopping class of device where wave circulation drives fluid into a confined reservoir and water outflow is regulated through an outlet turbine to generate electricity. Lastly, entries in the water activated device class produce electricity from the relative motion of articulated multiple bodies, which are driven by wave excitation forces (viscous, form drag and inertia forces). The wave activated WEC type devices are the most commonly investigated and numerous examples are in various stages of development as they are expected to be the smallest, most efficient and most economical technologies.

The directional behavior, how the wave direction affects performance, can be used to further break apart the wave activated classification. There are three groupings of directional behavior: point absorbers, attenuators and terminators. The attenuator, or surface follower shown in Figure 1(a), is aligned parallel to the dominant wave direction and is made up of long, segmented floating bodies which flex as the waves move past, generating electricity from the motion of the hinges.

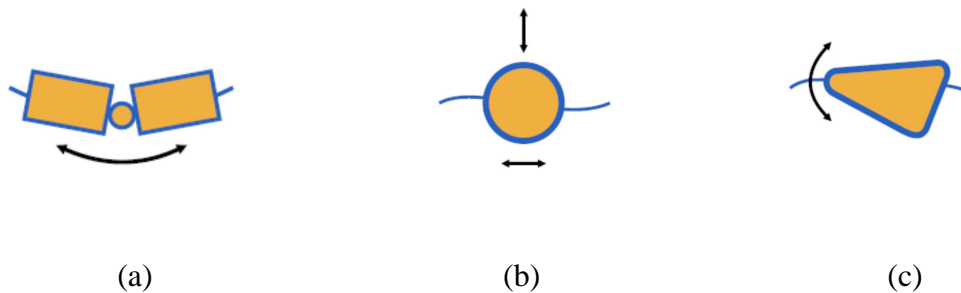


Figure 1 - A summary of the wave excited class of WEC technologies, where the wave direction is left to right.

(a) Attenuators (b) Point Absorbers (c) Terminators

The point absorber, shown in Figure 1(b), is generally small with respect to the wavelengths that compose the wave field, does not depend on wave direction and is therefore omni-directional. A point absorber can operate utilizing various modes of motion, surge and or heave for example, and may be floating or submerged. The

terminator, shown in Figure 1(c), is aligned perpendicularly to the wave field, typically moving back and forth on a hinge with the wave circulation. The motions drive a pump, pushing water to a shore-based hydro-electric power plant.

There is yet to be a convergence on a single type of WEC within the motion activated class as has occurred with other renewable energy technologies. Each potential WEC site, whether offshore, near shore or shore-based, has its own geographical features and its own typical wave characteristics which encourages customization of the WEC design concept. Determining the ideal WEC location is a balancing act between energy potential, and construction and manufacturing costs. For instance, wave energy decreases as it gets closer to shore due to the frictional losses incurred along the seabed. While that observation encourages a move offshore, the long underwater transmission cables required can induce significant energy losses. In addition, one must consider how wave energy is delivered at high energy sites whether offshore or near-shore. If the higher energy capacity realized at an offshore site is due to short concentrated bursts associated with storms, it may require extreme heavy duty design. Or, the converter may need to be shut down eliminating the benefit of the offshore location.

1.2.2 WEC Technology: Historical Context

The concept of capturing wave energy has been investigated for more than 100 years as seen by some early patent drawing shown in Figure 2. Figure 2(a) shows a type of attenuator that is bottom founded, while Figure 2(b) shows a very similar attenuator concept that is reactionless – that is to say it is moored to the ocean floor by compliant lines. Figure 2(c) shows a heaving point absorber that relies on a taut connection to a motor on the seabed.

Circa 2012, there are hundreds of wave energy converter concepts patented around the world, many have made it to a functional prototype stage and have been implemented in all variety of WEC types. Some of the most well-known prototypes are listed in Figure

3 in their respective category. Of the technologies listed, point absorbers have been suggested as the best candidate to win the race to commercial operations [6, 7].

To be economically feasible in the short term, a WEC must be competitive with at least other renewable technology options on the basis of lifetime cost per energy (kW-hr) delivered. The lifetime costs include initial construction, maintenance, and survivability in severe weather [8]. However, given the ambiguity that pervades any discussion of the detailed design and operation of a WEC, accurate estimates of these values are unavailable – especially for sustained operations. As such, projections of these costs are generated based on relatively simple, but available, metrics and device size is the most prevalent of these. As is discussed in the next section, point absorbers are small with respect to the wavelengths of the ocean waves they harvest energy from. As such, this type of WEC potentially requires less material which many believe will lower device fabrication and installation costs. Again based on physical size considerations, point absorbers are potentially less sensitive to extreme weather conditions as they can be designed to function as regular sea buoys by riding atop the waves during extreme weather.

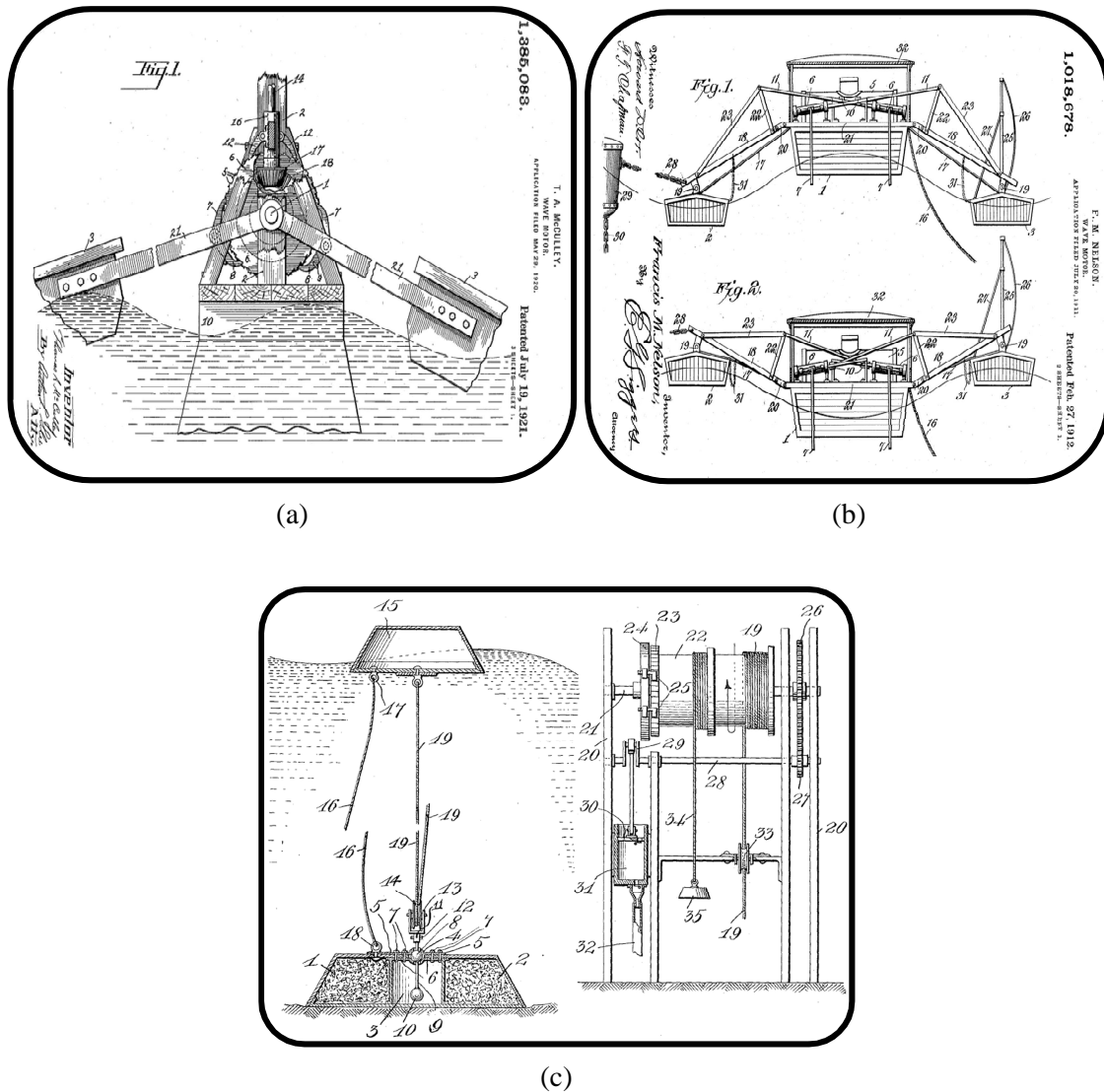


Figure 2 – Sample century old WEC patents.

(a) Patent No. 1,385,083 Dated May 29, 1920. Bottom founded attenuator, energy conversion through wave generated motion (b) Patent No. 1,018,678 Dated July 20, 1911. Moored attenuator, energy conversion through relative motion of floating bodies, this is a two body device that does not rely on taut mooring line connection to the seabed. (c) Patent No. 819,006 Dated April 24, 1906. Heaving point absorber, energy conversion through wave generated motion of floating body to bottom fixed motor.

The three classes are shown in Figure 3 including a breakout of existing design concepts. The activated bodies class of WEC including point absorbers is highlighted.

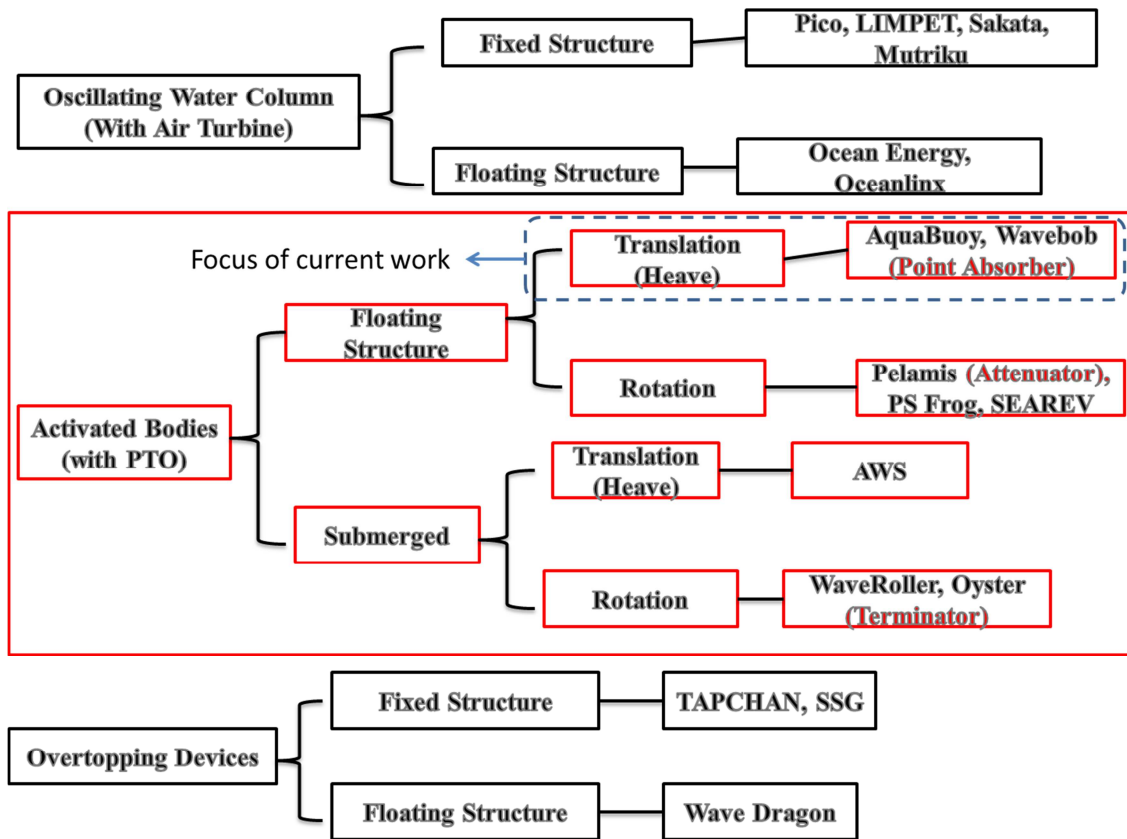


Figure 3 - WEC Type by functionality

1.3 Two Body Point Absorbers

In the Wave Energy Research Group at the University of Victoria, the two-body point absorber type of wave activated WEC is being studied in the context of servicing coastal off-grid communities on the West Coast of Vancouver Island. The two-body point absorber design is a conventional two-body vertically oriented heaving point absorber. A two-body point absorber differs from a single-body point absorber in the sense that it is usually only loosely moored to the seabed and only depends on its two bodies relative reactions to the wave regime, and does not depend on its motion relative to the seabed as shown in Figure 2 (b). Commercial examples of two-body point absorber concept are embodied in the OPT PowerBuoy², and the Wavebob³ WEC. Figure 4 and Figure 5,

² <http://www.oceanpowertechnologies.com>

respectively, show these two pre-commercial devices. All future references to point absorbers found within this thesis refers to two body heaving devices.

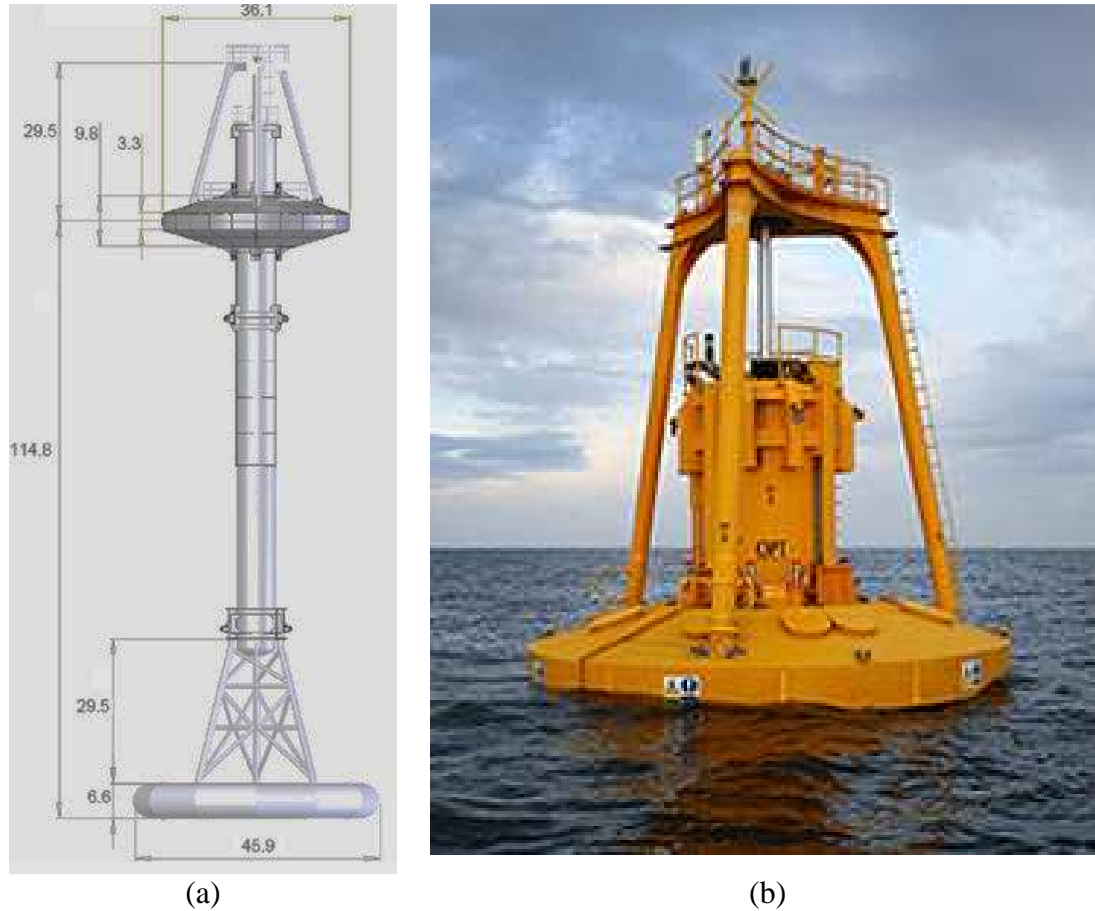


Figure 4 - the OPT PowerBuoy.

(a) A detailed drawing showing the 150kW buoy structure with submerged reaction body, and floating torus. (b) An OPT 150kW demonstration Unit (<http://www.oceanpowertechnologies.com>)

³ <http://wavebob.com/>

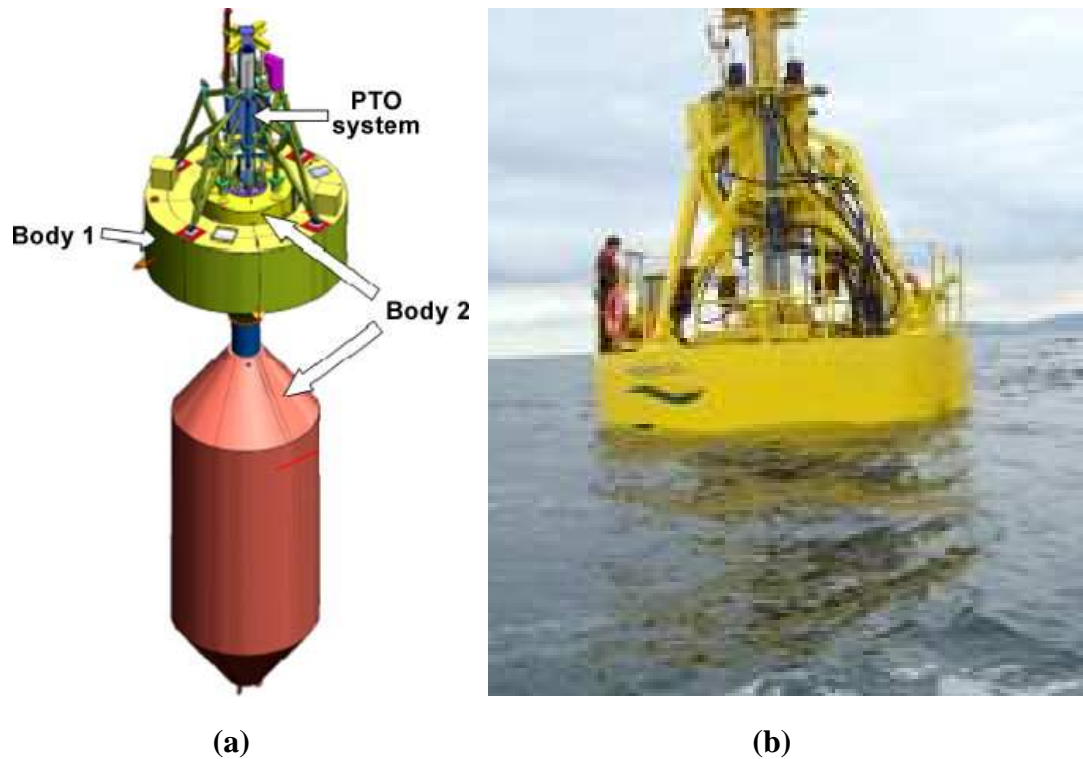


Figure 5 – WaveBob

(a) 3D model showing buoy structure with central body geometry and torus configuration. (b) Demonstration Unit. (<http://wavebob.com>)

Any vertically oriented point absorber design consists of two floating components that drive the energy conversion via their relative motion. The main body, referred to as the spar, consists of a surface piercing deep cylindrical body, with a bulbous component in the deepest section, similar to that of the WaveBob device shown in Figure 5. The secondary body, referred to as the float, is a cylindrical torus set external to the spar similar to that shown on both the OPT PowerBuoy and WaveBob in Figure 4 and Figure 5 respectively. When viewed from above, the point absorber's overall diameter is much smaller than a single wavelength. The ideal motion of the wave energy converter is in the heave or vertical direction only. Electrical energy is converted from the relative motion of the two components through a hydraulic power take off (PTO) connecting the float and the spar.

For point absorber type WECs, the design of the spar hull is crucial to the performance of the wave energy converter. A very low heaving natural frequency is required for the spar in order to ensure that, in general, the spar motion is phase shifted from that of the free surface as much as possible. If the float is designed to maximize wave following behavior, by employing a high buoyant stiffness and a very small total float mass, relative travel between the bodies will be encouraged. While it is simple to devise a float structure that has very good wave following behaviour, achieving a sufficient lag in the spar motion is difficult and a range of strategies exist on how to maximize the relative motion of the float and spar over sufficiently wide ranges of wave frequencies. Control of a typical point absorber is based on adjusting the mechanical impedance of the PTO connected between the spar and the float in a manner that increases power conversion. While it has been shown that a PTO must exhibit a specific inertia, stiffness and viscous damping characteristic to achieve optimal energy conversion for a single regular wave [9, 10], the PTO is most often modeled with just an effective viscosity. Almost all current investigations in PTO control for wave activated point absorbers consider the geometry of the spar and float, and hence the hydrodynamic coefficients of the spar and float to be fixed. Examples of recent research in WEC PTO control include [11, 12, 13].

At UVic, a departure from the conventional point absorber design is being considered. Control of the UVic point absorber concept is based on the continuous adjustment of the PTO viscosity and the inertia of an elastically supported internal mass. The internal reaction mass system, referred to as SWELS, can raise/lower the spar natural frequency in accordance with observed changes in the frequency of the waves at the deployment site. Changes in the point absorber transient behaviour produced by SWELS should increase the tendency for relative spar-float motions which is then exploited, in the context of power conversion, by the use of larger PTO viscosities than were previously possible.

The SWELS unit, shown in Figure 6 consists of a mass and spring system which is kinematically coupled to a ball screw which is rigidly connected to a series of pitching

rigid masses that resemble a fly-ball governor. By varying the pitch angle of the rigid masses, the rotational inertia of the ball screw assembly can be continuously changed. The inertia changes induce continuous changes in the natural frequencies of the spar-reaction mass heave oscillations. By changing the natural frequency of oscillation with respects to a fixed wave frequency, the tendency for the spar to lag the float can be directly altered. As such, the SWELS system could be used to affect the relative travel between the spar and the float.

The design and functionality of the SWELS unit is described in detail in [14].

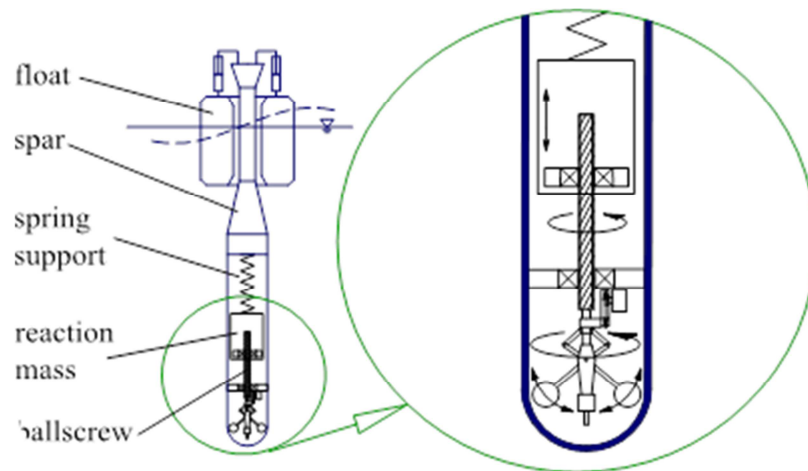


Figure 6 - SWELS Unit Diagram showing the reaction mass and ballscrew operation and connections.

Regardless of the control mechanism(s) used, or whether the focus of the control system designer is irregular seas or a regular (monochromatic) wave, the design of a point absorber PTO controller relies on an accurate hydrodynamic model of the float and spar hydrodynamics. There are drastic differences between the structures of the spars seen in Figure 4 through

Figure 6 and these physical differences translate to marked hydrodynamic coefficients and operating principles for each concept. For example, in Figure 4 (a) one can see that OPT uses a large braking plate at the bottom of the spar in an attempt to keep it

stationary. Contrary to that concept, the UVic investigated device relies on the added mass and radiation forces to be much smaller in order for the SWELS influenced spar oscillations to occur. Further complicating the search for an optimal point absorber control strategy is that the hydrodynamic coefficients of both devices are sensitive to the frequencies of the wave activation forces.

The contrast between the OPT and UVic concepts illustrates an underlying problem in the field of optimal point absorber control; the pursuit of optimal control strategies is occurring across a range of device geometries and any ‘optimal control’ determined through an individual effort is only a ‘local’ optimum – not an optimum across the full, or ‘global’, population of point absorbers. Where the control strategy that produces the most power possible for the given WEC geometry being defined as the most optimal. Globally optimal control methods can only be located if the point absorber WEC hull form and hydrodynamics are considered design variables. In that case, knowledge of how the hydrodynamic coefficients change with geometry must be applied.

1.4 Point Absorber Hydrodynamics Modelling

The most simplified theory for floating bodies often uses Airy wave theory, otherwise known as linear wave theory. Airy wave theory was published by George Biddell Airy in the 19th century and gives a linearized definition of the propagation of gravity waves on the surface of a fluid as described in detail in Chapter 3 “Small-Amplitude Water Wave Theory Formulation and Solution” of [15]. The theory employs assumptions of a constant fluid depth and inviscid, incompressible and irrotational flow, but is used extensively in the analysis of point absorber performance. In conjunction with Airy wave theory, many researchers apply an additional assumption – the small body approximation, sometimes referred to as slender body or long wave assumption. The small body approximation originated in aerodynamics [16], but has gradually been adapted for analysis of marine technologies. The approximation is very well suited to the study of vertically oriented point absorbers as they are slender vertical structures with diameters that are indeed small in comparison to the wavelengths of the ocean

waves that are acting on them. The small body approximation assumes that across a horizontal cross section of the body that the circulation pattern of the fluid in the wave is unaffected [16]. This allows the integration of the pressure over the surface area of the submerged part of the point absorber hull to be greatly simplified.

Numerical modelling of point absorbing wave energy converters most often utilizes both Airy wave theory and the small body approximation to form a point absorber dynamics model. Larsson & Falnes in [17] utilized the small body approximation on a two body system to find that the approximation was valid for a larger range of wave frequencies than they expected. Often, the commercial software WAMIT is utilized, as in [18], to complete the surface integration process and produce the coefficients of a lumped parameter model of the radiation, damping and the added mass forces. This can be completed even when a number of point absorbers are oscillating in a wave field but the WAMIT analysis neglects the diffracted wave field and flow separation, although it does account for the body geometry in the wave field. In the lumped parameter representation of the hydrodynamic effects, a single reference depth is used, as in [14], to calculate a single fluid velocity and acceleration values that is used in the calculation of radiation, damping and added mass forces that are each defined in terms of hydrodynamic coefficients. Since these semi-empirical expressions are linear in the velocity and acceleration terms, the models are referred to as linear lumped parameter models. Reduced order models, such as a lumped parameter representation, can also be readily constructed through regression analysis of experimental data.

However, there are limitations to the use of linear lumped parameter point absorber dynamics models. These include a misrepresentation of viscous effects since potential theory is used to calculate the hydrodynamic coefficients for such a model [19, 20, 21]. To capture viscous phenomena, some researchers have developed special purpose CFD (Computational Fluid Dynamics) codes that can act as a numerical wave tank – the results from which are then compared with physical scale model experiments [22, 23]. Further complex non-linear modelling can be considered and has been conducted by various researchers [23]. However, such studies are extremely time consuming and

have been found to produce changes on the predictions of simpler linear lumped parameter models that are within the level of uncertainty on the input wave conditions [23].

Each point absorber modelling method mentioned above (linear lumped parameter models based on the small body approximation, CFD and more complex non-linear numerical models) play a role in the point absorber design process. Linear lumped parameter models are used for early stage concept evaluation as in [18, 19], while for a more specific situation investigated such as the extreme wave loading in [23] a more complex numerical model (CFD) is required. However, a common need of any model is proper identification of the hydrodynamic model parameters. Experimentation with appropriately scaled physical models is absolutely necessary in order to summarize the geometry and frequency dependence of the hydrodynamic coefficients.

1.5 Hydrodynamic Characterization for Point Absorbers

Generalized experimentation, and/or linear lumped parameter numerical modelling, has been conducted and reported for basic cylinders in [24] and [25], where the hydrodynamic coefficients are numerically determined for various radii to draft ratios. For compound cylinders, with multiple radii and drafts a generalized computational method was developed in [26] and [27] and later compared with experimental results from [28]. The investigation of toroids was further developed in [29] where the hydrodynamic coefficients are numerically identified for various ring to core radius ratios. The investigation of various buoy bottom geometries has been numerically analyzed for hydrodynamic coefficients by [30], [19] and [21]. The combination of two concentric cylinders is evaluated in [31], where the hydrodynamic coupling is numerically determined for various configurations.

The various methods utilized in developing numerical models of various shapes and combination of shapes has been based on finite element methodologies or integral equations, or a combination of the two [27]. Numerical results compared in [27]

include the Boundary Element Method (BEM) and the Matching Technique (MT), both of which neglect the viscous effects. The two numerical methods compare quite well, but the newly developed Matching Technique was compared with experimental results and it was found that at higher wave frequencies the trend found in the linearized numerical model no longer follows experimental results; the added mass and damping both appeared to be under predicted [27]. For complex spar shapes and unique combinations of articulated floating bodies, experimentation is still required: there is not yet a comprehensive library of experimental data for point absorber spar geometries.

1.6 Research Objectives

At the University of Victoria, numerical modelling of the point absorber WEC design shown in Figure 6 must be complemented with a local capability for experimental hydrodynamic parameter identification. The type of numerical model being used at UVic is a linear lumped parameter representation of the hydrodynamics. In the short term, in-house experimentation will serve the study of the SWELS controller design. In the longer term, small scale experimentation at UVic could allow the range of spar geometries being considered to be expanded in pursuit for a more globally optimal control strategy; with a capacity to characterize various spar geometries, numerical modeling could be revised to such that parametric spar geometry and the control parameters are coupled inside the search for an optimal controller-spar design combination.

The primary objective of this research is to create a small scale wave tank that can be used to experimentally determine the hydrodynamic radiation damping, and added mass force coefficients of the point absorber WEC presented in Figure 6. In addition to designing and building the facility, a first batch of scale model point absorber experiments will be conducted that considers the range of wave frequencies that correspond to the expected sea states found off of the West coast of Vancouver Island. Those experiments will serve the secondary objective of the research program: to

determine the best fit lumped hydrodynamic coefficients for the current candidate point absorber geometry being considered, and the accuracy of those coefficients.

Special consideration will be given towards the coupling effects between the spar and float as the presence and motion of a secondary body, the float, will impact the hydrodynamics of the more complicated spar hull form. With the knowledge produced in this work, future control research will be able to comment, conclusively, on the potential of the proposed control approach in Vancouver Island conditions.

In order to accomplish the two overarching research objectives, five technical tasks must be completed:

1. Develop and characterize a small scale wave maker within the existing UVic fluid tunnel for small scale point absorber WEC physical model tests.
2. Validate the small tank's wave making abilities and its instrumentation through comparison to existing numerical model from [25] for the hydrodynamics of a simple cylinder.
3. Complete the first in-house experimental characterization of the hydrodynamic coefficients of the UVic point absorber WEC.
4. Determine the linear lumped parameter hydrodynamics utilizing the force-displacement data collected in wave-body interaction experiments.
5. Compare the point absorber WEC model experimental data to the existing numerical model from [25] for the hydrodynamics of a simple cylinder in order to determine the suitability of existing numerical models such as [25] for the WEC spar hydrodynamics.

1.7 Thesis Overview

Chapter 2 provides an introduction to the wave kinematics that are commonly used to express the wave circulation. The kinematic equations comprise the appropriate boundary conditions on the body surface, the interior fluid flow, and the conditions on all real/physical and artificial boundaries. A simplified hydrodynamic model utilizing the small body approximation and the linear wave kinematics is described in §2.4 and provides an idealized 2-DOF linear system representation of the spar and float motions. A detailed description of the lumped hydrodynamic coefficients found within the equations of motion is also included.

The constraints and criteria that guided the design of the wave making apparatus are presented in Chapter 3. The major design constraints of the existing facility are discussed, including model location, wave reflections, surface tension, wall effects and wave breaking. The full scale prototype's environmental conditions and wave regime is described. The scaling methodology is evaluated and scale model geometry presented.

Chapter 4 introduces the hydrodynamic testing apparatus and point absorber WEC support system design, along with details of the measurement instrumentation utilized and the wave maker design details. Experimental procedures for all tests are described including free oscillations in quiescent fluid, forced oscillations in quiescent fluid and fixed and free oscillations in a generated wave field.

Chapter 5 presents the experimental data gathered for three scale model geometries: a simple cylinder, the WEC spar hull and the WEC spar hull in the presence of the concentric float. The spar point absorber WEC component's interaction with the fluid is tested individually and the data set compared with the regenerated external numerical model from [25] for the most consistent geometry available, a cylinder of comparable diameter. Experimental data collected for the WEC spar and float components in combination are compared with the individual spar results to comment on the multi-body effects.

Chapter 6 is the conclusions and final recommendations of this research. The technical objectives and challenges faced in achieving them are discussed. Various improvements to the test facility and experimental methods are detailed for the benefit of future research. The chapter is concluded with a discussion on how the results of the experimentation impact the future design of the point absorbing WEC. Geometric effects such as a simple cylinder versus the complex spar, and combination of the spar-float geometry are discussed as well as the sensitivity of the hydrodynamic coefficient forces on wave frequency.

Chapter 2: Equation of Motion and Hydrodynamic Coefficients

2.1 Overview

Before entering into a discussion on the design of the small scale experimental test facility design, and the subsequent use of that apparatus to identify WEC hydrodynamic coefficients, a review of the fundamentals of linear lumped parameter WEC hydrodynamics modelling is necessary. In this Chapter, the equations of motion and definitions of the hydrodynamic coefficients are explained for this simplified mathematical modelling strategy. That discussion illustrates the gap in existing knowledge that prevents existing data sets from being directly applied to the study of the WEC shown in Figure 6. The mathematical modelling discussed in this Chapter defines the list of model coefficients that are required to be determined which subsequently sets the work plan of the experimental WEC work described in Chapter 4.

2.2 Wave Kinematics and Small Body Approximation

It is appropriate to use a monochromatic sinusoidal wave to construct the model of the activation forces on a floating body [16]. Point absorbing WECs are subject to a superposition of monochromatic waves of varying frequencies and directions. Since a heaving point absorber's motion is not significantly impacted by the varying direction of the waves, and since linear theory allows for the superposition of the absorber motions induced by the various wave field components, an investigation of the device dynamics in the presence of unidirectional monochromatic waves is fundamental to the analysis of the complete device response. A concise description of that monochromatic response can be obtained in the frequency domain, but the frequency domain framework must be populated with a description of the hydrodynamic parameters' frequency dependence.

The kinematic description of the monochromatic waves is taken from linear wave theory. Figure 7 below shows the important parameters including: the water depth d , the wavelength λ , the wave height h and the wave amplitude A . The displacement of the free surface is often referred to as $\eta(x,t)$. The period, T , is the time between successive peak amplitudes of the free surface at a single location.

The fluid particle trajectory is shown as elliptical in Figure 7, where u and w are the horizontal and vertical velocities respectively. The velocities can be defined utilizing ϕ , the velocity potential:

$$u = \frac{\partial \phi}{\partial x} \quad (2.1)$$

and

$$w = \frac{\partial \phi}{\partial z} \quad (2.2)$$

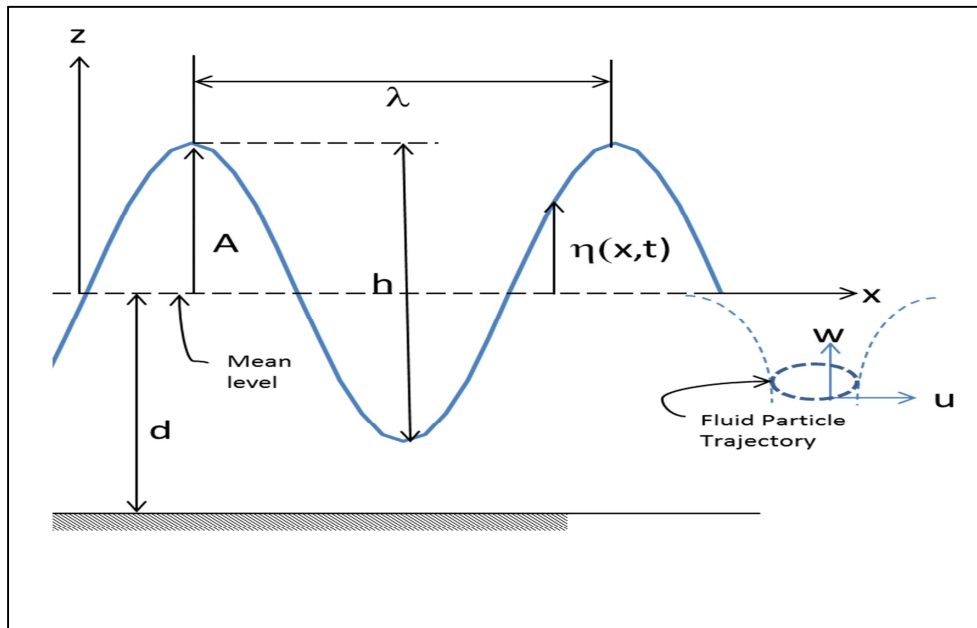


Figure 7 - Wave Parameter Definitions

The wave number, k , and the angular frequency, ω , are important parameters in the definition of the spatial and temporal variation of the free surface oscillations.

$$k = \frac{2\pi}{\lambda} \quad (2.3)$$

$$\omega = \frac{2\pi}{T} \quad (2.4)$$

The governing equations and boundary conditions that are used to define linear wave kinematics begin with the Laplace equation for two-dimensional flow:

$$\frac{\partial^2 \phi}{\partial x^2} + \frac{\partial^2 \phi}{\partial z^2} = 0 \quad (2.5)$$

Applying this velocity potential in the Bernoulli equation yields:

$$\frac{\partial \phi}{\partial t} + \frac{1}{2} \left[\left(\frac{\partial \phi}{\partial x} \right)^2 + \left(\frac{\partial \phi}{\partial z} \right)^2 \right] + \frac{p}{\rho} + gz = 0 \quad (2.6)$$

A few basic assumptions are commonly utilized including:

1. the fluid, seawater or fresh water, is homogeneous and incompressible,
2. the bottom of the fluid domain, whether a test tank or ocean floor, is horizontal, impermeable and stationary, and
3. the free surface maintains a constant pressure between the wave trough and wave peak instances.

Three boundary conditions are usually applied: two constrain the free surface conditions and the third enforces the impermeability of the bottom surface. The kinematic surface boundary condition (KSBC) at the free surface is defined in Equation (2.7).

$$w = \frac{\partial \eta}{\partial t} + u \frac{\partial \eta}{\partial x} \quad \text{at } z = \eta \quad (2.7)$$

The dynamic surface boundary condition (DSBC) at the free surface, where the gauge pressure is zero, comes from the Bernoulli equation for unsteady flow and is defined in Equation (2.8):

$$\frac{1}{2}(u^2 + w^2) + g\eta + \frac{\partial \phi}{\partial t} = 0 \quad \text{at } z = \eta \quad (2.8)$$

The bottom boundary condition (BBC), Equation (2.9), ensures that the normal flow at the bottom of the domain is zero:

$$w = 0 \quad \text{at } z = d \quad (2.9)$$

The wave amplitude is assumed to be small with respect to the water depth and the wavelength. In this case, the solution to the KSBC and DSBC is expedited by a linearization: the still water level is applied instead of the actual free surface level, η . The simplified KSBC and DSBC then become Equations (2.10) and (2.11) as the velocities u and w can be considered small, any product of these variables are very small and are neglected.

$$w = \frac{\partial \eta}{\partial t} \quad \text{at } z = 0 \quad (2.10)$$

$$g\eta + \frac{\partial \phi}{\partial t} \quad \text{at } z = 0 \quad (2.11)$$

The velocity potential of small amplitude linear waves is then derived from Equations (2.6), (2.7), (2.10) and (2.11), as

$$\phi = \frac{gh}{2\omega} \frac{\cosh k(d+z)}{\cosh(kd)} \cos kx \sin \omega t \quad (2.12)$$

The free surface profile is defined by setting $z = 0$ and combining Equations (2.11) and (2.12)

$$\eta = \frac{1}{g} \frac{\partial \phi}{\partial t} \Big|_{z=0} = \frac{h}{2} \cos(kx - \omega t) \quad (2.13)$$

The wave number is related to the angular frequency via the dispersion relation which is defined separately for deep and shallow water. In deep water conditions, where $h > 0.5\lambda$ [16], the wavenumber and angular frequency are related by:

$$k_d = \frac{\omega^2}{g} \quad (2.14)$$

For shallow water locations the wavenumber and angular frequency is related by:

$$k_s = \frac{\omega^2}{g \tanh(k_s d)} \quad (2.15)$$

In the remainder of the work, the wave number is represented by k , with the designation of deep or shallow water calculation methodology being determined based on the specific conditions considered. In §3.3, the influence of the WEC prototype and wave tank dimensions on the choice of the calculation of the wavenumber are discussed further.

Further discussion on boundary conditions and the solution to the linearized water wave boundary value problem can be found in [15]. It is important to note that the fluid particle motion is not constant throughout the depth of the fluid, it can be shown that the fluid particles move through an elliptical orbit, with an exponential decay as the depth increases, as shown in Figure 7. Using a deep water assumption where kd is considered large, $\cosh(kd)$ simplifies to $e^{kd}/2$ in the use of Equation (2.12). The water particle trajectory can then be identified by reviewing the velocity profiles for deep water:

$$u = \frac{\partial \phi}{\partial x} = \omega \frac{h}{2} e^{kz} \cos(kx - \omega t) \quad (2.16)$$

$$w = \frac{\partial \phi}{\partial z} = \omega \frac{h}{2} e^{kz} \sin(kx - \omega t) \quad (2.17)$$

The term e^{kz} shows the exponential decay; where the directions of horizontal and vertical velocity profiles combined generate the orbital motion. Further review of this effect can be reviewed in [16].

2.3 Floating Body Kinetics

With a sufficient description of the vertical oscillations of the fluid particles around the spar and float WEC components, the mathematical models of the WEC spar and float dynamics can be considered.

A floating body has six degrees of freedom, three rotational and three translational. The rotational are defined as: yaw on the z axis, roll on the x axis, and pitch on the y axis. The translational are defined as: surge in the x direction, heave in the z direction and sway in the y directions as shown in Figure 8, where the free surface is in the x - y plane.

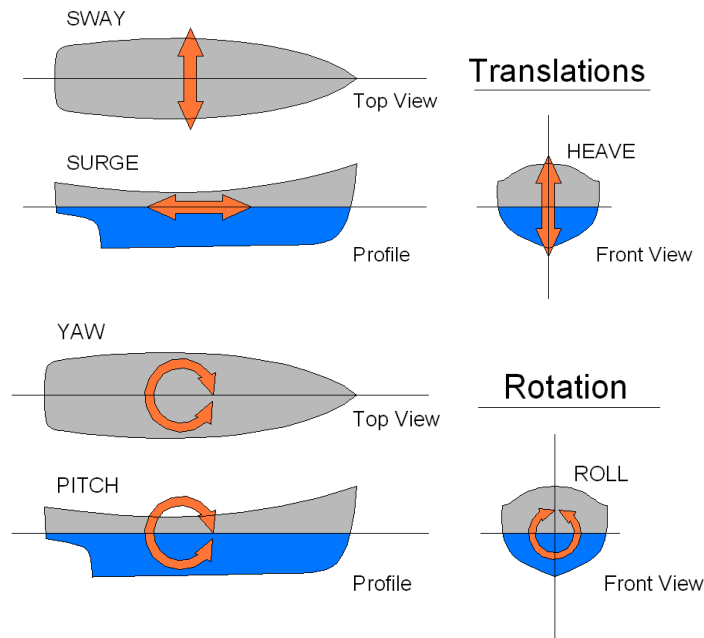


Figure 8 - Definition of floating body motions

For the two body point absorber WEC under investigation, the design of the spar and the mooring tends to curtail surge, sway and yaw motions. Ideally, the motion of the spar and float is limited to heave only in the z direction. A common simplification in the investigation of point absorbing WEC hydrodynamics is to reduce the equations of motion to only the heave degree of freedom (DOF) - as found in [19, 21, 32, 33].

For this research, only heave motions are considered and the other five degrees of freedom are eliminated from the motion equations. Pitch can potentially impact the overall relative translation of the float and spar, as described in detail in [34], and pitch dynamics have been investigated for floating hull forms in the field of naval architecture. It has also been shown in [34] that active control of the power-take-off (PTO) of a float-spar type point absorber WEC can reduce or eliminate the pitch motions. Given that others have shown the pitch motions can be curtailed, and that the pitching dynamics could be added in at a later date, it is reasonable to ignore the pitch DOF at this point. In Chapter 4: the experimental apparatus is described in detail including measures taken to ensure that the trials are heave only. Future

experimentation could be performed through revisions to that apparatus to allow for pitch only motion or a combination of heave and pitch motions.

The motions of a single floating body in waves can be evaluated by the superposition of two sets of forces:

1. The excitation forces created by the oscillating ambient water when the WEC hull component being considered is stationary.
2. The reactionary forces created by the motion of the WEC hull when the fluid is stationary.

The two sets of forces, excitation and reactionary forces, are combined to form the net activation force as discussed in §1.2.1. The forces action on the floating, heaving body, one of either the WEC spar or float for example, can be represented by a spring-mass-damper analogy shown in Figure 9.

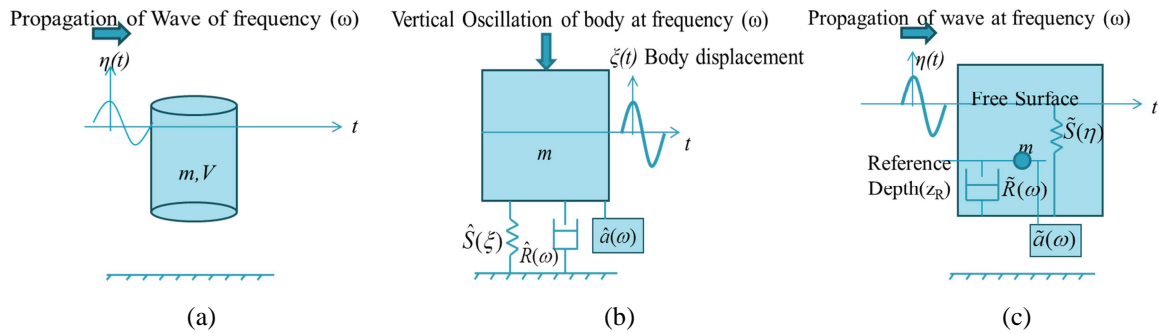


Figure 9 - Mechanical Oscillator Analogy of Floating Body.

(a) the floating hull displaces its own mass and is subject to an incident wave of a constant amplitude and frequency that creates a free surface displacement. (b) considering the free surface to be fixed, the motion of the hull, ξ , induces reactive forces that can be modelled with a spring-dashpot analogy. (c) considering the hull to be fixed in space, the free surface oscillation, η , and the associated fluid circulation beneath the surface induce additional forces that are proportional to the free surface elevation and the fluid velocity and acceleration at the reference depth.

In the following, $(\hat{\circ})$ indicates that the quantity in question is associated with excitation, and where $(\check{\circ})$ indicates that the quantity in question is associated with reaction. Figure 9 (a) shows a floating cylinder with a wave of frequency ω passing the cylinder of mass,

m , and the submerged volume V , where the body mass and volume of displaced fluid are related by Archimedes' principle. The body shown in Figure 9 (b) represents the oscillating body in a quiescent fluid. It has a true mass, m , equivalent to the mass in Figure 9 (a), but it also contains an additional mass, \hat{a} that represents the frequency dependant added mass that will be described in further detail in section §2.3.1. The reactive forces are represented by the spring constant, \hat{S} , and the damper, \hat{R} . The spring constant is also described as the hydrodynamic stiffness, which is actually equivalent to the buoyancy force, and is therefore dependant on the submerged volume. Both the added mass and damping coefficients are frequency dependant.

The system shown in Figure 9 (c) is a simplified mechanical oscillator that represents the fixed body in a wave field. Here, the stiffness, \tilde{S} , damping, \tilde{R} and added mass, \tilde{a} , represent the excitation force exerted by the wave on the body. The added mass and damping terms are directly related to the acceleration and velocity, respectively, of the fluid particles. Since the fluid velocity and acceleration are depth dependant, a reference depth is selected to be utilized as shown in Figure 9 (c). Since the buoyancy force is set by the free surface elevation, not the body displacement from the free surface, the stiffness, \tilde{S} , is shown connecting the body to the free surface instead of the fluid domain's bottom boundary.

2.3.1 Wave Excitation Force

The hydrodynamic coefficients shown in Figure 9 exist for both floating components of the point absorbing WEC, the spar and the float. Fixing either body in the wave field, as illustrated in Figure 9 (c) would eliminate the reaction forces leaving only the wave excitation force given by \tilde{F}_E :

$$\tilde{F}_E = \tilde{F}_B + \tilde{F}_D + \tilde{F}_I \quad (2.18)$$

Each of the three forces on the right hand side of Equation (2.18) represents a hydrodynamic loading on the body when only the heaving motion of the fluid particles is considered.

The excitation buoyancy force, \tilde{F}_B , is dependent on the changing draft of the floating, oscillating body and is defined by Archimedes principle. The buoyancy force is represented by the spring in the mass-spring-damper analogy, as it acts linearly with the displacement of the body.

$$\tilde{F}_B = \tilde{S}\eta e^{i\omega t} \quad (2.19)$$

The excitation diffraction force \tilde{F}_D is the force that occurs as the fluid moves by the stationary body, it is a linearization of the actual drag forces; the skin friction and form drag. The diffraction force is represented by the damper in the mass-spring-damper analogy, as it is dependent on the fluid velocity. This damping force represents the dissipation of energy that occurs when diffracted waves carry energy away from the body. The diffraction force is given by:

$$\tilde{F}_D = (\tilde{R} + \tilde{c}_v)\dot{\eta} e^{kz_R} e^{i\omega t} \quad (2.20)$$

The component of the diffraction force due to the waves is calculated based the coefficient as R . As discussed in §2.2, the fluid velocity decays as water depth increases, therefore, this coefficient must be modulated to account for the lower fluid velocities towards the bottom of the floating body hull. That modulation factor is defined in terms of a reference depth, z_R . The reference depth of a composite cylinder body is the weighted average depth of the horizontal planes that interact with the vertical fluid motions of the incident waves [14]. The exponential decay of the water particle trajectories satisfies the no-slip condition at the bottom and the exponential term varies between 1 and 0.

The drag forces are only grossly modeled by a simple linear or viscous term. The additional viscous term, c_v , ensures that the damping term does not go to zero as frequency decreases. The damping coefficients for the excitation forces can then be lumped together and designated \tilde{b} . The equation becomes:

$$\tilde{F}_D = \tilde{b} \dot{\eta} e^{kz_R} e^{i\omega t} \quad (2.21)$$

The inertial force is also dependant on the body's reference depth and it also induces an added inertial resistance to the acceleration of the fluid. To navigate any exposed horizontal surfaces of the submerged hull, the accelerating fluid must accelerate fluid neighbouring the body and the mass of that fluid is referred to as added mass. The total inertial component in the excitation force is a sum of two components: one due to the pressure gradient that accelerated the fluid and the other being the added mass component. The first component is known to equal the mass of the displaced fluid, m , and the second, \tilde{a} , is a fraction of the displaced fluid. The inertial force is given by:

$$\tilde{F}_I = (m + \tilde{a}) \ddot{\eta} e^{kz_R} e^{i\omega t} \quad (2.22)$$

Insertion of the hydrodynamic loading forces defined by Equations (2.19) through (2.22), into the wave excitation equation, transforms Equation (2.18) into:

$$\tilde{F}_E = (\tilde{S}\eta + [\tilde{b}\dot{\eta} + (m + \tilde{a})\ddot{\eta}]) e^{kz_R} e^{i\omega t} \quad (2.23)$$

2.3.2 WEC Reaction Forces

For the case where the body is oscillating and the fluid is quiescent as illustrated in Figure 9 (b), a reactive force, similar in form to the wave excitation force defined in §2.3.1 exists. It is composed of three parts: a variable buoyancy force \hat{F}_B , a radiation force \hat{F}_D , and the inertia force \hat{F}_I .

$$\hat{F}_R = \hat{F}_B + \hat{F}_D + \hat{F}_I \quad (2.24)$$

The reactive force, \hat{F}_R , always acts to return a body to its equilibrium position in still water. The buoyancy component, \hat{F}_B , is proportional to the body's displacement and is created by changes in the buoyancy force experienced as the hull is raised out of or lowered into the water, where ξ and its derivatives refer to the body displacement, velocity and accelerations with respect to the quiescent free surface as shown in Figure 9 (b).

$$\hat{F}_B = \hat{S}\xi e^{i\omega t} \quad (2.25)$$

The radiation component is proportional to the body velocity and is a combination of viscous skin friction and the energy loss to the generation of waves radiated by the body as it oscillates. The radiation term is similar to the diffraction term described for the excitation forces, but it is not dependent on the reference depth as the relative velocity of the body is constant with depth since the fluid particles are considered stationary. The damping lumped parameter term for the radiation term is designated as \hat{b} .

$$\hat{F}_D = (\hat{R} + \hat{c}_v)\dot{\xi} e^{i\omega t} \quad (2.26)$$

$$\hat{F}_D = \hat{b}\dot{\xi} e^{i\omega t} \quad (2.27)$$

The inertial force is proportional to the body's acceleration and is created by the added mass phenomenon described above.

$$\hat{F}_I = \hat{a}\ddot{\xi} e^{i\omega t} \quad (2.28)$$

Insertion of the hydrodynamic loading forces defined by Equations (2.25) through (2.28), into the wave reactionary equation, transforms Equation (2.24) into:

$$\hat{F}_R = (\hat{S}\xi + \hat{b}\dot{\xi} + \hat{a}\ddot{\xi})e^{i\omega t} \quad (2.29)$$

Additional reaction terms can be found within the multi-body system as described later in §2.4.2, these include the interaction forces that exist due to an additional body being present and disturbing the wave field. To clarify the additional added mass and damping effects, subscript are introduced to delineate the single and multi-body effects in the equations of motion in §2.4.

2.4 Equations of motion

2.4.1 Equation of motion of a 1-DOF system

The equations of motion for a two body (spar-float) point absorber are assembled here from the individual motion equations of the spar and float components. The spar is considered first and is referred to as body 1. The equation of motion is developed from Newton's Second Law where the sum of the forces, in this case the excitation and reaction forces, are superposed. The subscript notations on the forces and coefficients indicate the dependence of the force and coefficient on the state of body 1, the spar, or body 2, the float. For instance, $(\bullet)_{11}$ indicates that the force is acting on body 1 due to the motion of body 1, the subscript $(\bullet)_{21}$ would indicate a force on body 2 due to the motion of body 1, and the subscript $(\bullet)_{2i}$ indicates the force on body 2 due to the presence of body 1, it should be noted that the 'i' in the subscripts indicates an induced force that occurs even if the source body is motionless. Coefficients defining coupled spar-float dynamic effects are added when the independent spar and float equations of motion are assembled.

All of the hydrodynamic parameters are considered to be frequency dependant except the actual body mass, m , and the buoyancy component, denoted by S .

The assembled equation of motion for body 1, in isolation, is:

$$\sum F = m\ddot{\xi} \quad (2.30)$$

$$\tilde{F}_{E11} + \hat{F}_{R11} = m\ddot{\xi} \quad (2.31)$$

$$\tilde{F}_{I11} + \tilde{F}_{D11} + \tilde{F}_{B11} + \hat{F}_{I11} + \hat{F}_{D11} + \hat{F}_{B11} = m\ddot{\xi} \quad (2.32)$$

$$\left[(m_1 + \tilde{a}_{11})\ddot{\eta} + \tilde{b}_{11}\dot{\eta} + \tilde{S}_1\eta \right] e^{kz_R} e^{i\omega t} = \left[(m_1 + \hat{a}_{11})\ddot{\xi} + \hat{b}_{11}\dot{\xi} + \hat{S}_1\xi \right] e^{i\omega t} \quad (2.33)$$

An analogous motion equation exists for the float with the only differences being in the specific frequency dependence of the hydrodynamic coefficients and the reference depth value.

2.4.2 Equation of motion of a 2-DOF system

When the point absorber spar and float are assembled for the purposes of this research, new coefficients must be added to the collective heave equations of motion for the two bodies. These new forces are due to the disturbance of the wave field caused by the presence of the bodies, and the creation of radiated waves by each body. A power take off unit is not utilized in the experimental setup, and therefore a PTO force is not considered in the 2-DOF system for this work. The equations are coupled by the forces induced by the second bodies presence and motion (a consequence of a radiated wave), which is broken down into the inertial components, \tilde{F}_{I12} , \hat{F}_{I12} and the radiation damping components, \tilde{F}_{D12} , \hat{F}_{D12} for excitation and reaction forces respectively. The 2-DOF system inertial forces are an extension of the 1-DOF inertial forces with the addition of the added mass interaction components, \tilde{a}_{12i} , \hat{a}_{12i} and added mass from the second body motion, \hat{a}_{12m} in the reactive force, where the subscript ‘m’ refers to the motion of the second body, as shown:

$$\tilde{F}_{I12} = (m_1 + \tilde{a}_{11} + \tilde{a}_{12i})\ddot{\eta}e^{kz_R}e^{i\omega t} \quad (2.34)$$

$$\hat{F}_{I12} = [(\hat{a}_{11} + \hat{a}_{12i})\ddot{\xi}_1 + \hat{a}_{12m}\ddot{\xi}_2]e^{i\omega t} \quad (2.35)$$

The 2-DOF system radiation damping forces are again an extension of the 1-DOF radiation forces with the addition of the damping interaction components, \tilde{b}_{12i} , \hat{b}_{12i} , and the damping component from the second body motion, \hat{b}_{12m} , in the reactive force, as shown:

$$\tilde{F}_{D12} = (\tilde{b}_{11} + \tilde{b}_{12i})\dot{\eta}e^{kz_R}e^{i\omega t} \quad (2.36)$$

$$\hat{F}_{D12} = [(\hat{b}_{11} + \hat{b}_{12i})\dot{\xi}_1 + (\hat{b}_{12m})\dot{\xi}_2]e^{i\omega t} \quad (2.37)$$

The 2-DOF system equation of motion is presented:

$$\tilde{F}_{I12} + \tilde{F}_{D12} + \tilde{F}_{B11} + \hat{F}_{I12} + \hat{F}_{D12} + \hat{F}_{B11} = m_1\ddot{\xi}_1 \quad (2.38)$$

$$\begin{aligned} & [(m_1 + \tilde{a}_{11} + \tilde{a}_{12i})\ddot{\eta} + (\tilde{b}_{11} + \tilde{b}_{12i})\dot{\eta} + S_1\eta]e^{kz_R}e^{i\omega t} \\ & = \left[[(m_1 + \hat{a}_{11} + \hat{a}_{12i})\ddot{\xi}_1 + \hat{a}_{12m}\ddot{\xi}_2] + [(\hat{b}_{11} + \hat{b}_{12i})\dot{\xi}_1 + (\hat{b}_{12m})\dot{\xi}_2] + S_1\xi_1 \right]e^{i\omega t} \end{aligned} \quad (2.39)$$

Equivalent forces exist for body 2 and a very similar equation of motion can be written. The new additional coefficients definitions seen in Equation (2.39) can be applied to the other body, where the coupling force changes, with body 1 impacting body 2. It can therefore be expected that the motion of the body 1 will influence the motion of body 2, and vice versa. But since this effect is transferred through perturbations in the wave circulation, the effects will not be equal. As a result, the system matrices are not necessarily symmetric, for example, it is assumed that $\hat{b}_{12m} \neq \hat{b}_{21m}$. The two motion equations can be assembled to yield:

$$\begin{aligned}
& \begin{pmatrix} m_1 + \tilde{a}_{11} + \tilde{a}_{12i} & 0 \\ 0 & m_2 + \tilde{a}_{22} + \tilde{a}_{21i} \end{pmatrix} \{\dot{y}\} + \begin{pmatrix} \tilde{b}_{11} + \tilde{b}_{12i} & 0 \\ 0 & \tilde{b}_{22} + \tilde{b}_{21i} \end{pmatrix} \{\dot{y}\} + \\
& \begin{pmatrix} \tilde{S}_1 & 0 \\ 0 & \tilde{S}_2 \end{pmatrix} \{y\} = \begin{pmatrix} m_1 + \hat{a}_{11} + \hat{a}_{12i} & \hat{a}_{12m} \\ \hat{a}_{21m} & m_2 + \hat{a}_{22} + \hat{a}_{21i} \end{pmatrix} \{\ddot{x}\} + \\
& \begin{pmatrix} \hat{b}_{11} + \hat{b}_{12i} & \hat{b}_{12m} \\ \hat{b}_{21m} & \hat{b}_{22} + \hat{b}_{21i} \end{pmatrix} \{\dot{x}\} + \begin{pmatrix} \hat{S}_1 & 0 \\ 0 & \hat{S}_2 \end{pmatrix} \{x\}
\end{aligned} \tag{2.40}$$

Where $\vec{x} = \begin{Bmatrix} \xi_1 \\ \xi_2 \end{Bmatrix} e^{i\omega t}$

And $\vec{y} = \begin{Bmatrix} \eta e^{kz_{R1}} \\ \eta e^{kz_{R2}} \end{Bmatrix} e^{i\omega t}$

For experimental purposes, only a total lumped parameter is able to be evaluated, therefore the multi body system also requires the addition of the added mass lumped parameter to include the interaction component, and is defined as

$$a_{12} = a_{11} + a_{12i} \tag{2.41}$$

and for body 2 as

$$a_{21} = a_{22} + a_{21i} \tag{2.42}$$

The damping lumped parameter also must include the interaction components.

$$b_{12} = b_{11} + b_{12i} \tag{2.43}$$

and for body 2 as

$$b_{21} = b_{22} + b_{21i} \tag{2.44}$$

The equation of motion of the two body system becomes

$$\begin{aligned} & \begin{pmatrix} m_1 + \tilde{a}_{12} & 0 \\ 0 & m_2 + \tilde{a}_{21} \end{pmatrix} \{\ddot{y}\} + \begin{pmatrix} \tilde{b}_{12} & 0 \\ 0 & \tilde{b}_{21} \end{pmatrix} \{\dot{y}\} + \begin{pmatrix} \tilde{S}_1 & 0 \\ 0 & \tilde{S}_2 \end{pmatrix} \{y\} \\ & = \begin{pmatrix} m_1 + \hat{a}_{12} & \hat{a}_{12m} \\ \hat{a}_{21m} & m_2 + \hat{a}_{21} \end{pmatrix} \{\ddot{x}\} + \begin{pmatrix} \hat{b}_{12} & \hat{b}_{12m} \\ \hat{b}_{21m} & \hat{b}_{21} \end{pmatrix} \{\dot{x}\} + \begin{pmatrix} \hat{S}_1 & 0 \\ 0 & \hat{S}_2 \end{pmatrix} \{x\} \end{aligned} \quad (2.45)$$

2.5 Closing

Of the variables found in Equation (2.45), the frequency dependent added mass and damping coefficients are the most difficult to predict for specific spar and float geometries. As discussed in §1.5, these coefficients can only be roughly estimated for the particular point absorbing WEC under investigation, such as in [35, 36, 28, 37, 33].

A breakdown of the hydrodynamic coefficients that are needed in order to apply Equation (2.45) are defined in Table 1 through Table 8.

Table 1 – Experimentally Determined 1-DOF Spar Excitation Coefficients

<i>Parameter</i>	<i>Description</i>
\tilde{a}_{11}	Added mass of body 1 in excitation
\tilde{b}_{11}	Radiation damping coefficient for body 1 in excitation (lumped)

Table 2 - Experimentally Determined 1-DOF Spar Reaction Coefficients

<i>Parameter</i>	<i>Description</i>
\hat{a}_{11}	Added mass of body 1 in reaction
\hat{b}_{11}	Radiation damping coefficient for body 1 in reaction (lumped)

Table 3 - 1-DOF Float Excitation Coefficients (not experimentally evaluated in this research)

<i>Parameter</i>	<i>Description</i>
\tilde{a}_{22}	Added mass of body 2 in excitation
\tilde{b}_{22}	Radiation damping coefficient for body 2 in excitation (lumped)

Table 4 - 1-DOF Float Reaction Coefficients (not experimentally evaluated in this research)

<i>Parameter</i>	<i>Description</i>
\hat{a}_{22}	Added mass of body 2 in reaction
\hat{b}_{22}	Radiation damping coefficient for body 2 in reaction (lumped)

Table 5 - Experimentally Determined 2-DOF Spar Excitation Coefficients

<i>Parameter</i>	<i>Description</i>
\tilde{a}_{12}	Added mass of body 1 when body 2 is present in excitation (lumped)
\tilde{b}_{12}	Radiation damping coefficient for body 1 when body 2 is present in excitation (lumped)

Table 6 - Experimentally Determined 2-DOF Spar Reaction Coefficients

<i>Parameter</i>	<i>Description</i>
\hat{a}_{12}	Added mass of body 1 when body 2 is present in reaction (lumped)
\hat{b}_{12}	Radiation damping coefficient for body 1 when body 2 is present in reaction (lumped)
\hat{a}_{12m}	Added mass of body 1 when body 2 is in motion in reaction (not evaluated)
\hat{b}_{12m}	Radiation damping coefficient for body 1 when body 2 is in motion in reaction

Table 7 - 2-DOF Float Excitation Coefficients (not experimentally evaluated in this research)

<i>Parameter</i>	<i>Description</i>
\tilde{a}_{21}	Added mass of body 2 when body 1 is present in excitation (lumped)
\tilde{b}_{21}	Radiation damping coefficient for body 2 when body 1 is present in excitation (lumped)

Table 8 - 2-DOF Float Reaction Coefficients (not experimentally evaluated in this research)

<i>Parameter</i>	<i>Description</i>
\hat{a}_{21}	Added mass of body 2 when body 1 is present in reaction (lumped)
\hat{b}_{21}	Radiation damping coefficient for body 2 when body 1 is present in reaction (lumped)
\hat{a}_{21m}	Added mass of body 2 when body 1 is in motion in reaction
\hat{b}_{21m}	Radiation damping coefficient for body 2 when body 1 is in motion in reaction

Chapter 3: Experimental Considerations and Constraints

3.1 Overview

This Chapter describes in detail the design requirements and constraints on the wave making and small scale WEC testing apparatuses. The test facility is built on an existing fluid tunnel and the logistical constraints imposed by this existing infrastructure are discussed. The choice of a model WEC geometric scaling factor that is tenable with the existing tank dimensions is also presented along with the scaled WEC dimensional details. The characteristics of the ocean waves experienced off of Vancouver Island are described, the selected dynamic scaling methodology is applied to the wave regime, and the wave maker requirements are defined. Additional details on non-conformance within the scaling of the WEC and the wave kinematics are also provided.

3.2 The Fluid Tunnel

The experiments require a fluid tank that has a number of features, including a visible test section, adequate length for the propagation of the generated waves, and wave making capability. The UVIC Department of Mechanical Engineering currently has a flow visualization water tunnel with a test section measuring 2.5m x 0.45m x 0.45m [L x W x H]. The facility can produce unidirectional constant velocity laminar flow up to 2m/s that is circulated by a mechanical pump. The fluid travels from the pump through a honeycomb structure that reduces turbulence then converges into the test section, after which it passes through a diverting manifold and is returned to the pump through the outflow, as shown in Figure 10.

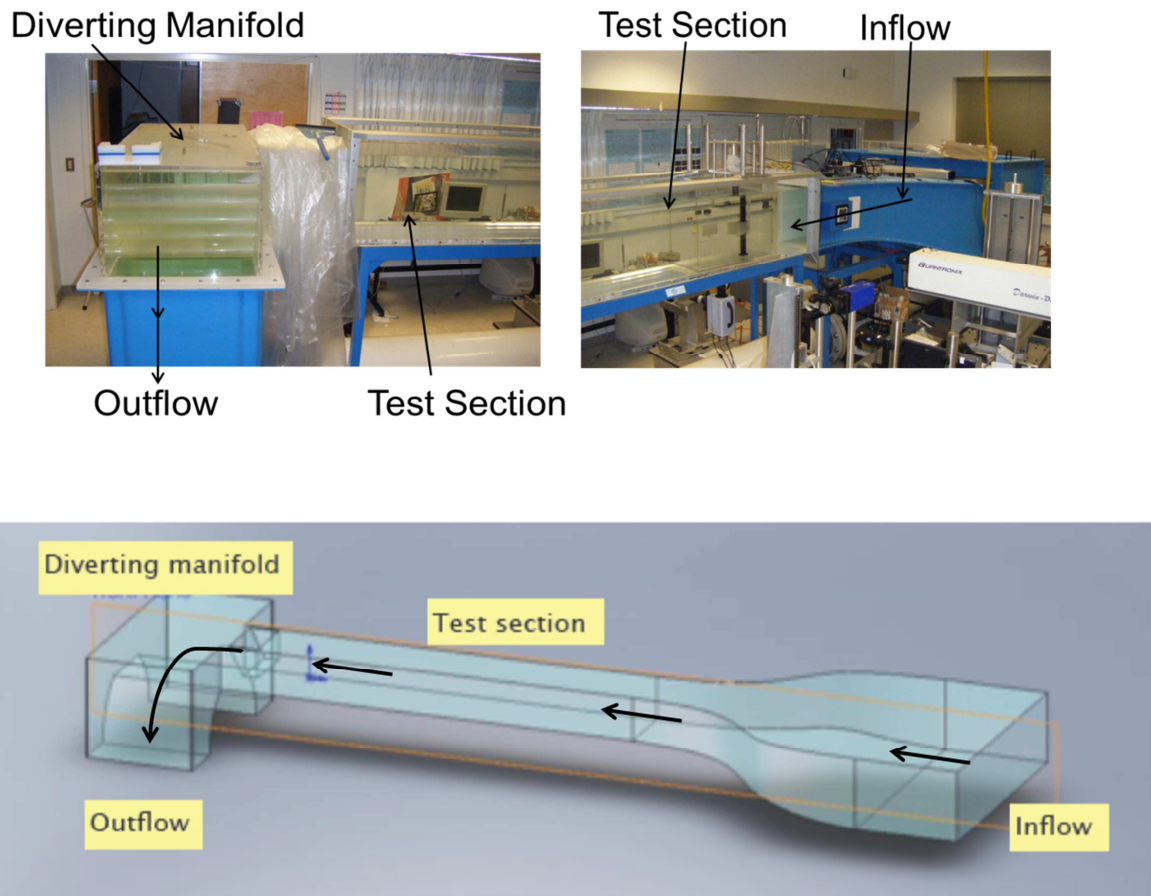


Figure 10 - UVIC fluid tunnel

For the purposes of this body of WEC research, the current producing capabilities of the tank are not utilized. In order to absorb generated waves, a beach must be included to prevent reflections from polluting the experimental data. However, the relatively short length of the test section makes it challenging to install both a wave maker and a beach without compromising the test section. In fact, the existing tank parameters pose constraints to the model location, model size, and wave kinematics.

Constraining Model Location: The dominant design constraint for the wave-maker is the tank length, as it limits the possible wavelengths that can be generated and thus also controls where the model WEC can be located within the tank. Current best practice suggests the location of a model must be located at least twice the hinge depth or for this tank, 0.8m, for the wave to become fully developed [38]. In order to make

evanescent waves generated by the wave-maker negligible, the test section must be at least three water depths away from the wave-maker [15]. This designates the potential location of the test model, to be at least 1.2m from the wave-maker as shown in Figure 11.



Figure 11 - Test Facility Length Constraints

Preventing Wave Reflections: In addition to the model location constraint, the possibility of wave reflections from the end of the test section must be mitigated. The tank is currently fitted with a unique flow diffuser at one end that is designed to straighten the flow at the interface of the inflow and test sections seen in Figure 10. In this work, the propagation direction of the waves is reversed from the normal current direction. In doing so, the honeycomb section can act to dissipate the kinetic energy in the wave oscillations and hopefully destroy the wave before it enters the inflow section. Conventional beach design suggests that for a beach to absorb 90% of the incoming wave it should be at least half of the wavelength in size [38]. The honeycomb section is not a conventional beach and does not follow the same guidelines; therefore the wave data will need to be reviewed during experimentation to determine its suitability for the desired wavelengths. The wave data will be reviewed in §5.2 for obvious wave reflection.

Maximum Wave Height: The geometry of the fluid tunnel allows a maximum fluid level of 45cm from the tank bottom without interaction with any sharp edges entering either the tunnel inlet or outlet, therefore in order to allow a wave form; the allowable

mean water depth is reduced to 40cm for a maximum of a 10cm wave height to be generated.

Preventing surface tension effects: The surface tension effect occurs when the cohesion of water molecules produces a strong film on the air-water interface that interferes with the motion of the floating surface piercing body. Effects due to surface tension are expected to be eliminated with a minimum wave period of 0.5 seconds [39]. Applying the dispersion relation, this condition determines the minimum wavelength that can be used in the tank, approximately 0.4m.

Preventing wall effects: Based on tank width and depth, the model needs to fit within a specific envelope to avoid side wall reflections and contact with the tank bottom. To avoid influences from the tank sides, the maximum model diameter should be 1/5th the tank width, which translates to 0.09m given the 0.45m tank width [38]. The max draft of the model should provide bottom clearance even when the largest waves possible are being generated.

Preventing wave breaking: For deep water waves, the wave breaking is based upon the maximum wave steepness (the ratio of wave height to wavelength or H/λ) of 1/7 [39]. In shallow water, the wave breaking also depends on the relative depth d/λ (water depth to wavelength) where the wave height to water depth ratio at breaking is between 0.8 and 1.2, depending on the beach slope and wave period. Assuming deep water with a freeboard availability of 0.05m equivalent to half the maximum wave height, the minimum wavelength for the maximum wave height is 0.7m. Or for the wave height of 0.01m the minimum wavelength is 0.07m as shown in Table 9 for deep water. If shallow water conditions are considered, the largest possible wave height of 0.1m only reaches a ratio of 0.25 and wave breaking is not expected to occur as shown in Table 10.

Table 9 - Wave Breaking: Deep Water

<i>Wave Height (H)</i>	<i>Minimum Wavelength (λ) to avoid wave breaking ($H/\lambda < 1/7$)</i>
0.01m	0.07m
0.1m	0.7m

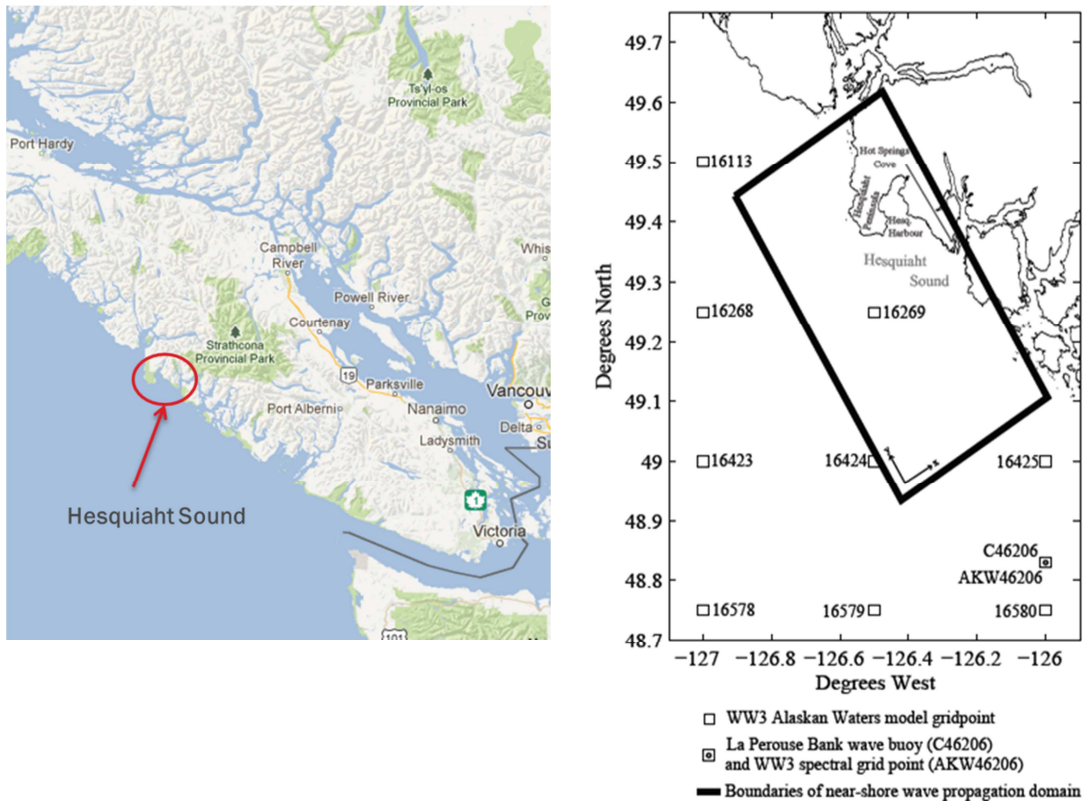
Table 10 - Wave Breaking: Shallow Water

<i>Wave Height (H) ($d=0.4m$)</i>	<i>Wave Height to Water Depth Ratio to avoid wave breaking ($H/d < 0.8$)</i>
0.01m	0.025 NO BREAKING
0.1m	0.25 NO BREAKING

3.3 Environmental Conditions

In order to determine the wave kinematics that need to be replicated in the test facility the environmental conditions expected at the prototype WEC's deployment location must be understood. Understanding collected wave data and spectral analysis is a core requirement to developing representative model experiments.

One potential location for a prototype wave energy converter is seen in Figure 12: Hesquiaht Sound, on the central Vancouver Island west coast, in Nuuchah-nulth traditional territory north of Tofino, British Columbia. The wave conditions in Hesquiaht Sound have been studied in past wave energy resource assessment research at UVic [40]. As discussed in [40] and in [41], the global wind-wave model WAVEWATCHIII (WW3) operated by the National Oceanic and Atmospheric Administration, was used to build a set of directional wave conditions for the offshore boundary of Hesquiaht Sound. Referring to [40] for further detail, the offshore conditions were translated to directional wave spectra at each grid point of a fine scale REF/DIF model of Hesquiaht Sound.



(a)

(b)

Figure 12 – Hesquiaht Sound (a) Location of Hesquiaht Sound on Vancouver Island (b) Wave Energy Converter Test Site Location in Hesquiaht Sound.

The grid points are WW3 grid points for which power Spectra data are available. Numbered grid point 16424 is the WW3 grid point used to define the offshore conditions for Hesquiaht Sound.

3.3.1 Hesquiaht Sound - Offshore Conditions

Ocean swell is considered to be a superposition of a large number of monochromatic waves, each with unique amplitude, frequency, and phase and from all directions. This is most often referred to as an irregular sea state. For the purpose of this research, it is important to extract from the irregular free surface oscillations the series of component monochromatic waves that create it. Ideally, the full range of wave frequencies and heights in this series of monochromatic waves will be replicated in the small scale WEC experimentation at UVIC.

The WW3 wind-wave model is executed using hindcast wind data. The energy generates an estimate of the wave generated over a large fetch by the wind. The results

are most often displayed as a power spectrum, or variance density spectrum, over a range of frequencies and directions. From the power spectrum, a significant wave height, H_s , peak period, T_p , and wave direction, θ_p , are extrapolated. The significant wave height can be defined as the average of the highest one third of all waves. The peak period, T_p , and peak wave direction, θ_p , are the period and direction at which the variance density is at its maximum value.

In [40], data from grid points 16424 and AKW46206 were fused to create a typical year of offshore conditions for Hesquiaht Sound.

3.3.2 Hesquiaht Sound – Near Shore Conditions

In [40] the wave regime for the near shore WEC locations shown in Figure 13 was generated utilizing near shore modelling. The near shore modeling utilized the offshore wave regime as boundary conditions as discussed in §3.3.1, as well as the local bathymetry in a REF/DIF model. The positions A-E were selected for potential deployment locations of a prototype WEC, the near shore wave propagation model exact latitude and longitude of these positions are listed in Table 11. Figure 14 shows the mean wave conditions for points A-E, and the offshore as determined in [40]. Site D is suggested as a promising location for the prototype WEC as it is closest to shore, but maintains 66% of the wave energy as found offshore. From this data, it can be roughly estimated that a prototype period T_p ranging between 5s and 20s and wave heights H_s ranging from 1m to 3m should be considered in small scale WEC experiments at UVIC. The wave directions were not considered in planning the monochromatic wave experiments since the technology being considered is an omnidirectional point absorber.

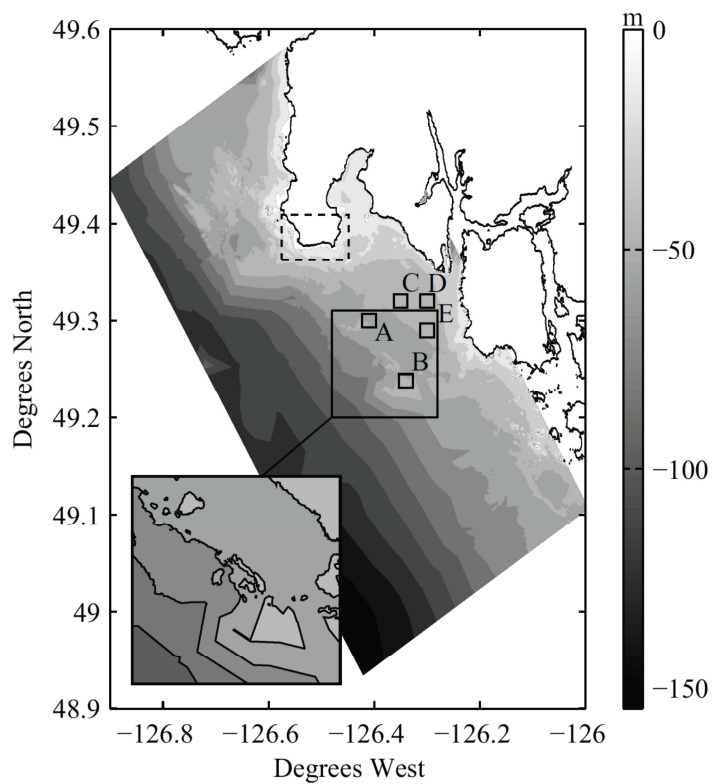


Figure 13 - Bathymetric data in Hesquiaht Sound and selected near-shore sites A-E.

Table 11 - Deployment Site Locations

<i>Site #</i>	<i>Coordinates (Easting or Longitude)</i>	<i>Coordinates (Northing or Latitude)</i>
A	-126.41	49.3
B	-126.34	49.238
C	-126.35	49.32
D	-126.3	49.32
E	-126.3	49.29

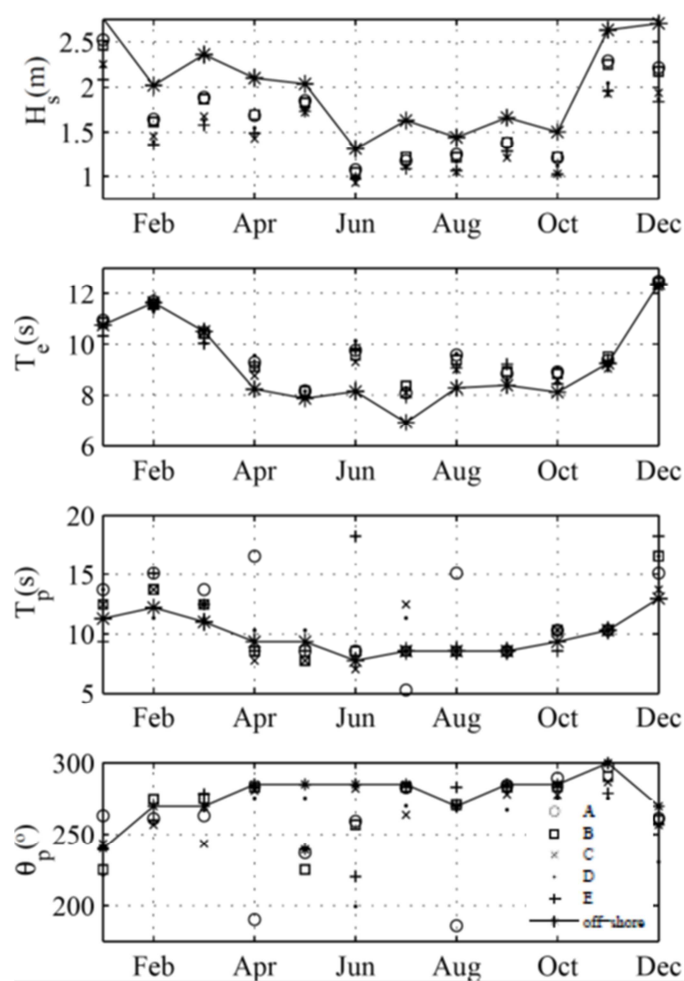


Figure 14 - H_s , T_p and θ_p offshore and for selected near-shore points A-E

This data is also used to determine the site water depth characteristic for the wave number. Recall that deep water is defined as the water depth, d , being greater than half the wavelength, λ . At the selected site, D, the water depth is 39m and the wavelength ranges from 107-217m utilizing both deep and shallow wave number formulations. All of which deem the site as shallow water.

3.4 Full Scale WEC Prototype Physical Parameters

The WEC prototype that was being considered by SyncWave Energy Inc. for deployment at the location shown in Figure 14 has a total mass of 160,000 kg including ballast, a float outer diameter of 5m, a spar draft of 30m and a maximum capacity of 100kW. The general construction of the WEC prototype can be seen in Figure 15. The physical parameters relevant to the hydrodynamic characterization experiments being conducted in this work are defined in Figure 16.

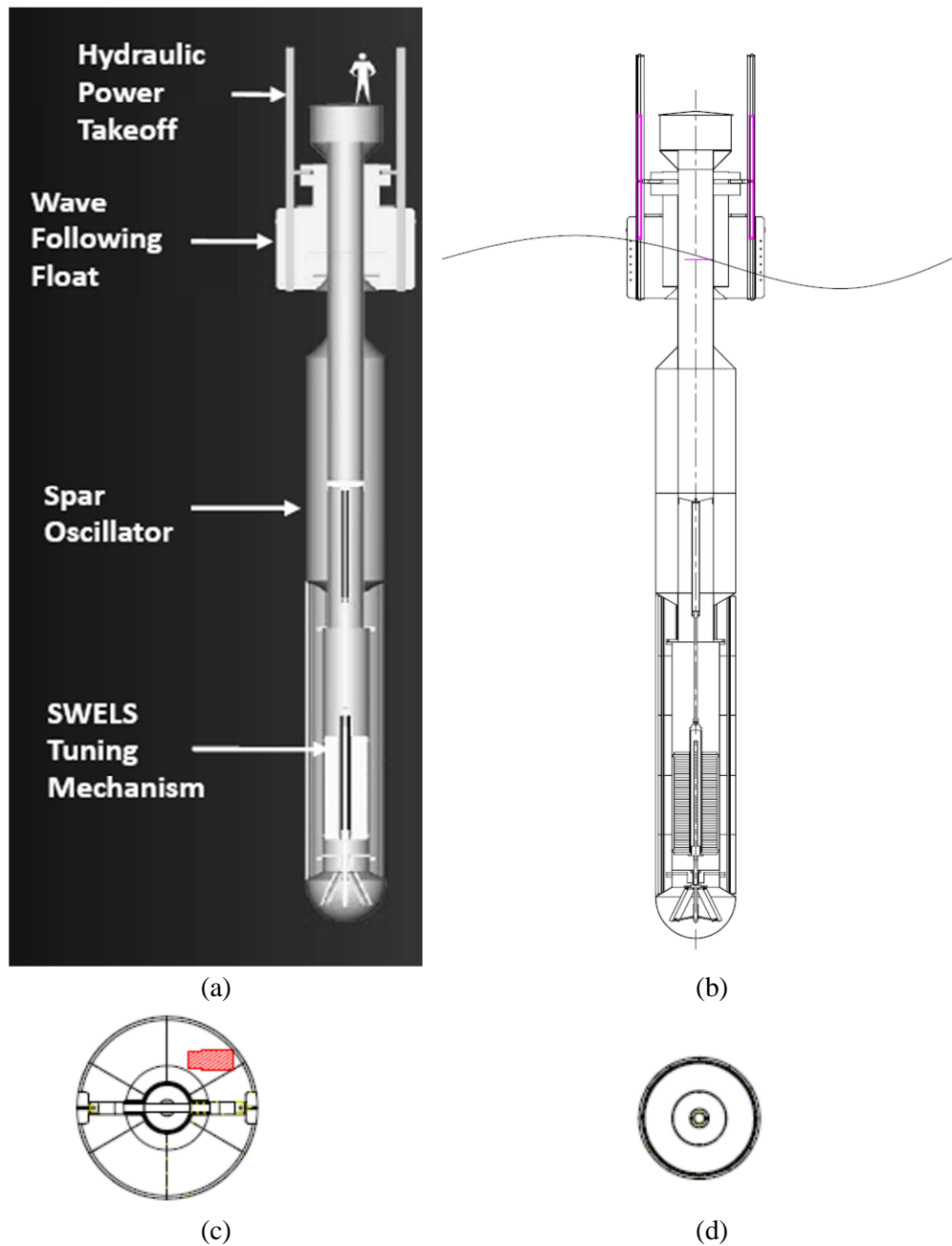


Figure 15 - SyncWave Point Absorbing WEC
 (a) a front view showing the size of the planned device relative to an average height (5'10'') individual; (b) Full elevation line drawing ; (c) Top view line drawing; (d) Top view spar line drawing .

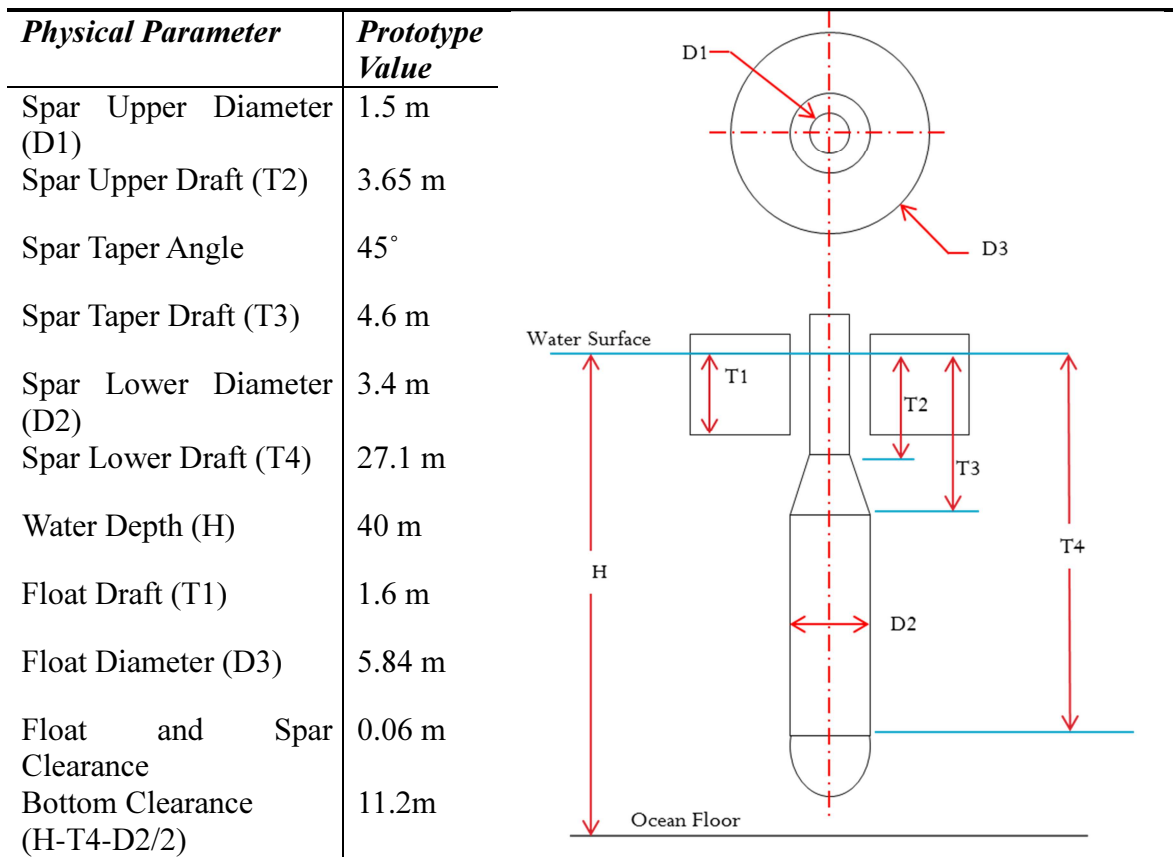


Figure 16 - WEC Prototype Design Parameters

In the hydrodynamic characterization experiments, the spar hydrodynamic coefficients are of primary interest. In point absorber design it is well understood that the float should be as buoyant as possible in order to ensure that its wave following tendency is maximized. As such, the performance limitations imposed by the float design stem from material selection, and structural design considerations and not the form of the hull or its hydrodynamic coefficients. For the SyncWave design concept, the hydrodynamic characteristics of the spar significantly impact the ability of the tuning system to adjust the natural frequencies of the machine's heaving oscillations. Consequently, it is the spar shape that is of most concern when generating the scale model design.

3.5 WEC Model Scaling

Given the wave regime of Hesquiaht Sound, an appropriate scaling method can be selected for the small scale wave tank and the WEC models being tested in it.

Geometric, or kinematic, scaling is a uniform scaling of the geometric parameters defining the WEC prototype. Kinematic scaling also applies to the fluid motions: the wave amplitudes, wavelengths and water depth should be defined by the geometric scaling factor. Once the geometric scale factor is selected, dynamic scaling tries to recover any dissimilarities in the wave excitation forces, between the scales, that drive the oscillations of the device components by adjusting other physical properties in the scale model test. To conduct a relevant assessment of WEC performance, the wave excitation force acting on the model components must be accurately reproduced and dynamic considerations result in a modification of model component geometries and masses. A number of dynamic scaling terms can be used, and the nature of the hydrodynamic phenomena that dominate the WEC motions dictates the choices made.

3.5.1 Dynamic Scaling Parameters

For fluid-body interaction problems there are three main scaling metrics that, when maintained between model and full scale device, can ensure at least a mode of dynamic similarity: Reynolds number, Froude number and Keulegan-Carpenter number. The Reynolds number defines the balance between the inertial and viscous forces in the fluid near the body and when maintained ensures that the flow separation and resulting drag forces are being properly modelled. Conserving the Reynolds number will guarantee that the viscosity induced effects are maintained. Reynolds scaling should be considered when separation induced effects like form drag and lift dominate the device dynamics. But, as the effects of viscosity are generally more significant in the boundary layer, it can often be assumed as negligible in scale models of WEC devices with simple streamlined geometries and small oscillating frequencies and heaving amplitudes.

$$\text{Re} = \frac{\rho U D}{\mu} \quad (3.1)$$

Where ρ is the fluid density, U is the velocity, D , is the characteristic length, and μ is the kinematic viscosity.

The Froude number, which is the ratio of inertial to gravitational forces, is used for free surface flows. Historically, Froude number scaling is used when comparing the resistance of bodies moving through a fluid, most commonly ships. As the inertial and gravitational forces are dominant for floating structures, it is the most commonly utilized scaling parameter for WEC devices [38, 16, 42]. Conserving the Froude number between model and prototype guarantees that gravitational forces are correctly scaled.

$$Fr = \frac{U}{\sqrt{gD}} \quad (3.2)$$

Where g is the gravitational constant.

The Keulegan-Carpenter (KC) number, a ratio between the drag and inertial forces, is the governing parameter for flow structures generated by bluff objects in oscillating flows or, conversely, oscillating bodies in still fluid. The KC number is commonly used in conjunction with the Stokes number, β , that relates the KC to the Reynolds number, so that $R_e = KC\beta$. A common use of the KC and Stokes numbers is found in [43]: where a vertical cylinder is oscillated horizontally in quiescent fluid and the fluid is evaluated using flow visualization. In [43] the generated vortices and flow separation are of major interest and are grouped by KC and Stokes numbers. Others have performed the scaling of surface piercing cylinders and Tension Leg Platforms (TLP's) [44] also utilizing the KC and the Stokes numbers.

The KC and the Stokes numbers are defined as follows

$$KC = \frac{2\pi A}{D} \quad (3.3)$$

$$\beta = \frac{D^2 f}{\nu} \quad (3.4)$$

Where A is the amplitude, f is the frequency and ν is the dynamic viscosity.

In order to have a scale model with exact dynamic similarity to the larger prototype, all three scaling metrics should be consistent between the WEC prototype and the scale model. However, it is nearly impossible to do so in most experimental setups without the use of a highly viscous fluid, or a vacuum. For wave energy converter studies, compromises in the dynamic scaling have to be made and the choice of scaling metric(s) will define its limitations.

3.5.2 Choice of WEC Spar Geometric Scaling factor

The normal desired range of scales in wave tanks for offshore structures in ocean engineering models and WEC's in particular wave tank is between 1:100 and 1:10 [38, 42]. As described earlier in §3.2, the maximum diameter of the model is to be 0.09m, which is a scale of approximately 1:65, when scaled to the maximum outer diameter of the float, D_3 , and falls within the recommended range. The spar geometry is of primary interest and maximizing the scale was considered. A standard material was required for the construction of the spar, where a tube outer diameter of 1 inch yielded a scale of 1:59 for the upper spar diameter, D_1 , and a tube outer diameter of 2.5 inches yielded a scale of 1:54 for the lower spar diameter, D_2 , therefore a scale of 1:55 was selected as a compromise scale value for the remainder of the physical geometric properties as was possible with the tank geometry and model construction materials. Table 12 lists the prototype dimensions for key geometric features in comparison to the selected model dimensions and the scale value, where the geometry is defined in Figure 16.

Table 12 Scaled Geometry Values

<i>Physical Parameter</i>	<i>Prototype Value</i>	<i>Model Value</i>	<i>Scale Value</i>
Spar Upper Diameter (D1)	1.5 m	2.54 cm (1.00 in)	1:59
Spar Upper Draft (T2)	3.65 m	6.64 cm	1:55
Spar Taper Angle	45°	48°	1:0.94
Spar Taper Draft (T3)	4.6 m	8.37 cm	1:55
Spar Lower Diameter (D2)	3.4 m	6.35 cm (2.5 in)	1:54
Spar Lower Draft (T4)	27.1 m	31.5 cm	1:86
Water Depth (H)	39 m	40.0 cm	1:97.5
Float Draft (T1)	1.6 m	2.9 cm	1:55
Float Diameter (D3)	5.84 m	8.89 cm (3.5 in)	1:65
Float and Spar Clearance	0.06 m	0.032 cm (1/8 in)	1:187.5
Bottom Clearance (H-T4-D2/2)	10.2m	5.0 cm	1:204

It is important to note the model features that do not satisfy the desired 1:55 scale factor. The spar upper and the spar lower diameters are not at scale factor, for the purpose of utilizing standard sized materials. The spar taper angle is subsequently not scaled 1:1 due to these differences. The taper draft scales are held at 1:55. The clearance between the float and spar is held to a reasonable manufacturable clearance of 1/8" (3.2 mm), whereas strict application of the geometric scale factor would have dictated a clearance of 1mm. The most important of the scaling inequalities is the total draft of the spar or more precisely the bottom clearance. The actual total draft of the model utilizing a 1:55 scale would be 0.52m, which is not possible in a 0.40m deep tank. To ensure that the model did not contact the bottom during tests, a required clearance minimum matching the maximum wave amplitude of 0.05m was applied. Overall, the approximate scale values are in the 1:55 range, where acceptable deviations from the exact scaling values have been adhered to.

3.5.3 Enforcing WEC Spar Dynamic Scaling

Viscous effects are generally neglected in numerical models, but are not being fully ignored in this work, with the inclusion of the c_v term. It would be of benefit to

consider that the Reynolds number scale method be utilized in order to accurately represent the viscous effects. However, “it is often impossible to conduct a laboratory investigation at a sufficiently large scale to fully eliminate viscous scale effects in some experiments such as the measurement of wave forces on a vertical pile” [39].

Past ocean engineering experiments using Reynolds scaling with a large scale factor experience significant scaling distortion and the model fluid is often laminar when the prototype would induce turbulent flow. The dominating effects in wave motion are pressure, gravity and inertia, therefore, Froude scaling is the accepted method for hydrodynamic modeling. Although, it is important to note that the viscous effects may exist and are not suitably scaled as with the small scale utilized in this work, the viscous effects may have a much greater influence than for the full scale model.

Froude scaling rather than Reynolds scaling also lends itself to a more realistic frequency domain for the wave tank as explained when considering the Stokes number.

Froude scaling commonly utilizes the term α to represent the geometric scaling ratio between the full scale and the model geometric parameters. The general method for determining the α influence on the Froude scaling is to equate the Froude number for the full scale and the model as shown in Equation (3.5) below, where subscript P and M refer to prototype and model respectively. The period, T , scale factor, can be determined by a rearrangement of Equation (3.6), where the dimensional value for period, time [T], is solved for with respect to the prototype and model values as shown in Equation (3.7). The common scale ratios for the kinematic wave regime are shown in Table 13.

$$\frac{U_M}{\sqrt{gD_M}} = \frac{U_P}{\sqrt{gD_P}} \quad (3.5)$$

$$U_P = U_M \sqrt{\frac{D_P}{D_M}} = U_M \alpha^{1/2} \quad (3.6)$$

$$\frac{\frac{D_P}{U_P} [T_P]}{\frac{D_M}{U_M} [T_M]} = \sqrt{\frac{D_P}{D_M}} = \alpha^{1/2} \quad (3.7)$$

Table 13 - Froude Scale Factors

<i>Parameter</i>	<i>Scale Factor</i>	<i>Units</i>	<i>Dimensional Units</i>
Wavelength (λ)	α	m	[L]
Frequency (ω)	$\alpha^{-1/2}$	rad/s	1/[T]
Period (t)	$\alpha^{1/2}$	s	[T]
Wave Height (h)	α	m	[L]

Utilizing the geometric scale factor of 1:55, the wavelength, frequency, period and wave height requirements for the fluid tunnel can be determined and are shown in Table 14. It can be seen that the wavelength scaled values are larger than what is desired as the wavelengths are exceeding tunnel length, of 2.5m. An acceptable experimental range in the test tank has been determined to be wavelengths ranging to a maximum of 2.5m. The experimental waveform is examined at wavelengths longer than 2.5m in order to determine suitability based on wave reflections in §5.2 and Appendix A.

In conjunction with the limits on the wave heights is the bottom interaction on the wave particle trajectories. As explained earlier, the deployment location of the WEC prototype is not considered deep water and the ocean floor is likely to affect the wave circulation. To properly dynamically scale the model, the bottom interaction should also be scaled. For the wave tank, this similarity can only be produced at an extremely small scale of approximately 1:100.

In order to accommodate the bottom clearance dynamic effects of the fluid particle motion on the model, the dispersion relation shown in Equation (3.8) is used to validate the test facility in relation to the prototype. The hyperbolic tangent function for

shallower water is a value less than 1, which can be compared between prototype and model values.

$$\omega^2 = gk \tanh(kd) \quad (3.8)$$

The model bottom interaction range contains a lower value than the prototype range due to the tank depth not scaling at 1:55. For the model, in order for the bottom interaction value to correspond to the prototype range exactly, wavelengths of minimum of 1.1m and a maximum of 2.25m are required. The model scale range is within a similar range to the prototype range and therefore the test facility can be used to represent the shallow water condition and the scaled model WEC. Wavelengths shorter than 0.3m will have fluid particle motion that is defined by deep water, and there would be no fluid particle motion at the bottom boundary.

Table 14 - Froude Scaled Wave Regime

<i>Wave Parameter</i>	<i>Prototype Range</i>	<i>Model Range (1:55)</i>
Wavelength (λ)	107-217 m	1.94-3.94m
Frequency (ω)	0.89-0.31 rad/s	6.6-2.3 rad/s
Period (T)	5-20 s	0.67-2.7 s
Wave Height (h)	1-3m	1.8-5.5 cm
Bottom Interaction $\tanh(2\pi d/\lambda)$	0.81-0.98	0.76-0.86

Chapter 4: Experimental Apparatus Specification

To complete a hydrodynamic characterization of the scale model WEC, tests have to be conducted that isolate the hydrodynamic effects that are defined by the parameters in Table 1 through Table 8. As is discussed in detail in §4.3, the schedule of experiments requires more than just a wave making apparatus. For the first set of experiments in quiescent fluid, the body will be displaced and allowed to oscillate freely and a model linear guide mechanism and displacement measurement device are required to maintain heave only motion. For the second set of experiments, where the body is forced to oscillate in quiescent fluid, a forcing mechanism, linear guide assembly and force measurement instrumentation are required. For the third set of experiments where the model is oscillated by a wave field, the wave making ability must be added to the model linear guide assembly and the force and displacement transducers. In this Chapter, the design of the wave maker, the WEC model forcing mechanism and the instrumentation suite are explained in detail.

4.1 Wave Maker Specifications

Ideally, the wave maker is to recreate the scaled wave regime of Hesquiaht Sound. Due to the UVIC fluid tunnel size and its use for other experiments, the wave maker was required to be compact and removable. As discussed earlier, the normal inlet of the fluid tunnel will become the beach for the wave experiments to utilize the wave damping potential of the honeycomb section. To maximize the portion of the fluid tunnel length available for the test section, it was also necessary to use the fluid tunnel's outlet diffuser to house the wave making apparatus.

There are three main types of wave makers used in small scale experiments; the flap or hinged plate, the piston and the heaving body. Each is found to create different wave characteristics. The flap gives a deep water wave type with exponential velocity decay towards the tank bottom; the piston gives a shallow water wave type with a relatively

linear velocity decay; the wave circulation profiles produced by a heaving body type of device are sensitive to the frequency of oscillation and the stroke length. Each method of wave generation can be seen in Figure 17.

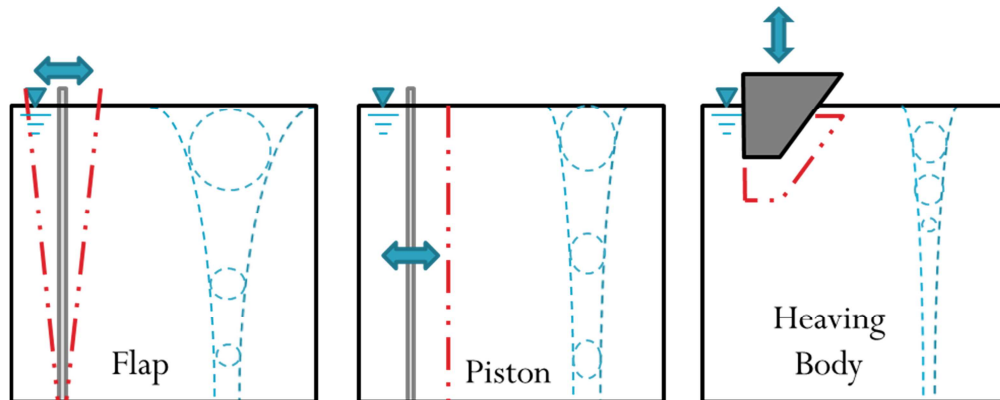


Figure 17 - Wave Maker Types.

The dashed lines surrounding the wave maker body represent the wave maker motion, while the dashed lines on the right of the diagram represent the fluid particle motion and the motion decay with depth.

A modified piston flap wave-maker has been argued to better replicate real ocean wave scenarios as shown in Figure 18 [38]. But, for the small scale WEC experiments, and limited tank dimensions considered in this work, a simplified architecture was desired, and the modified piston flap and heaving body designs were eliminated. As discussed earlier in §3.3, the Hesquiaht Sound regime is not considered to be deep water as the water depth is not more than half the wavelength, and therefore the piston type wave maker was considered the ideal option for the small scale testing facility.

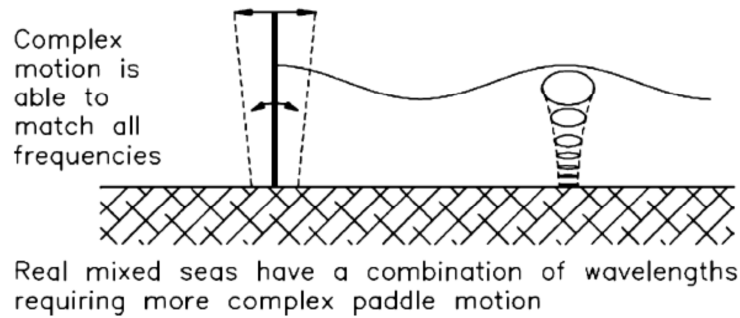


Figure 18 - Modified Piston Flap Wave maker [38]

In sizing the piston style wave maker, the piston face should eclipse the largest expected wave height being produced. The maximum allowable wave height as determined in §3.2 is 10cm for a fluid depth of 40cm. A minimum piston face height of 50cm from the bottom of the 40cm deep tank was desired in order to allow an additional 5cm of clearance to allow for sloshing.

Other wave-maker design criteria include the stroke, power and force required to make waves for a piston type wave-maker. The required stroke, S , was calculated for a piston wave-maker using Equation (4.1) from [15].

$$\frac{H}{S} = \frac{2(\cosh(2kd) - 1)}{\sinh(2kd) + 2kd} \quad (4.1)$$

Where H is the wave height, d is the water depth/piston depth, and k is the wave number as calculated in Equation (2.15) for shallow water. The stroke requirements for the 1:55 scale waves are shown below in Table 15. Results for waves ranging from 1cm to 10cm in height and periods ranging from 0.73s to 2.7s are shown, where the desired experimental range is highlighted in bold. The wave height to stroke ratio versus relative depths is plotted in Figure 19 for the piston type wave maker. Relative depth, kd , is a ratio between the water depth and wavelength.

Table 15 - Stroke requirements (mm) over range of wave heights (m) and periods(s)

Stroke (mm)		T (s)									
		0.73	0.94	1.16	1.37	1.58	1.79	2.00	2.20	2.40	2.70
H (m)	0.01	0.6	0.4	0.3	0.3	0.3	0.4	0.6	1.5	4.8	20.7
	0.02	1.3	0.8	0.6	0.6	0.6	0.8	1.2	3.0	9.6	41.3
	0.03	1.9	1.2	0.9	0.9	1.0	1.3	1.9	4.4	14.3	62.0
	0.04	2.6	1.6	1.2	1.2	1.3	1.7	2.5	5.9	19.1	82.6
	0.05	3.2	2.0	1.5	1.4	1.6	2.1	3.1	7.4	23.9	103.3
	0.06	3.9	2.4	1.8	1.7	1.9	2.5	3.7	8.9	28.7	123.9
	0.07	4.5	2.8	2.1	2.0	2.3	2.9	4.3	10.4	33.4	144.6
	0.08	5.2	3.2	2.4	2.3	2.6	3.4	5.0	11.8	38.2	165.2
	0.09	5.8	3.6	2.7	2.6	2.9	3.8	5.6	13.3	43.0	185.9
	0.1	6.5	4.0	3.0	2.9	3.2	4.2	6.2	14.8	47.8	206.5

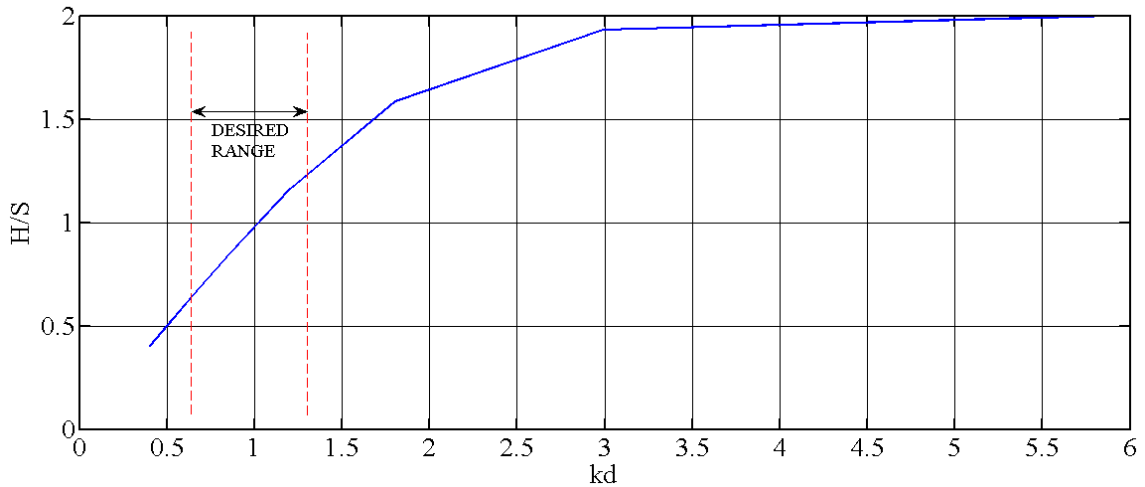


Figure 19 - Piston Wave-maker: Wave Height to Stroke ratios versus relative depths

The power requirement was calculated from the non-dimensional power curve from [15], and determined to be $0.06W$ to $1.7W$ maximum for the range of scaled conditions for a piston wave-maker. From the power curve it is identifiable that the peak power requirement is required at a value of kd of approximately 1.5, which for this tank corresponds with a wavelength of 1.68m, which is smaller than the desired wavelength for these experiments. The reproduced power curve can be seen in Figure 20.

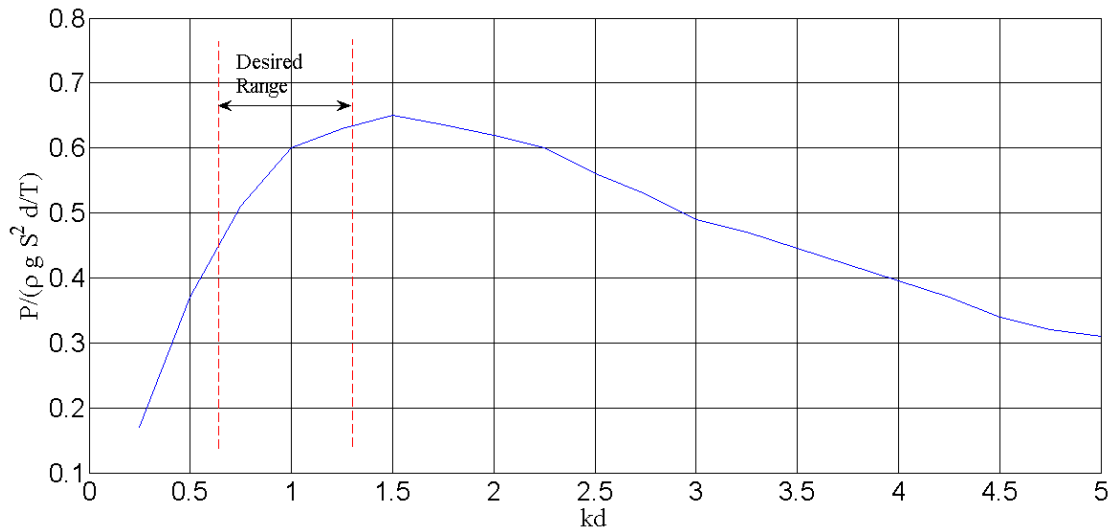


Figure 20 - Piston Wave-maker: Dimensionless mean power as a function of water depth

As mentioned, the wave-maker needs to be easily removed from the fluid tunnel, and without compromising the current making abilities of the tank. This requirement led to a wet-back design, meaning that there is fluid on both sides of the piston. In order to maintain a parallel motion at both the top and bottom areas of the piston, a dual plate structure has been designed for the piston head to ensure structural integrity. To prevent back waves being generated behind the wave-maker, a secondary volume displacement shell was implemented inside the outlet diffuser space which moves in heave in conjunction with the piston travel. The interactive motion between the piston body and volume displacement box is shown in Figure 21. Figure 22, describes the major components of the wave maker including the guides and volume displacement box. The forced piston motion is generated from a ball screw linear actuator, attached through bolted plates to the volume displacement box. The volume displacement box is connected to the piston body via linear ball bearings and precision shafts on a 45° angle, so that the vertical displacement of the volume displacement box equals that of the horizontal displacement of the wave maker's piston face. To maintain the vertical motion of the displacement box, additional precision linear shafts and bearings were used. The piston's horizontal motion is maintained by another set of precision linear

shafts and bearings attached to the bottom of the linear actuator support plate and the front piston plate.

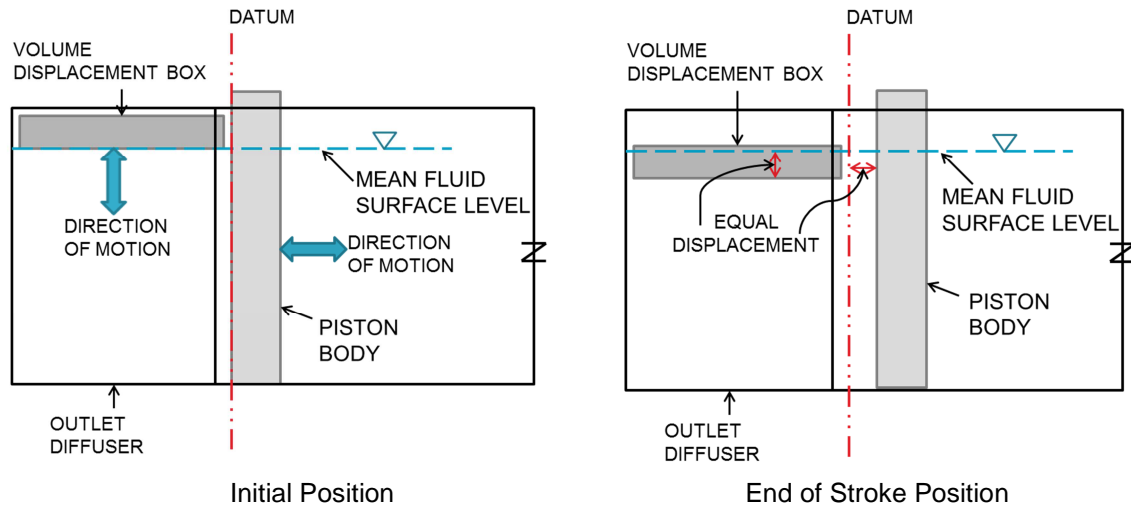


Figure 21 - Volume Displacement Box and Piston Face Motion

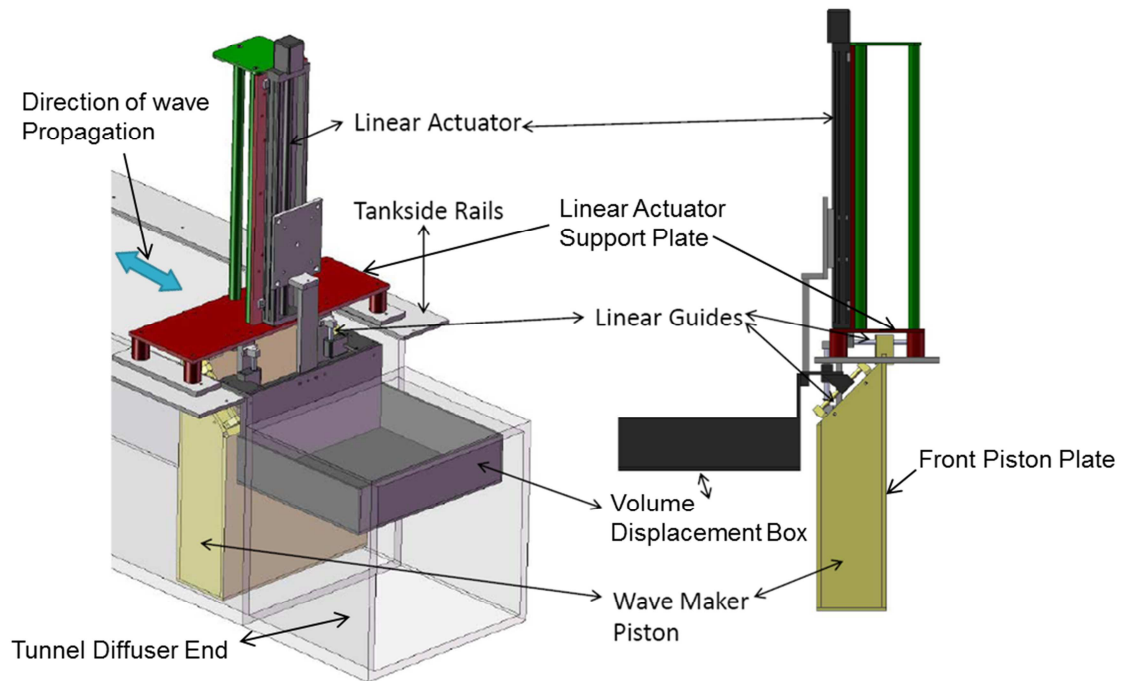


Figure 22 - Wave Maker 3D Model

The wave maker setup in the UVIC fluid tunnel can be seen in Figure 23. The wave maker piston and volume displacement box were constructed from clear plexi-glass (lexan) with individual panels epoxied to prevent fluid penetration.

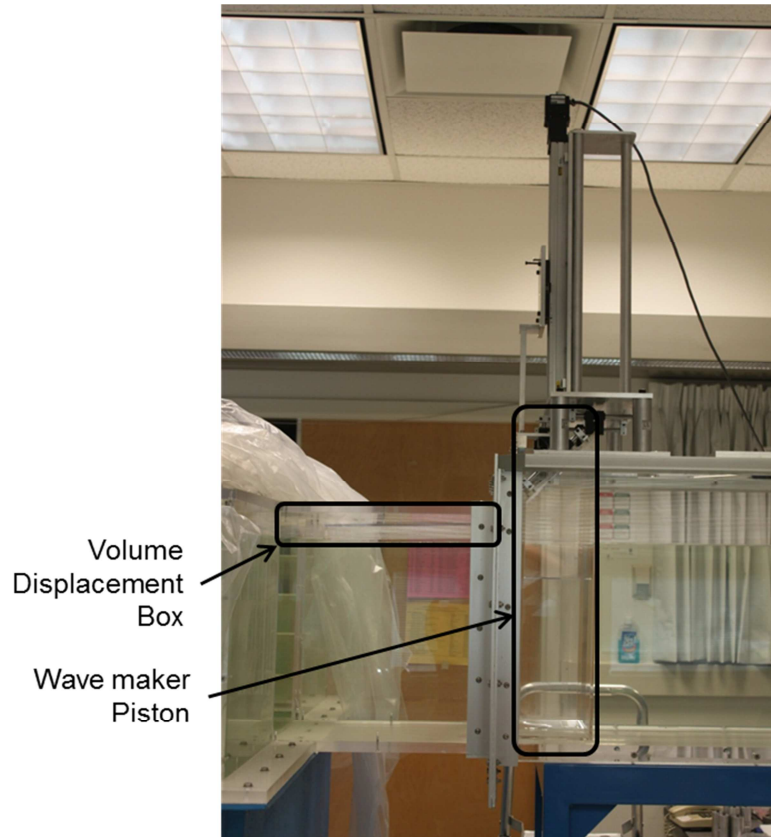


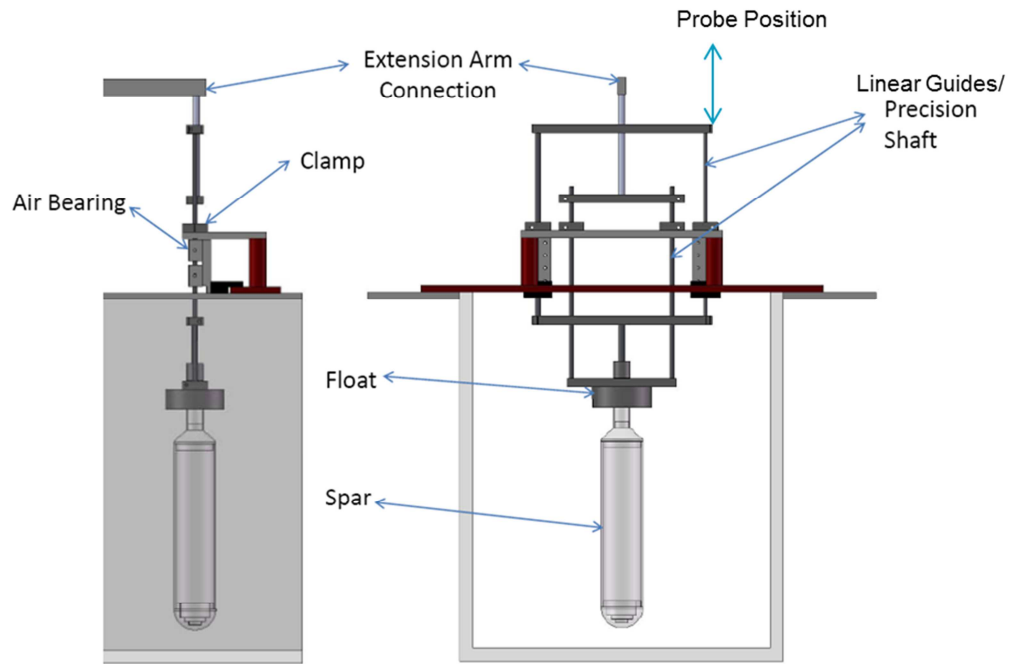
Figure 23 - Wave Make Setup

4.2 Scale Model WEC Forcing Mechanism

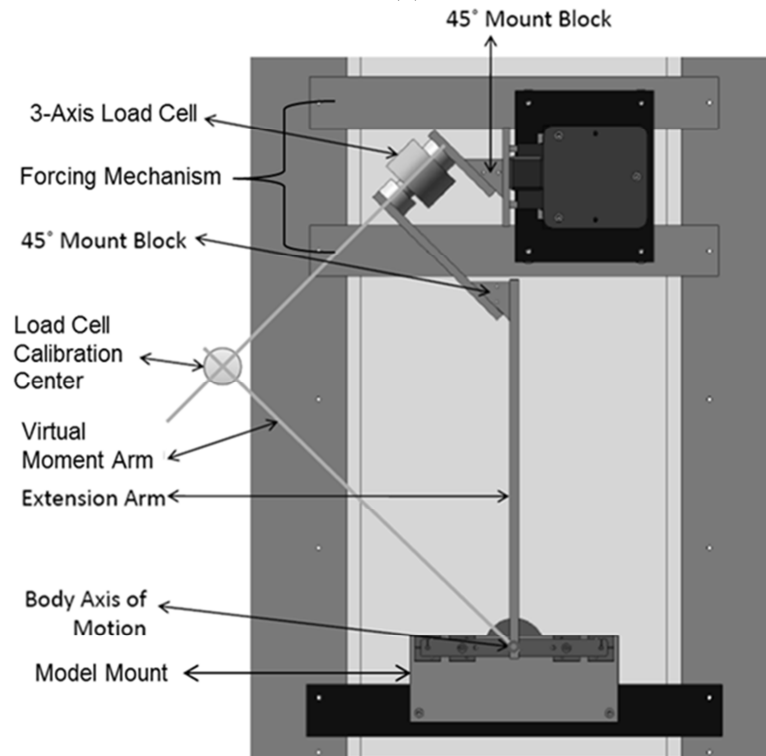
The experiments in quiescent fluid require the model to be oscillated in a sinusoidal motion with amplitude that matches the expected scaled converter motions in order to determine the hydrodynamic coefficients that define the reaction forces. The heave motion is generated by a ball screw linear actuator, the same actuator used for the wave maker, driven by a stepper motor programmed to rotate in a sinusoidal mode. The actuator is connected to the spar body through a rigid connection formed by the load cell and the extension arm.

To maintain the desired heave only motion of the spar model, linear guides are necessary. In order to eliminate as much friction as possible, two precision shafts are supported by linear air bushings. The shafts are attached rigidly to an extension arm that in turn is connected to the actuator by a load cell. Air bushings were selected due to the high damping experienced with standard linear ball bearings. Four 0.25" Nelson Air Corp Air Bearings are used, two per precision linear shaft. Each bearing is rated at 6N when 60psi air is supplied.

Figure 24(a) shows the side view from outside the test tunnel and the front view from the tunnel end of the model guides and mounting apparatus. The precision shafts, clamps, air bushings, float and spar as well as probe position are also shown. Figure 24(b) shows the top view of the linear guide mounts and also includes the forcing mechanism. The position and orientation of the load cell is discussed in the next section. The forcing mechanism is shown in Figure 26.



(a)



(b)

Figure 24 - WEC Model Mount and Forcing Mechanism

(a) Linear Guides for WEC Models (b) Forcing Mechanism Moment Arm Connections

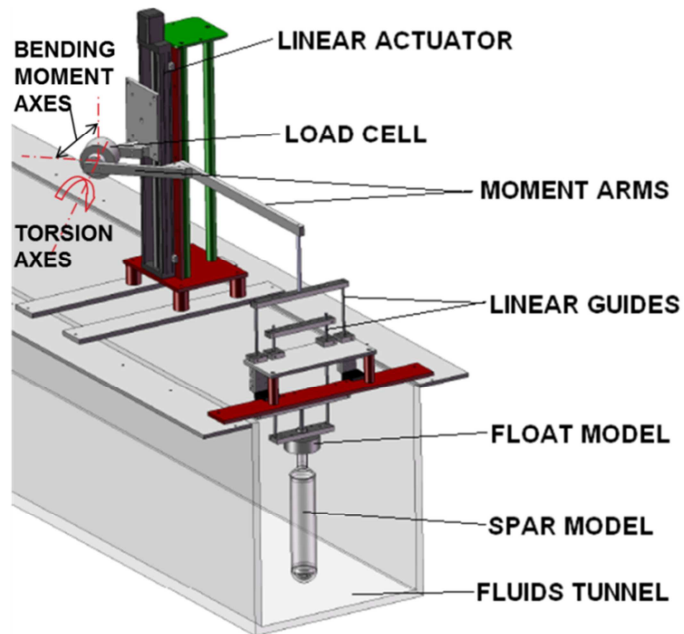


Figure 25 - Combined view of linear guides and WEC Model with Linear Actuator.

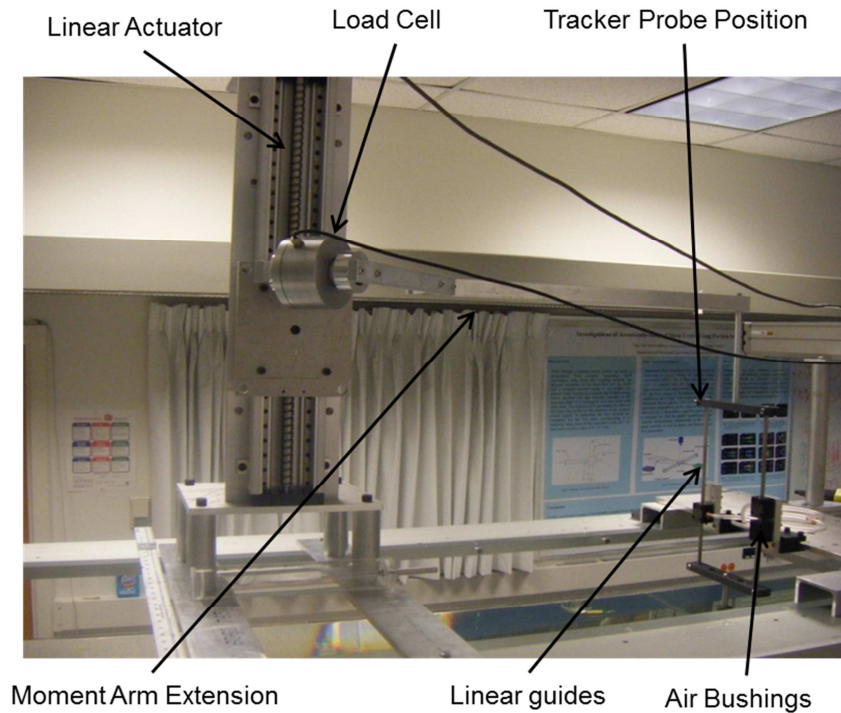


Figure 26 – Scale model WEC Forcing Mechanism

4.3 Measurements and Instrumentation

4.3.1 Force Measurement

In order to determine the hydrodynamic coefficients for both the excitation and reaction forces, a three-axis load cell, model F233-Z3712 from Novatech Measurements Ltd, was used as shown in Figure 27. The load cell measures moments produced about three orthogonal axes, two bending moments and a torque. The load cell is used on its side such that the vertical force delivered to a long moment arm by the spar model creates a relatively large input to the torque axis. The load cell had been calibrated for a previous project to have a load centre 30cm removed from the intersection of the bending moment axis of the load cell and the location of this calibration centre set the length of the moment arm and the relative position of the model and load cell as shown in Figure 24(b). The load cell was connected to the LabView software through a 16-bit resolution USB digital acquisition model (DAQ). The output of the torsional load cell is in N-m with the range and accuracy listed in Table 16. Only the torsional data was utilized, and the data received was converted to the effective vertical load simply by dividing by the moment arm length.

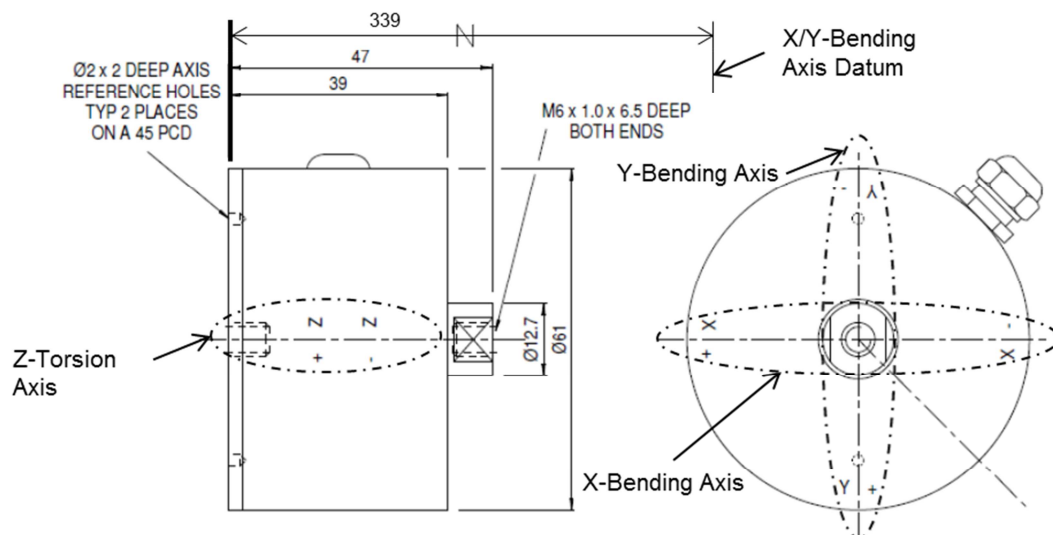


Figure 27 - Load Cell Arrangement

The calibration of the force measurement system was conducted in water with the moment arm and linear guide shafts and model installed. This gave a baseline measurement for the system without the hydrodynamic excitation or reaction forces present. A zero load configuration was used where the actuator was positioned so that the spar model exerted no net buoyant force or weight on the load cell in order to remove bias from the collected measurements. The linearity of the measurements was initially validated by a series of static displacements of the model, and a comparison of the calculated change in buoyancy with respect to the measured change in loading.

4.3.2 Displacement Measurement

Along with force measurements, accurate position measurements are desired to track the heave displacement, velocity and acceleration of the scale model. The displacement measurement system selected for use was a 3D motion capture camera referred to as VisualEyz, produced by Phoenix Technologies Incorporated. The VisualEyz tracker probes were connected to an accessible moving component of the WEC model, as shown in Figure 24(a), and the linear motion was recorded using the VisualEyz software. The accuracy and range for the displacement measurements can be seen in Table 16.

4.3.3 Wave Measurement

The wave elevation profile was also measured to determine the actual wave field generated by the wave maker. An RBR Ltd WG50 capacitance two wire wave gauge was selected specifically for the wave regime at the testing facility. The probe's scale and accuracy are detailed in Table 16.

The force, wave and displacement data were each collected separately, and aligned manually for each individual trial as the existing programs used did not allow for amalgamation.

Table 16 - Measurement Tool Specifications

<i>Wave Gauge Specification</i>	<i>Value</i>
Probe Length (wave height)	16cm (± 8 cm)
Accuracy	$\pm 0.4\%$
<i>Load Cell Specification</i>	<i>Value</i>
Z-axis Range	± 0.3 N-m
Accuracy	± 0.0001 N-m
<i>VisualEyez Specification</i>	<i>Value</i>
Measurement Range - Displacement	0.01mm
Accuracy	± 0.12 mm

4.4 Experimental Procedures

The following sections describe the experimental procedures used to determine the hydrodynamic coefficients of the scaled WEC model. The procedures included a free naturally damped body in quiescent fluid, a sinusoidal motion forced body in quiescent fluid, and a body fixed and freely oscillating in a wave field. Additionally, there are three model geometries that are considered: a simple cylinder, the scaled model spar and the scale model spar with the concentric float. Although the modeled float is to scale, it would have required exotic material selections in order to model the buoyancy of the full scale device. In this work, the float is constructed from readily available materials and is held fixed in place when included in the tests. This was allowable since the spar hydrodynamics were of much greater interest.

4.4.1 Natural Oscillations in Quiescent Fluid

When a body is displaced in quiescent fluid and allowed to return naturally to its equilibrium position, it will oscillate at a damped frequency, easily related to its natural frequency. This is the simplest method of determining hydrodynamic coefficients for added mass and damping from Equation (2.29) for the reactive forces, but can only provide results at the natural frequency. This decay curve test was utilized by Bracewell in [36] to determine hydrodynamic coefficients over a range of frequencies

by changing the natural frequency of the body through the addition of a springs and masses. The first set of experiments involves displacing the body in question and allowing it to oscillate naturally. The heave response such as the example shown Figure 28, is utilized with Equations (4.9) through (4.15) to determine the natural frequency, which can then be used to determine the added mass. The decay of the curve from $\xi(t_1)$ to $\xi(t_2)$ is used to determine the damping ratio of the system.

Starting with the equation of motion of a single floating body as derived in §2.4.1:

$$\hat{a}_{11}\ddot{\xi} + \hat{b}_{11}\dot{\xi} + \hat{S}_1\xi = m_1\ddot{\xi} \quad (4.2)$$

Assume $\xi = Ce^{st}$ then:

$$(m_i + \hat{a}_{ij})s^2 + \hat{b}_{ij}s + \hat{S}_i = 0 \quad (4.3)$$

The solutions are

$$s_{1,2} = -\frac{\hat{b}_{11}}{2(m_1 + \hat{a}_{11})} \pm \sqrt{\left(\frac{\hat{b}_{11}}{2(m_1 + \hat{a}_{11})}\right)^2 - \frac{\hat{S}_1}{(m_1 + \hat{a}_{11})}} \quad (4.4)$$

Where critical damping, b_c , is defined as the value that sets the square root term equal to 0.

$$\left(\frac{\hat{b}_c}{2(m_1 + \hat{a}_{11})}\right)^2 - \frac{\hat{S}_1}{(m_1 + \hat{a}_{11})} = 0 \longrightarrow \hat{b}_c = 2(m_1 + \hat{a}_{11})\omega_n \quad (4.5)$$

The damping ratio is

$$\zeta = \frac{b}{b_c} \quad (4.6)$$

For this work we can assume an underdamped system for the case where $\zeta < 1$. Equation 4.4 becomes

$$s_{1,2} = (-\zeta \pm \sqrt{\zeta^2 - 1})\omega_n \quad (4.7)$$

The solution to Equation 4.2 becomes

$$\xi(t) = C_1 e^{s_1 t} + C_2 e^{s_2 t} = C_1 e^{-\zeta\omega_n t} e^{i\sqrt{1-\zeta^2}\omega_n t} + C_2 e^{-\zeta\omega_n t} e^{-i\sqrt{1-\zeta^2}\omega_n t} \quad (4.8)$$

The damped frequency ω_d is the observed cyclic frequency and is defined as

$$\omega_d = \omega_n \sqrt{1 - \zeta^2} \quad (4.9)$$

Then applying initial conditions Equation 4.8 yields

$$\xi(t) = e^{-\zeta\omega_n t} \left(\xi_0 \cos \omega_d t + \left(\frac{\dot{\xi}_0 + \zeta\omega_n \xi_0}{\omega_d} \right) \sin \omega_d t \right) \quad (4.10)$$

When considering two points in time separated by a single period.

$$\tau_d = t_2 - t_1 = \frac{2\pi}{\omega_d} \quad (4.11)$$

$$\frac{\xi_1}{\xi_2} = e^{\zeta\omega_n \tau_d} \quad (4.12)$$

The damping ratio ζ can be determined from the logarithmic decrement δ

$$\delta = \ln \frac{\xi_1}{\xi_2} = \frac{2\pi\zeta}{\sqrt{1-\zeta^2}} \quad (4.13)$$

The added mass term can then be determined from the natural frequency.

$$\hat{a}_{11} = \frac{\hat{S}_1}{\omega_n^2} - m_1 \quad (4.14)$$

The lumped parameter damping coefficient b_{ij} is found from a rearrangement and combination of Equations (4.5), (4.6) and (4.13).

$$\hat{b}_{11} = 2\zeta\omega_n(m_1 + \hat{a}_{11}) \quad (4.15)$$

Each model arrangement; cylinder, spar and spar with float was tested 4 times. The number of peaks used to calculate the hydrodynamic coefficients was 15 for the cylinder and spar arrangements, but only 7 for the spar with concentric float arrangement as the oscillations did not continue past 7 peaks. The results are summarized in the plots of §5.3.1, §5.4.1 and §5.5.1.

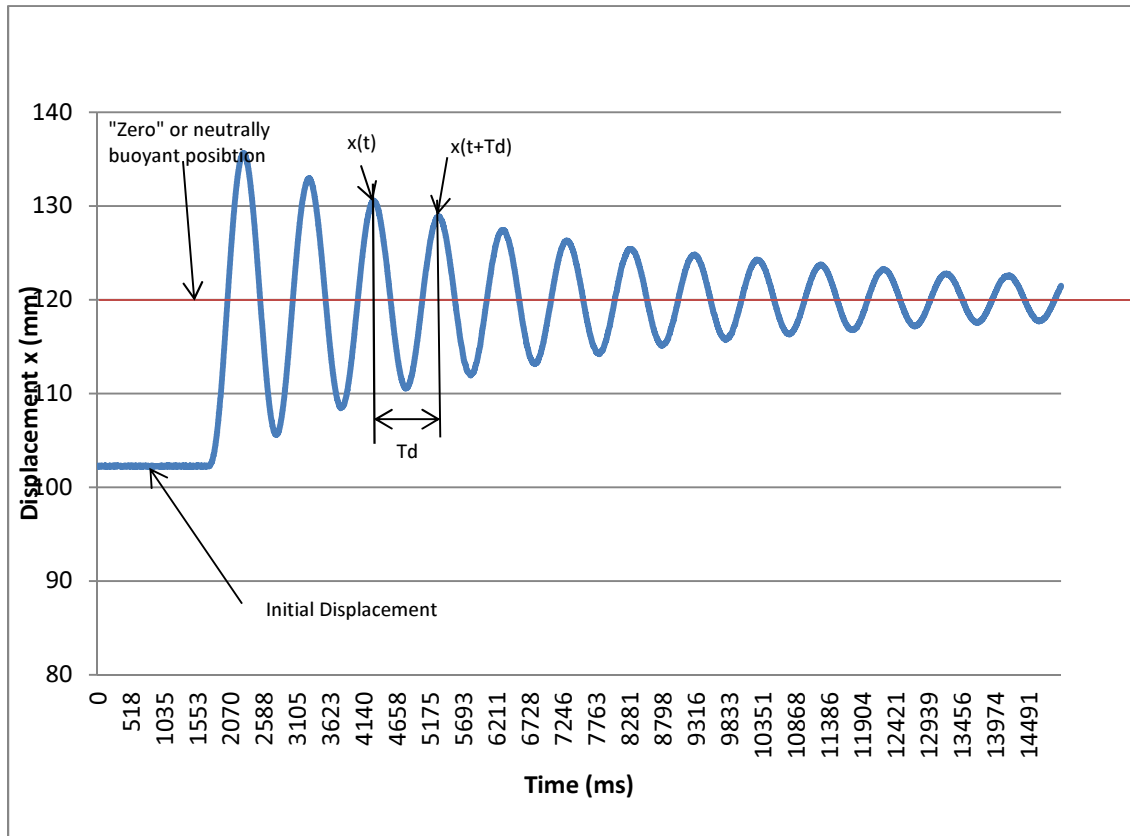


Figure 28 - Natural Decay Curve for a sample spar test.
A case where the spar was initially displaced 1.8cm and then allowed to freely oscillate and return to its neutrally buoyant position.

The hydrodynamic coefficients resolved utilizing this method are defined in Table 17.

Table 17 – Natural Oscillation Experimental Reaction Coefficients

<i>Parameter</i>	<i>Description</i>
\hat{a}_{cyl}	Added mass of Cylinder in reaction (1-DOF System only)
\hat{b}_{cyl}	Radiation damping coefficient for Cylinder in reaction
\hat{a}_{11}	Added mass of Spar-only model in reaction
\hat{b}_{11}	Radiation damping coefficient for Spar-only model in reaction
\hat{a}_{12}	Added mass of Spar-float model in reaction
\hat{b}_{12}	Radiation damping coefficient for Spar-float model in reaction

4.4.2 Forced Oscillations in Quiescent fluid

By measuring the driving force experienced during forced oscillations of the scale model in quiescent fluid, the hydrodynamic coefficients for added mass and damping from the reaction forces can be found. Referring to the equation of motion

$$(m_1 + \hat{a}_{ij})\ddot{\xi} + \hat{b}_{ij}\dot{\xi} + \hat{S}_{ij}\xi = F_{measured} \quad (4.16)$$

When the acceleration is zero, there is only a damping force and stiffness present. The stiffness force can be calculated based on the measured heave displacement of the body. Similarly, when the velocity is zero, there is only one unknown inertial force. Figure 29 shows both the displacement and the force measurement recorded during the forced oscillation of the spar model. This figure also shows the instances of zero acceleration and zero velocity that were used to calculate the coefficients.

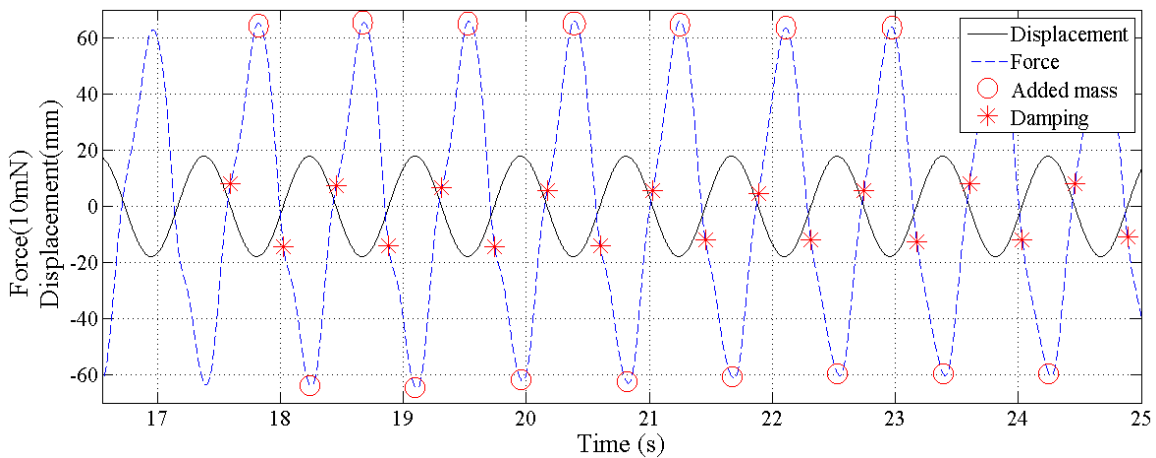


Figure 29 – Model Displacement and Force data used in identification of Reaction Force coefficients

A sample of the displacement, velocity and acceleration data output from the 3D camera, VisualEyez, as well as the filtered signal is shown in Figure 30, Figure 31 and Figure 32. A low pass filter was written into the Matlab code for use during the data processing stage. The velocity data was filtered using a low pass filter with a cut-off

frequency of 0.2 Hz, while the acceleration data was filtered using a low pass filter with a cut-off frequency of 2 kHz.

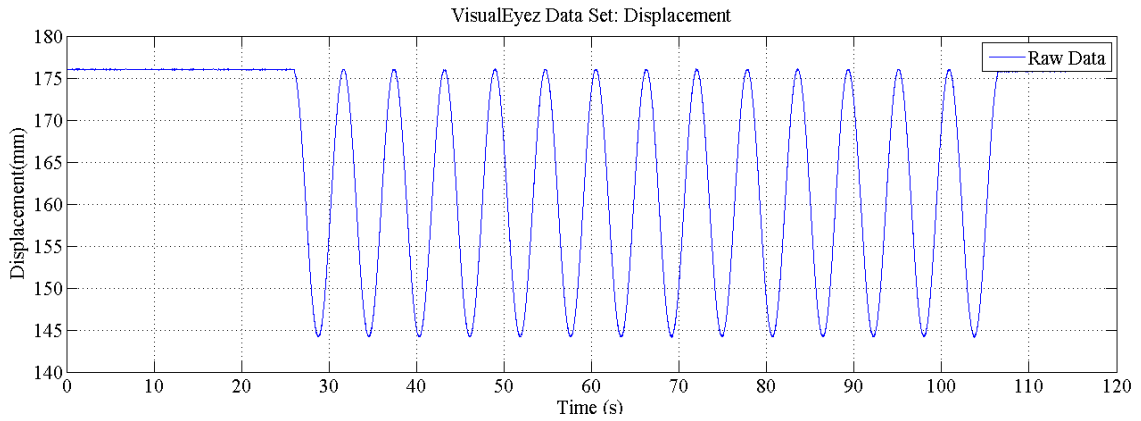


Figure 30 - VisualEyez: Displacement

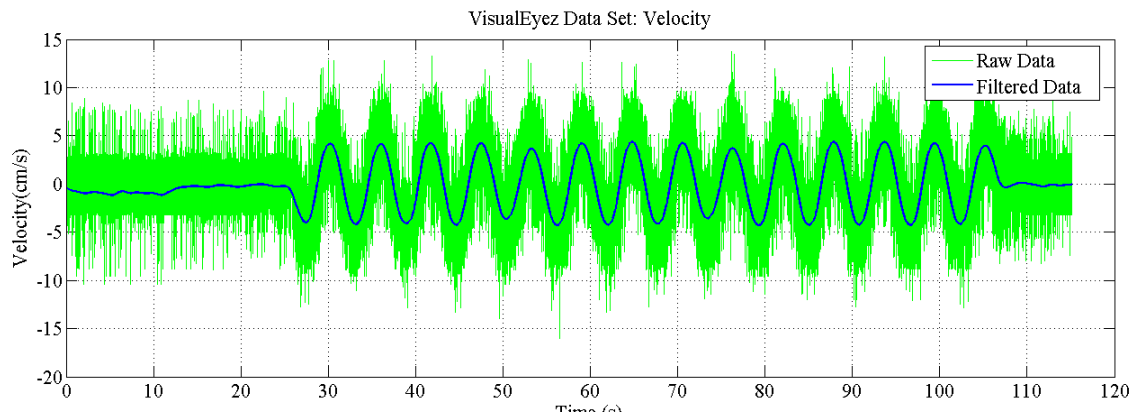


Figure 31 - VisualEyez: Velocity

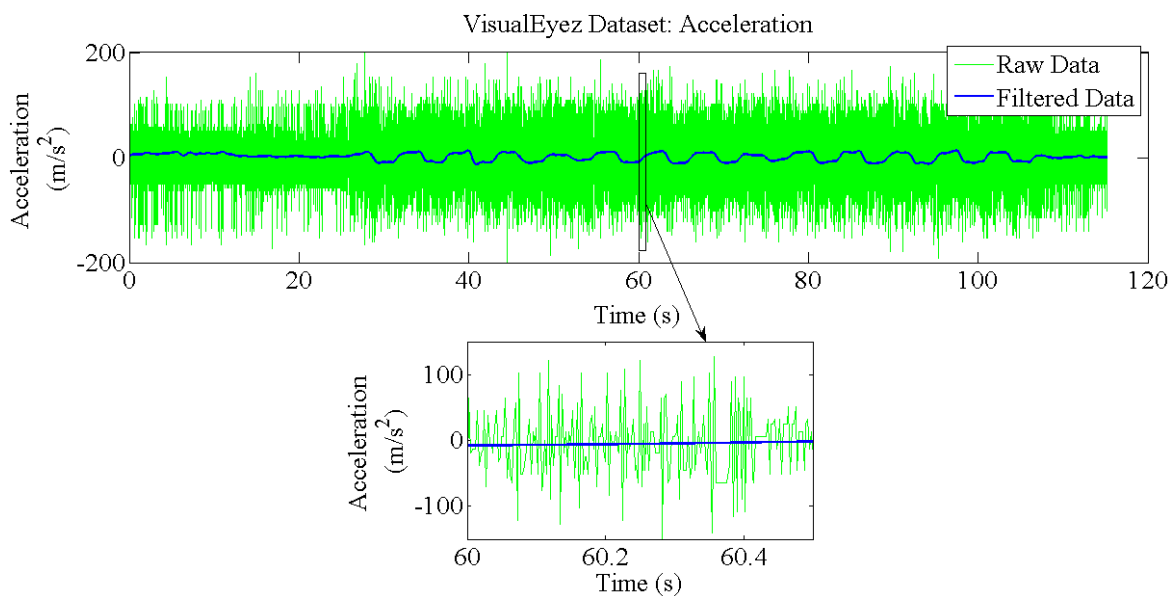


Figure 32 - VisualEyz: Acceleration

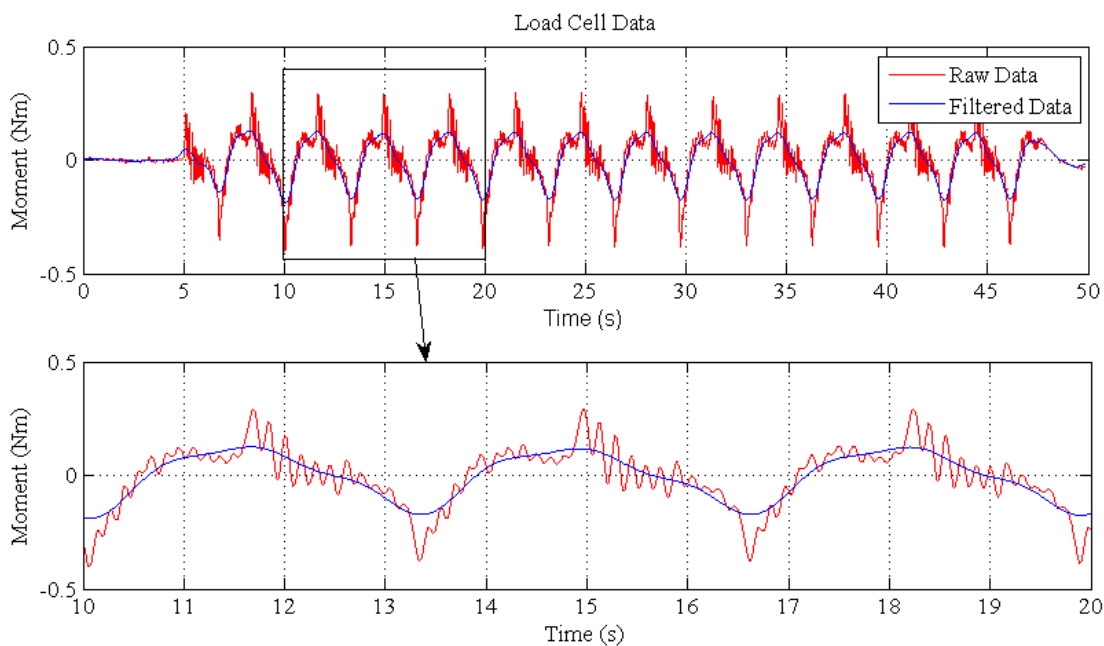


Figure 33 - Load Cell Torsion Data

A sample of the force data output from the Labview software, as well as the filtered signal is shown in Figure 33. A low pass filter was written into the Matlab code for use during the data processing stage. The force data was filtered using a low pass filter with a cut-off frequency of 0.2 Hz.

Tests were repeated for each geometry and different frequencies and the collective data was combined to form a description of the parameters frequency dependence.

The same methodology was used for determining hydrodynamic coefficients for the reactionary damping and added mass forces for all the body geometries considered. As discussed previously, the float is held fixed when included with the scale model spar and therefore the equation of motion for the multi-body is similar to the single body system, except that the lumped parameters being resolved include the induced terms.

The hydrodynamic coefficients resolved utilizing this method are defined in Table 18.

Table 18 – Forced Oscillation Experimental Hydrodynamic Coefficients

<i>Parameter</i>	<i>Description</i>	<i>Desired Frequency Range</i>
\hat{a}_{cyl}	Added mass of Cylinder in reaction	2.3-6.6 rad/s
\hat{b}_{cyl}	Radiation damping coefficient for Cylinder in reaction	2.3-6.6 rad/s
\hat{a}_{11}	Added mass of Spar-only model in reaction	2.3-6.6 rad/s
\hat{b}_{11}	Radiation damping coefficient for Spar-only model in reaction	2.3-6.6 rad/s
\hat{a}_{12}	Added mass of Spar-float model in reaction	2.3-6.6 rad/s
\hat{b}_{12}	Radiation damping coefficient for Spar-float model in reaction	2.3-6.6 rad/s

4.4.3 Wave Excitation Forces on a fixed body

In order to determine the hydrodynamic coefficients for excitation forces on a fixed body in a generated wave field, both the force and wave amplitude are measured. The data from both transducers was then combined. From this data we can again utilize the methodology given in §4.4.2, where the body displacement is replaced by the wave free surface displacement; determining the hydrodynamic coefficients requires the ability to segregate the points of zero velocity and zero acceleration of the wave free surface. Referring to Equation (2.23) in §2.3.1, the equation of motion utilized in solving the excitation force coefficients is

$$(m_i + \tilde{a}_{ij})\ddot{\eta} + (\tilde{b}_{ij})\dot{\eta} + \tilde{S}_{ij}\eta = F_{measured} \quad (4.17)$$

The recorded data from the load cell was utilized in determining the measured force values utilized in the calculations of the added mass and damping coefficients. The wave elevation, velocity and acceleration data can be seen both raw and filtered in Figure 34, Figure 35 and Figure 36. A low pass filter was written into the Matlab code for use during the data processing stage. The wave free surface elevation data was filtered using pass filter with a cut-off frequency of 0.2 Hz. The wave free surface elevation velocity and acceleration were calculated from the filtered wave height data using a finite difference formulation, then a low pass filter was applied. The wave free surface velocity was filtered using a low pass filter with a cut-off frequency of 0.2 Hz, and the wave free surface acceleration was filtered using a low pass filter with a cut-off frequency of 0.2 Hz.

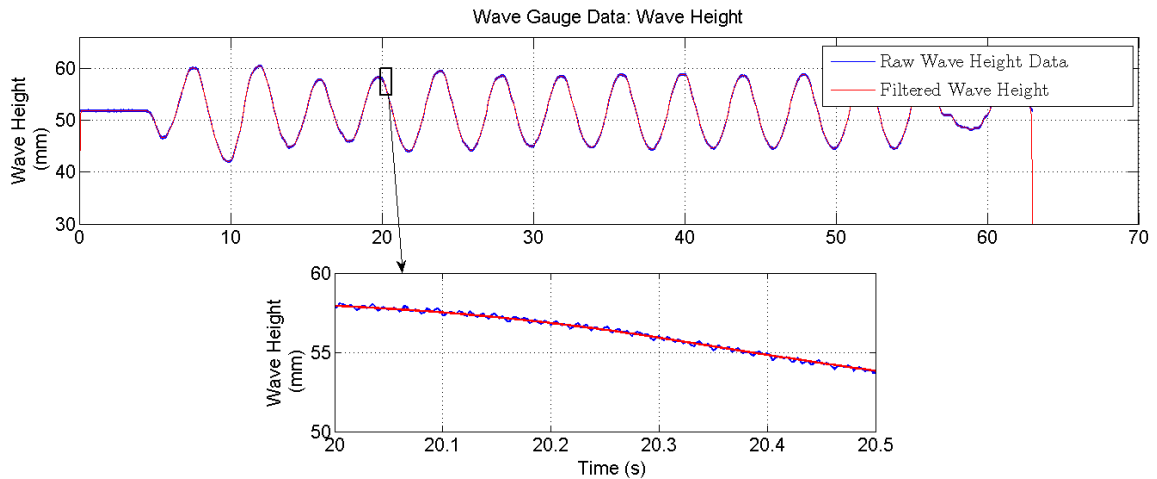


Figure 34 - Wave Gauge Data

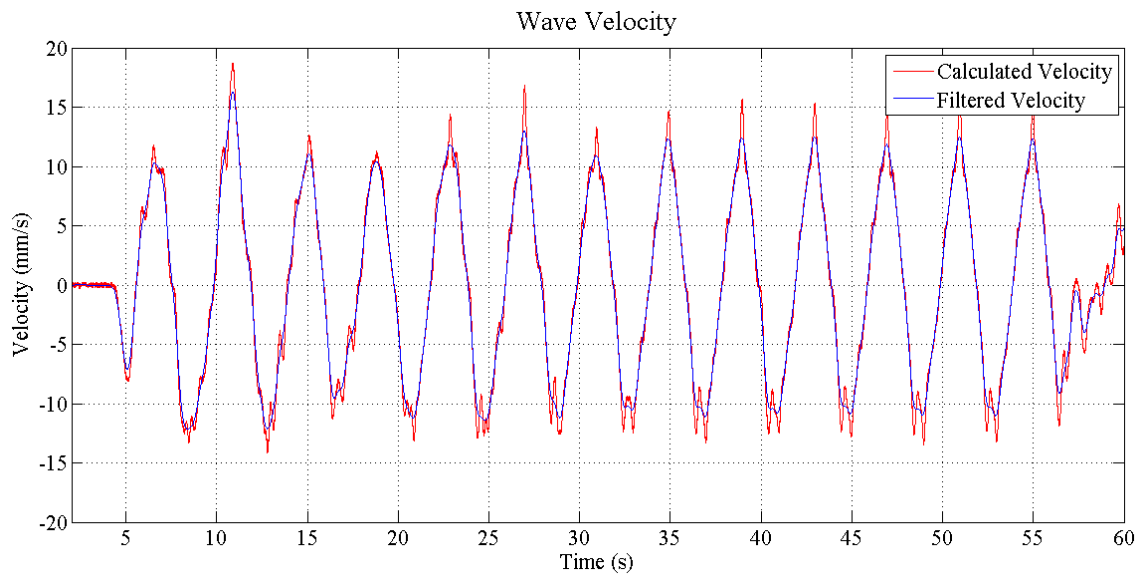


Figure 35 - Calculated Wave Free Surface Velocity

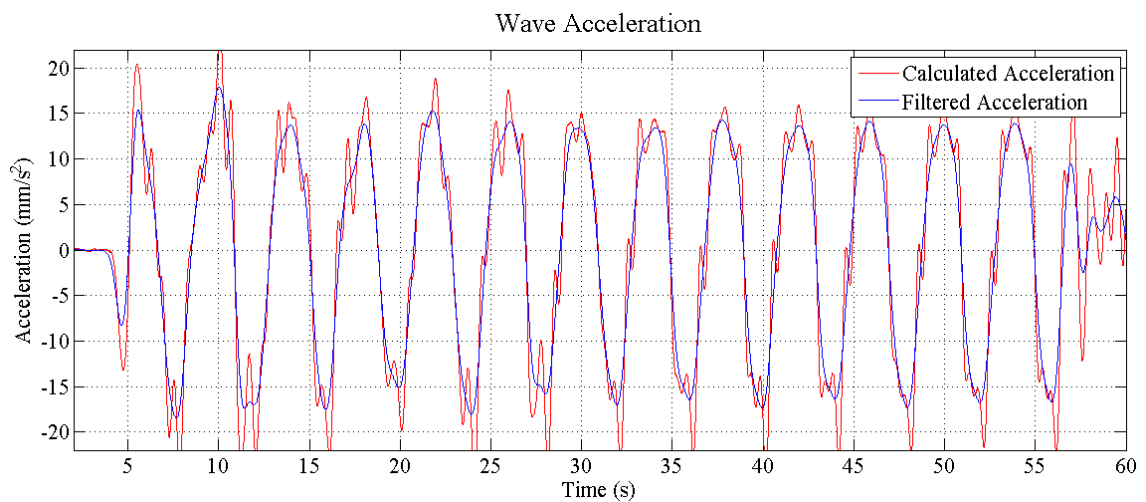


Figure 36 - Calculated Wave Free Surface Acceleration

The setup for the wave field experiments can be seen in Figure 37. The wave maker and linear actuator can be seen on the left end of the fluid tunnel. The load cell is fixed in place roughly in the middle of the tank, with the extension arm attached extending out to the right where the spar is affixed extending downwards into the fluid tunnel. The wave gauge is affixed 10cm ahead of the body. The force and wave data sets were recorded separately and combined afterwards by manually inspecting the data sets for

the trigger point of an event with a nominal sign of an initial reading; this point was used to synchronize the time series and compensates for the displacement between the wave gauge and model.

In behind the tank, the 3D camera can be seen on its tripod with three lenses, which is used in the wave experiments as discussed in §4.4.4.

The same methodology was applied for all model geometries considered. For the combined Spar-Float tests, the lumped parameters identified include the induced coefficient values.

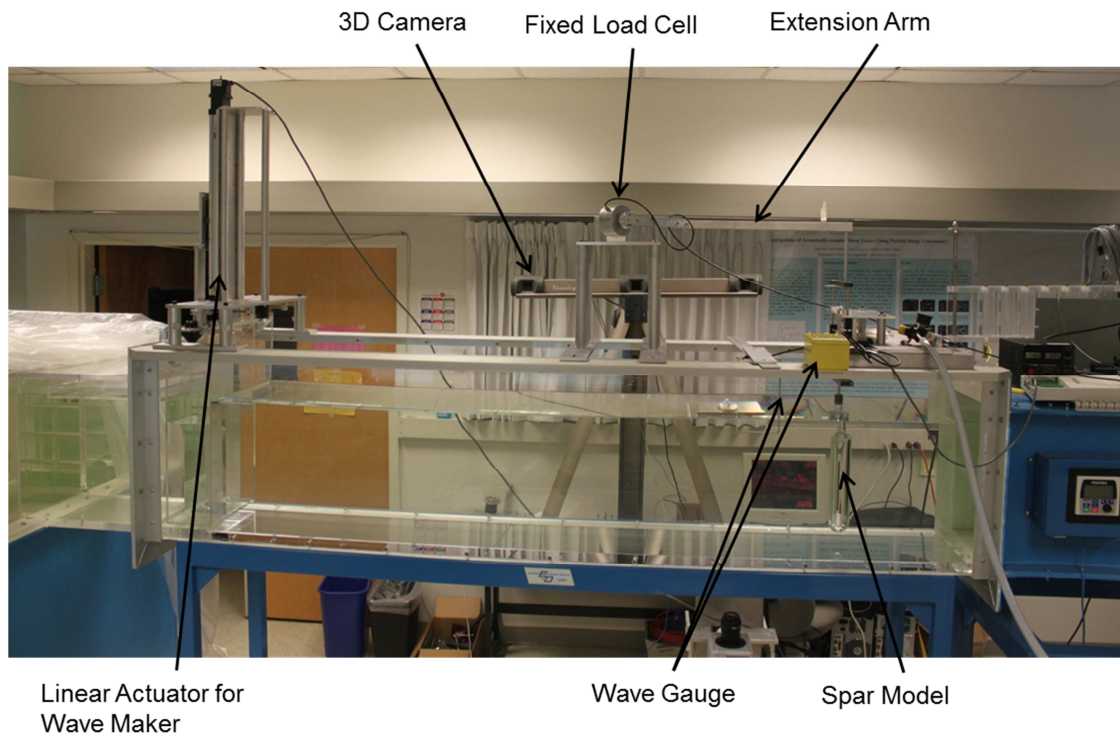


Figure 37 - Wave Field Experimental Setup

The hydrodynamic coefficients resolved utilizing this method are defined in Table 19.

Table 19 – Fixed Body in Wave Experimental Excitation Coefficients

<i>Parameter</i>	<i>Description</i>
\tilde{a}_{cyl}	Added mass of Cylinder in excitation
\tilde{b}_{cyl}	Radiation damping coefficient for Cylinder in excitation
\tilde{a}_{11}	Added mass of Spar-only model in excitation
\tilde{b}_{11}	Radiation damping coefficient for Spar-only model in excitation
\tilde{a}_{12}	Added mass of Spar-float model in excitation
\tilde{b}_{12}	Radiation damping coefficient for Spar-float model in excitation

4.4.4 Reaction Forces of a Free Body in Waves

The freely oscillating body in waves is a redundant test as both the excitation and reaction forces can be identified in the previous tests described in §4.4.2 and §4.4.3. The displacement data from the freely oscillating body in wave tests can be used to confirm either previously determined coefficients, either reaction or excitation. Re-identification of the reaction forces was selected as the forces of the Free-Body in wave experiments.

Equation (4.18) gives the equation of motion for when the body is allowed to freely oscillate in a wave field.

$$\tilde{F}_E + \hat{F}_R = m\ddot{\xi} \quad (4.18)$$

The excitation force, \tilde{F}_E , is a calculated value based on a best fit curve for the added mass and damping coefficients as calculated in §4.4.3 and the actual wave free surface elevation, η , velocity, $\dot{\eta}$, and acceleration, $\ddot{\eta}$, as found within the experimental trial.

Then:

$$(m_i + \hat{a}_{ij})\ddot{\xi} + \hat{b}_{ij}\dot{\xi} + \hat{S}\xi = (m_i + \tilde{a}_{ij})\ddot{\eta} + (\tilde{b}_{ij})\dot{\eta} + \tilde{S}_{ij}\eta \quad (4.19)$$

Determining the hydrodynamic coefficients requires the ability to segregate the points of zero velocity and zero acceleration of the body motion.

The hydrodynamic coefficients that are resolved utilizing this method are defined in Table 20.

Table 20 – Free Oscillation of Body in Wave Experimental Reaction Coefficients

<i>Parameter</i>	<i>Description</i>
\hat{a}_{cyl}	Added mass of Cylinder in reaction
\hat{b}_{cyl}	Radiation damping coefficient for Cylinder in reaction
\hat{a}_{11}	Added mass of Spar-only model in reaction
\hat{b}_{11}	Radiation damping coefficient for Spar-only model in reaction
\hat{a}_{12}	Added mass of Spar-float model in reaction
\hat{b}_{12}	Radiation damping coefficient for Spar-float model in reaction

4.5 Non-dimensional Hydrodynamic Coefficients

The hydrodynamic coefficients for added mass and damping are plotted in a non-dimensionalized format as shown in Equations (4.20) and (4.21). An overbar, ($\bar{\cdot}$), is used to signify a dimensionless value.

$$\bar{a}_{ij} = \frac{a_{ij}}{\rho V} \quad (4.20)$$

$$\bar{b}_{ij} = \frac{b_{ij}}{\rho V \omega} \quad (4.21)$$

The hydrodynamic coefficients are plotted against the non-dimensionalized angular frequency:

$$\bar{\omega} = \frac{\omega^2 a}{g} \quad (4.22)$$

Where, a , is the surface piercing radius.

Chapter 5: Experimental Results

5.1 Overview

Using the experimental apparatus described in Chapter 4 and the experimental procedures described in §4.4, the WEC scale model hydrodynamic coefficients are determined in this Chapter for the range of scaled wave frequencies identified in Table 14 in §3.5.3 . Prior to scale model WEC tests, the abilities of the wave making apparatus to generate steady Airy, or sinusoidal, waves and to eliminate wave reflections into the test area were tested. In the model tests, a series of model geometries are considered:

- 1) Simple Cylinder: The hydrodynamic coefficients of a simple single cylinder were initially determined to validate the procedures for the small scale testing facility. Existing numerical results were used as the basis for the validation.
- 2) Spar-Only Model: To isolate the spar hydrodynamics, the spar component of the WEC scale model was tested alone. The added mass and damping coefficients were determined from four experimental scenarios: a free oscillation in quiescent fluid, a forced oscillation in quiescent fluid, a fixed model in a wave field, and finally the free model in a wave field. The reactive hydrodynamic coefficients are determined from the free and the forced oscillations in quiescent fluid, whereas the excitation hydrodynamic coefficients are determined from the fixed model in the wave field. The free body in the wave field tests involve both excitation and reactive forces, and data from the fixed in wave field tests was used to facilitate another identification exercise for the reactive forces.
- 3) Spar-Float Model: Finally, the concentric float was added to the system in order to determine its influence on the spar dynamics. All four scenarios mentioned in stage (2) above were repeated and the results were compared between the spar-

only and spar-float model configurations, as well as to existing numerical estimates for cylinders of comparable sizes.

The configurations listed above: simple cylinder, spar-only model, and spar-float model are shown in Figure 38. The corresponding results are discussed in the §5.3, §5.4, and §5.5.

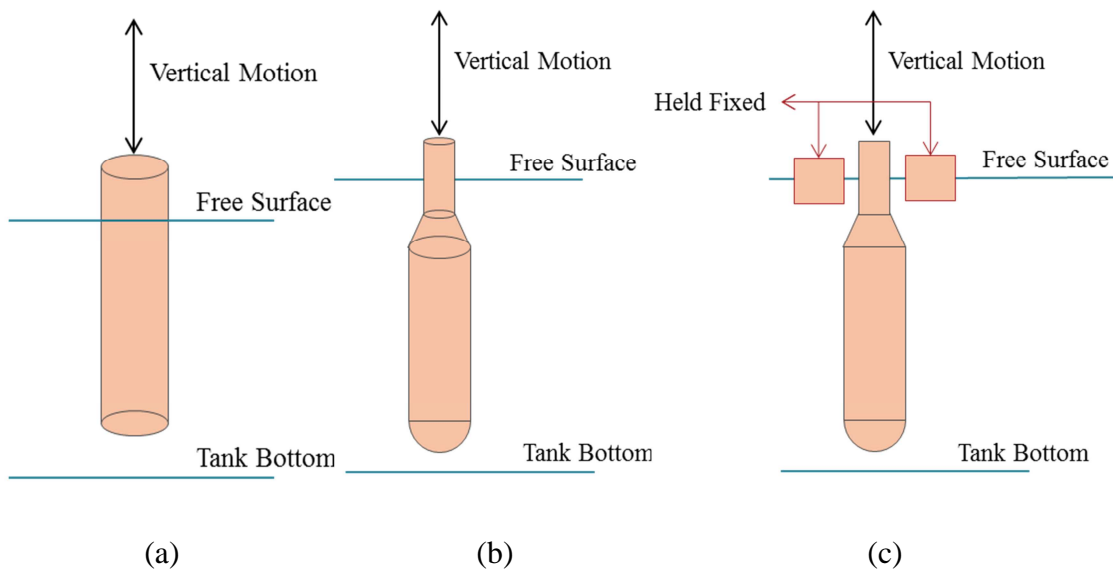


Figure 38 – Small scale model configurations
(a) Simple Cylinder, (b) Spar-only model, (c) Spar-float model configuration in which the float is held fixed.

5.2 Wave Maker Validation

The series of plots in Figure 39 through Figure 41 show sample wave forms generated for the range of cyclic frequencies $1.6 \leq \omega \leq 6.8$ rad/s. Various piston strokes were used across the range of wave frequencies. A repeatable wave height was not always achievable due to the sensitivity of the wave height to the small motions of the piston face. The remainder of wave form profiles can be found in Appendix A. Each test was used to determine the quality of the steady state Airy wave and the impact of wave

reflections within the test section. This series of tests illustrated both temporary and steady perturbations in the desired Airy wave profile at some frequencies.

The waveforms shown in Figure 40 and Figure 41 illustrate some of the defects in the generated waves. When a pure sinusoidal motion is produced with a piston type wave maker, there is always at least one additional free second order wave generated [15, 45]. These can be seen most readily in Figure 40 as a secondary maximum peak developing as time progresses.

The wave form shown in Figure 41 has a levelling of the upper sinusoid peaks. This is due to asymmetry in the relative motion of the piston wave maker and the fluid surface: the volume of water moved to generate the upper peak is less than the volume of water withdrawn to form the trough.

Lastly, there is a prominent low frequency modulation of the wave amplitude that is evident in Figure 40 prior to the 38s point. The exact cause of the low frequency amplitude modulations is unknown; however, these low frequency errors diminish as the tests progress and a steady Airy wave type free surface oscillation does develop for most scenarios. Influence of these wave profile errors on the models were mitigated by manually clipping datasets and retaining only the steady state portions of the test data. For most of the frequencies tested, this is achieved after 40 seconds of wave maker operation. The steady state wave form is not a perfect sinusoid for some frequencies as seen in the higher frequency range close-up plots in Figure 40 and Figure 41, but is suitable for the experiments discussed within this work.

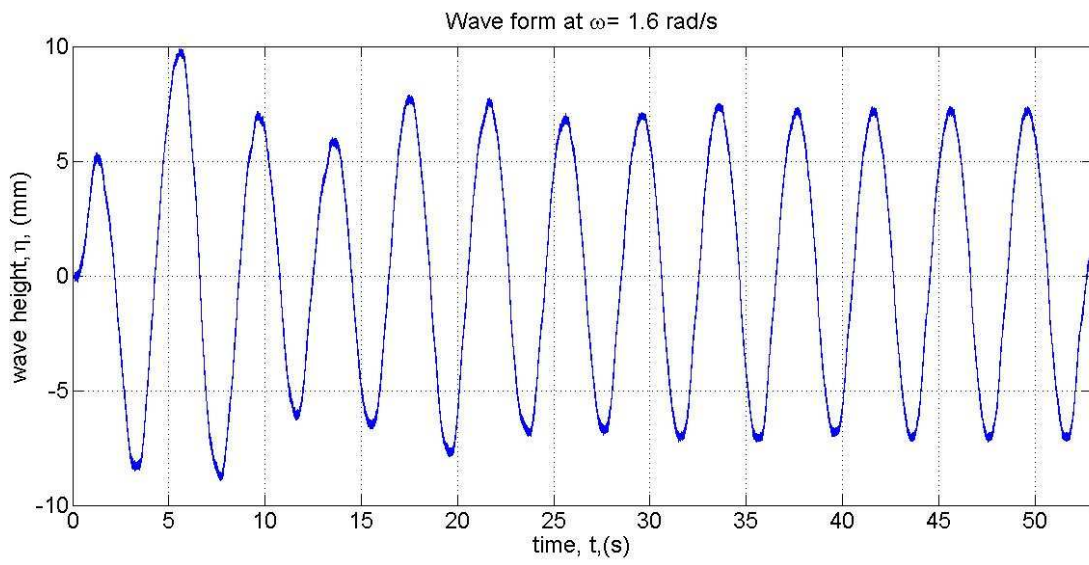


Figure 39 - Wave Form at 1.6rad/s

A relatively pure sinusoidal wave is seen at a time past 40s, the initial ramp up of the wave maker motion can be seen in the upslope of the first peak. The low frequency amplitude modulations are visible to the naked eye up to approximately 35s.

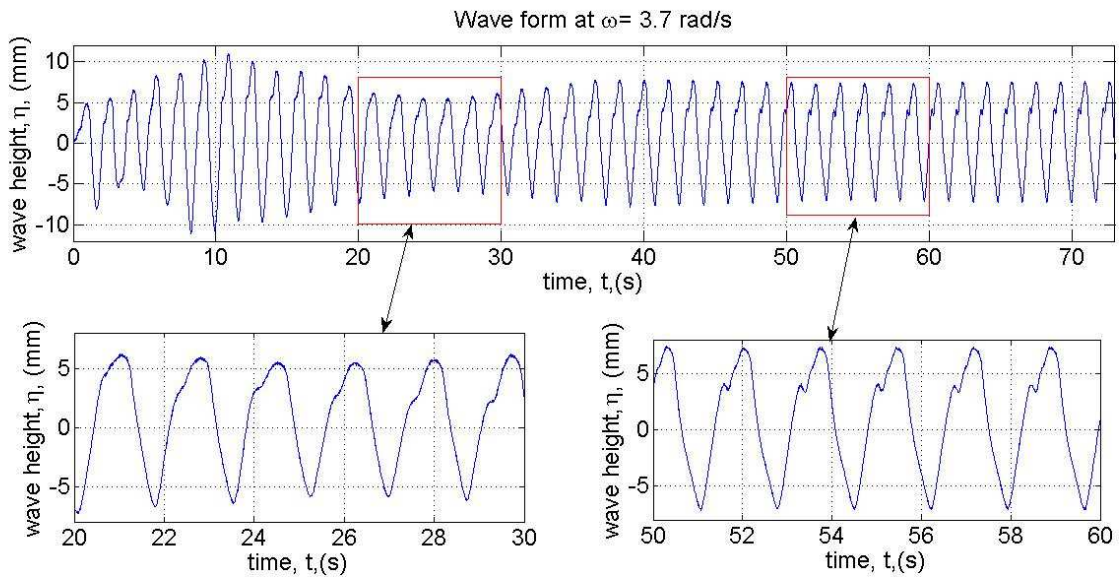


Figure 40 - Wave Form at 3.7 rad/s

The wave form at 3.7rad/s is not purely sinusoidal as time increases: the secondary peak is gaining strength. The low frequency amplitude modulations are most notable at this frequency and are visible to the naked eye until approximately 38s. The bottom two graphs demonstrate the increase in prominence of the secondary peak with time. For this frequency it is assumed that the secondary peak has a lower effect on the hydrodynamic forces than does the amplitude modulation, therefore experimental data is collected after 40s regardless of the secondary peak formation.

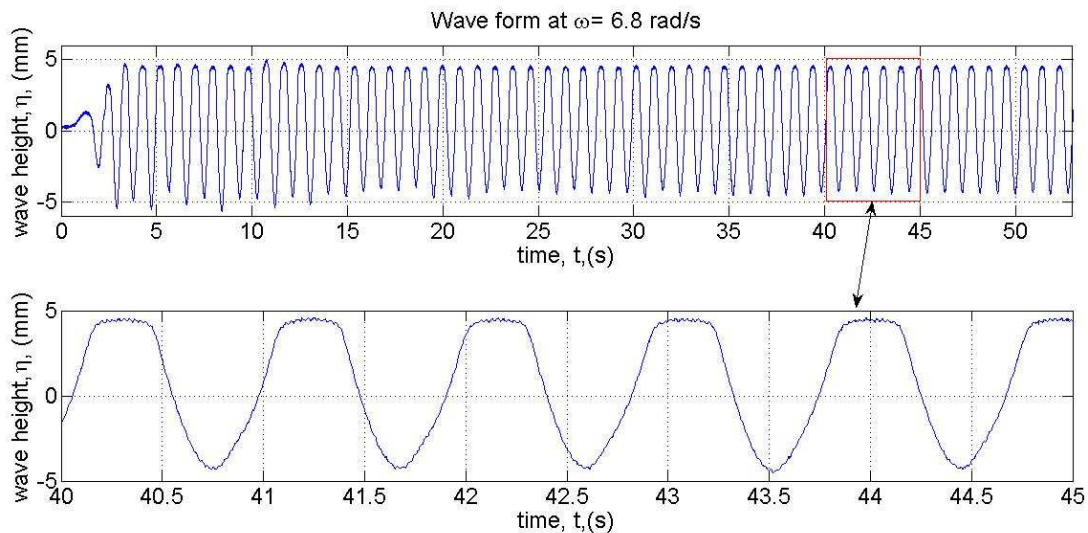


Figure 41 - Wave Form at 6.8 rad/s

At this frequency, the low frequency amplitude modulation is not as obvious to the naked eye, but can still be seen on the lower end of the surface elevation, until approximately 35s. When viewing the waveform over a smaller time scale, (5s) as in the lower graph, the asymmetric shape of the surface wave is more pronounced. In this case the upper surface elevation of the sinusoid form is cropped, or leveled off.

5.3 Simple Cylinder Model Tests

The simple cylinder was used to validate the characterization procedures in the test facility. The cylinder had a radius of 38.1mm (1.5in) and a draft of 22cm. This size of cylinder was found to produce sufficient buoyancy forces to overcome the inertia of the linear guide system: the cylinder is designed so that when the linear guide components are attached to it, it sits at a desired height in the fluid. The cylinder was made of Lexan (plexi glass) tubing, with epoxied end caps.

The hydrodynamic coefficients as defined in Table 21 were identified in the four experimental methods detailed in §4.4

Table 21 - Experimentally determined hydrodynamic coefficients for a simple cylinder

<i>Experimentally Determined Coefficients</i>	<i>Experimental Method</i>	<i>Description</i>	<i>Frequency Tested</i>
\hat{a}_{cyl}	Free in Quiescent	Reaction Added Mass for Simple Cylinder configuration	Natural Frequency
\hat{b}_{cyl}	Free in Quiescent	Reaction Damping Coefficient for Simple Cylinder configuration	Natural Frequency
\hat{a}_{cyl}	Forced in Quiescent	Reaction Added Mass for Simple Cylinder configuration	1.6-4.3 rad/s
\hat{b}_{cyl}	Forced in Quiescent	Reaction Damping Coefficient for Simple Cylinder configuration	1.6-4.3 rad/s
\tilde{a}_{cyl}	Fixed in Waves	Excitation Added Mass for Simple Cylinder configuration	1.6-6.8 rad/s
\tilde{b}_{cyl}	Fixed in Waves	Excitation Damping Coefficient for Simple Cylinder configuration	1.6-6.8 rad/s
\hat{a}_{cyl}	Free in Waves	Reaction Added Mass for Simple Cylinder configuration	1.6-6.8 rad/s
\hat{b}_{cyl}	Free in Waves	Reaction Damping Coefficient for Simple Cylinder configuration	1.6-6.8 rad/s

5.3.1 Free Oscillations in Quiescent Fluid

The motion occurring after an initial displacement of the simple cylinder in quiescent fluid is shown in Figure 42. The hydrodynamic coefficients \hat{a}_{cyl} and \hat{b}_{cyl} were determined using the methodology discussed in §4.4.1.

Each data point in Figure 43 represents one peak to peak calculation of the coefficients. It was noted that as oscillations progressed, the frequency of oscillation was found to increase, and this increase in frequency resulted in a decrease in the estimated added mass and damping coefficients. In Figure 43 the added mass and damping coefficients are plotted against the results of the numerical model developed by Calisal & Sabuncu in [25]. The reference model was selected as the basis of the validation as it has been shown to be reasonably accurate in comparison to experiments as presented in [25].

The increase in oscillation frequency is attributed to the decrease in oscillation displacement amplitude. Visible in Figure 43 is the decrease in added mass and damping coefficients with increasing frequency. As oscillation amplitude decreases, so does the velocity. Therefore in the larger oscillations there may be an amplitude dependant damping term, form drag, induced by flow separation.

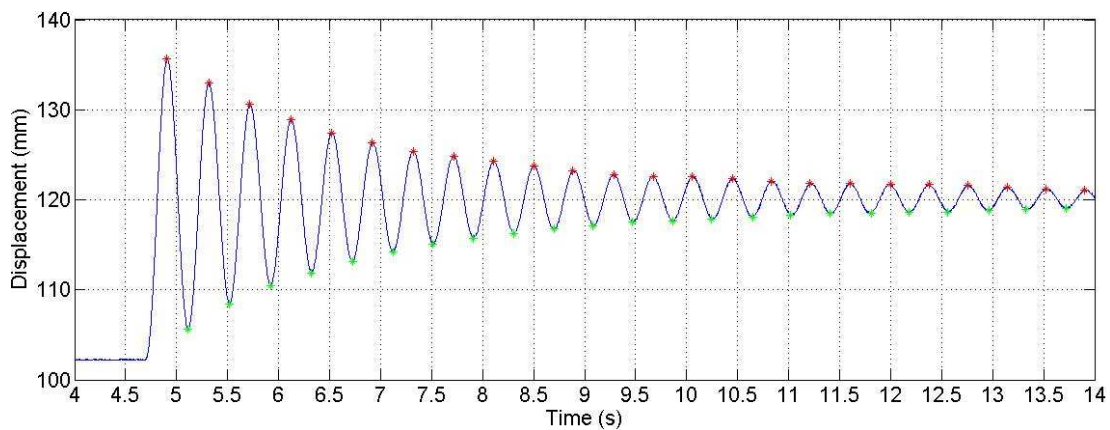


Figure 42 - Naturally Damped, Cylinder in Quiescent Fluid

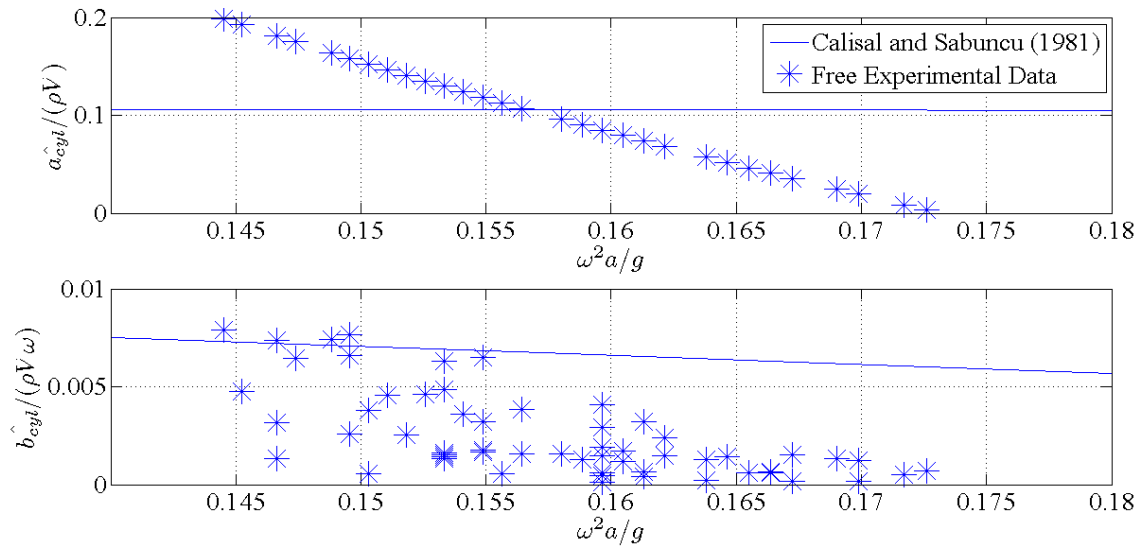


Figure 43 - Hydrodynamic Coefficients of Free cylinder in Quiescent Fluid.

5.3.2 Forced Oscillations in Quiescent Fluid

The cylinder configuration was forced to oscillate utilizing the forcing mechanism discussed in §4.4.2 over a range of frequencies. The hydrodynamic coefficients \hat{a}_{cyl} and \hat{b}_{cyl} as defined in Table 21, were then calculated utilizing the methodology discussed in §4.4.2 and the results of the forced cylinder trial are plotted against the numerical model from Calisal & Sabuncu in [25] as shown in Figure 44. Each plotted experimental data point is the average of a single test's series of calculated values.

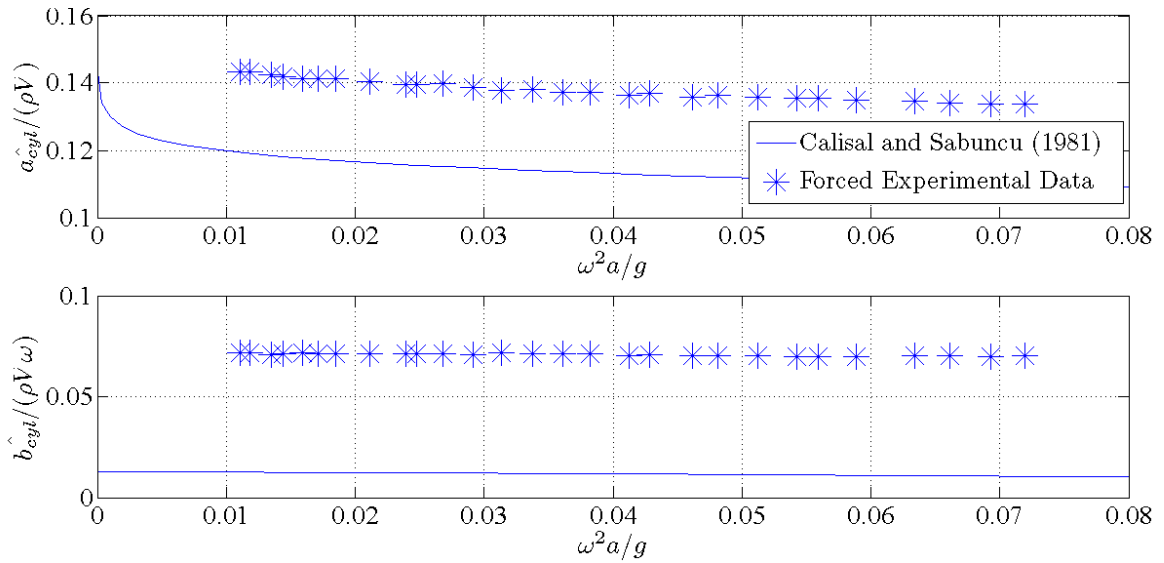


Figure 44 - Reaction Coefficients of Forced Cylinder in Quiescent Fluid

The cylinder configuration is used as a confirmation that the experimental setup and methodology is valid and can be used for the spar-only model and spar-float model configurations. The results shown in Figure 44 show that the experimentally determined reaction coefficients follow the same trends as the numerical predictions made by Calisal and Sabuncu in [25]. While the match up of experimental and numerical results in Figure 44 is not ideal, it must be noted that the comparison of these numerical results in [25] to other experimental data gathered with cylindrical buoy geometry showed a similar level of mismatch.

5.3.3 Fixed Model in Wave Field

The setup used for the fixed body in wave field trials includes the wave maker, the fixed load cell, wave gauge and the linear guide arrangement for the body. This arrangement can be seen in Figure 37. The experimental process and hydrodynamic coefficient calculation methodology are described in §4.4.3. The results of the fixed cylinder trial, estimates of the hydrodynamic coefficients \tilde{a}_{cyl} and \tilde{b}_{cyl} are plotted against the numerical model predictions from Calisal & Sabuncu in [25] as shown in Figure 45.

The added mass coefficients appear to increase with increasing frequency, while the damping coefficients appear to decrease with increasing frequency. The data points with a wave frequency higher than 3.5rad/s as shown on the right side of the dashed line are not considered to be reliable as the recorded force data was of a magnitude corresponding to the force signal noise. The poor signal to noise ratio made it extremely difficult to synchronize the wave probe and load cell data sets.

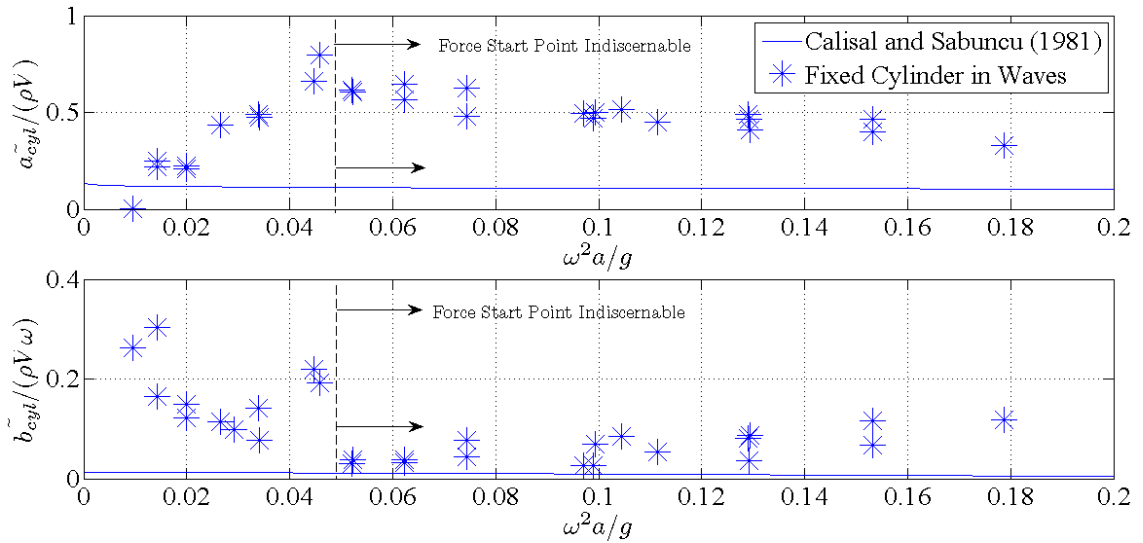


Figure 45 - Excitation Coefficients of Fixed Cylinder in Wave Field

5.3.4 Free Model in Wave Field

The final method of determining the hydrodynamic coefficients required two operations per configuration: a free oscillation of the body in the wave field, in order to determine the displacement, velocity and acceleration induced by the waves, and a fixed body in the wave field trial in order to measure the excitation forces to the body and develop estimated values for the excitation coefficients as described in §5.3.3. The best fit excitation coefficients were determined from the regression analysis toolbox in Matlab using a cubic solution. The excitation added mass and damping equations extracted were

$$\tilde{a}_{cyl} = (914.86\bar{\omega}^3 - 297.44\bar{\omega}^2 + 26.925\bar{\omega} - 0.0879) \times \rho V \quad (5.1)$$

$$\tilde{b}_{cyl} = (-132.37\bar{\omega}^3 + 54.834\bar{\omega}^2 - 6.5591\bar{\omega} + 0.28874) \times \rho V \omega \quad (5.2)$$

The two sets of data were then combined in order to re-determine the reaction hydrodynamic coefficients \hat{a}_{cyl} and \hat{b}_{cyl} . The calculation methodology is as described in §4.4.4. To facilitate the combination of datasets, the same wave regime is utilized for the fixed body and free body in wave experiments.

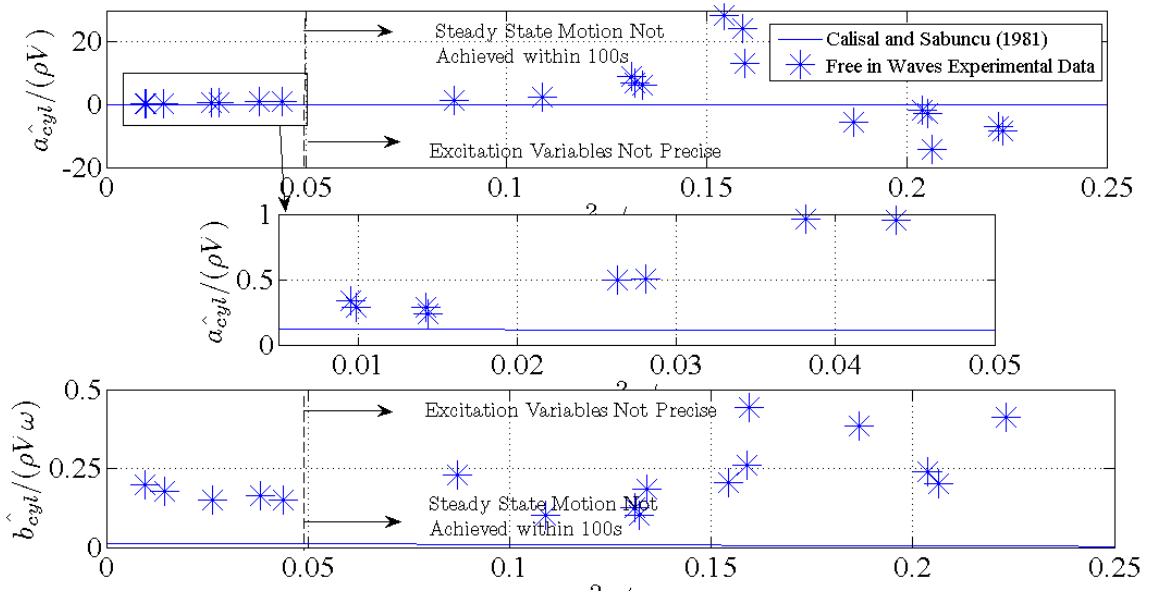


Figure 46 - Reaction Coefficients of Free Simple Cylinder in Wave Field

For the lower frequency data points, the added mass is increasing with increasing frequency, while the damping coefficient is decreasing with increasing frequency. The higher frequency data points indicated in Figure 46 are not considered to be valid as both the forced data sets and free data sets were found to have poor signal to noise ratio at the higher frequency range designated by the dashed line. As discussed in §5.3.3, the force measurements start point was not able to be accurately determined, while in the free experiment, the body oscillations did not achieve steady state motion within 100s of wave tests. Interesting to note is the exceedingly high amplitude of body oscillation with respect to the wave amplitude: over the range of tested frequencies the maximum ratio of oscillation amplitude to wave amplitude was 8:1 at 6.3rad/s.

Although the range of attempted wave frequencies was consistent for all of the model geometries tested, it was found that model specific constraints on the frequency range had to be applied. For example, the body would hit the bottom of the tank or not oscillate at all for some frequencies in the in the attempted range. Or, the linear guides would stick due to excessive horizontal loads from the waves. The air bushings ideal operating pressure was designed to be 60-100psi, while the actual available pressure to the system was between 40-60psi. When such situations occurred, the experiments were stopped, and reattempted. If the scenario repeated, experiments were halted and no data was collected at that frequency and wave height. Some of the tests with common frequency had various wave heights as repeatable wave heights could not be achieved without a feedback loop between the wave gauge and the wave maker. Such closed loop control could not be implemented within the project scope. Wave heights ranged from 2.6mm to 19.4mm in the fixed experiments, and from 2.4mm to 6.8mm in the free experiments.

5.4 Spar-Only Model Configuration

The hydrodynamic coefficients as defined in Table 22 were identified in the four experimental methods detailed in §4.4

Table 22 - Experimentally determined hydrodynamic coefficients for a spar-only model

<i>Experimentally Determined Coefficients</i>	<i>Experimental Method</i>	<i>Description</i>	<i>Frequency Tested</i>
\hat{a}_{11}	Free in Quiescent	Reaction Added Mass for Spar-Only configuration	Natural Frequency
\hat{b}_{11}	Free in Quiescent	Reaction Damping Coefficient for Spar-Only configuration	Natural Frequency
\hat{a}_{11}	Forced in Quiescent	Reaction Added Mass for Spar-Only configuration	2.0-7.4 rad/s
\hat{b}_{11}	Forced in Quiescent	Reaction Damping Coefficient for Spar-Only configuration	2.0-7.4 rad/s
\tilde{a}_{11}	Fixed in Waves	Excitation Added Mass for Spar-Only configuration	1.5-2.6 rad/s
\tilde{b}_{11}	Fixed in Waves	Excitation Damping Coefficient for Spar-Only configuration	1.5-2.6 rad/s
\hat{a}_{11}	Free in Waves	Reaction Added Mass for Spar-Only configuration	1.5-2.6 rad/s
\hat{b}_{11}	Free in Waves	Reaction Damping Coefficient for Spar-Only configuration	1.5-2.6 rad/s

5.4.1 Free Oscillations in Quiescent Fluid

The experimental process for a free body with initial displacement in quiescent fluid is repeated for the spar-only model configuration as shown in Figure 38(b). The hydrodynamic coefficients \hat{a}_{11} and \hat{b}_{11} , were calculated using the process detailed in §4.4.1. The hydrodynamic coefficients are plotted in Figure 47 against the numerical model developed by Calisal & Sabuncu in [25] for two different cylinders matching the cross sectional diameters of the surface piercing portion of the spar, and the cross sectional diameters of the lower submerged portion of the spar. .

The discrepancy observed between the numerical model and the experimental results can be explained by the more complex spar geometry. The simple cylinders considered in the numerical work have a bottom horizontal sharp edged surface that generates hydrodynamic effects distinct from those associated with the rounded bottom surface of

the spar and the spar's taper section. The comparison of the numerical and experimental results is provided to demonstrate the need for geometry specific experimental data: the existing numerical models for simple cylinders do not suffice.

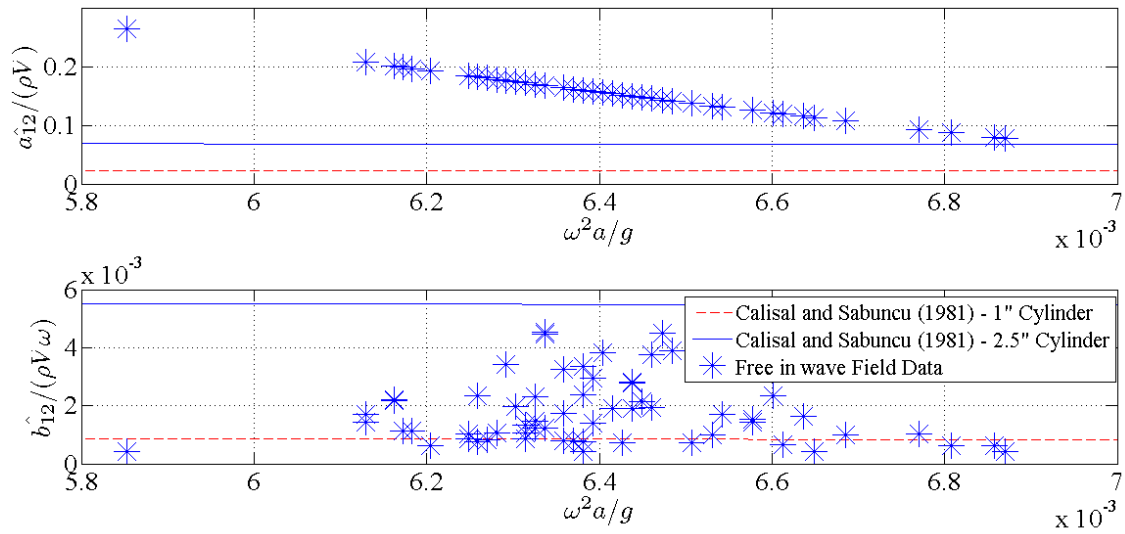


Figure 47 - Hydrodynamic Coefficients of Free Spar-Only model in Quiescent Fluid

The spar configuration results indicate that the geometry of the spar generates enough discrepancy between the theoretical models of a simple cylinder of either size, with a significantly higher added mass. The damping coefficient values are a compromise between the 1" diameter cylinder and the 2.5" diameter cylinder.

Similarly with the cylinder trials, the frequency was found to increase with a decrease in oscillation amplitude, leading to the conclusion that form drag may be present in the higher amplitude oscillations.

5.4.2 Forced Oscillations in Quiescent Fluid

The spar-only model configuration was forced to oscillate utilizing the forcing mechanism discussed in §4.2 over a range of frequencies. The hydrodynamic

coefficients \hat{a}_{11} and \hat{b}_{11} , were then calculated utilizing the methodology discussed in §4.4.2 and the results of the forced spar trial are plotted against the numerical model for the two cylinders sizes comparable to the two main cross sectional diameters of the spar from Calisal & Sabuncu in [25] as shown in Figure 48.

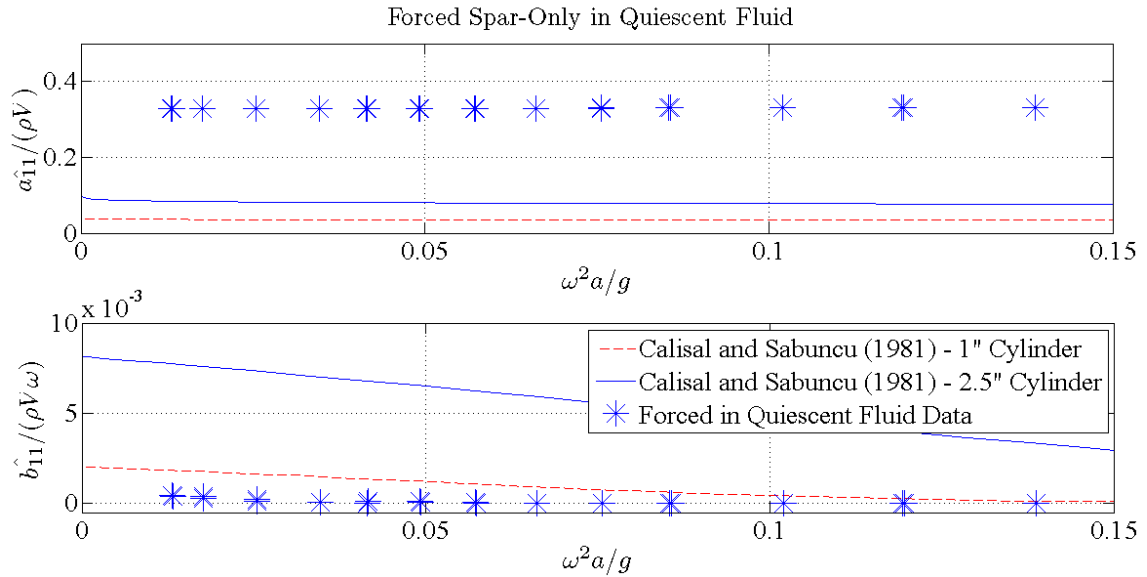


Figure 48 - Reaction Coefficients of Forced Spar-Only model in Quiescent Fluid

Although not obvious in Figure 48, both the added mass and damping coefficients were found to have parabolic like trends when the scale of the plot is reduced as shown in Figure 49 and Figure 50. The added mass increases with increasing frequency with an asymptote that nears a non-dimensional value of 0.4045, while the damping decreases with increasing frequency, with an asymptote of 0.

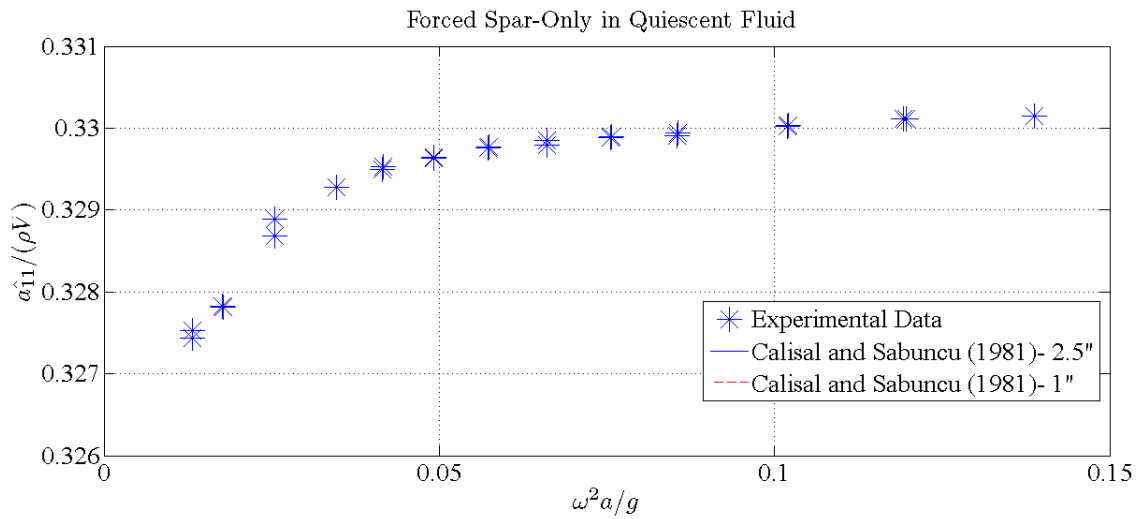


Figure 49 - Forced Spar-Only in Quiescent Fluid: Added Mass

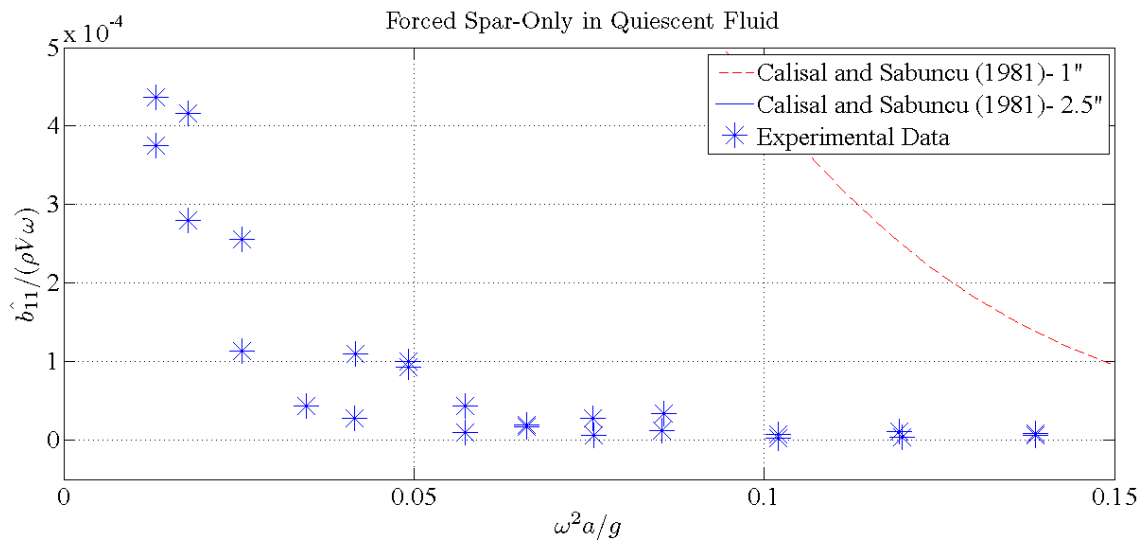


Figure 50 - Forced Spar-Only in Quiescent Fluid: Damping Coefficient

5.4.3 Fixed Model in Wave Field

The Spar-only model configuration was fixed in the wave field and the experimental process and hydrodynamic coefficient calculation methodology of §4.4.3 was followed.

The excitation hydrodynamic coefficients \tilde{a}_{11} and \tilde{b}_{11} , were then determined and plotted

in Figure 51 against the numerical model output for the 1" and 2.5" diameter cylinders from Calisal & Sabuncu in [25].

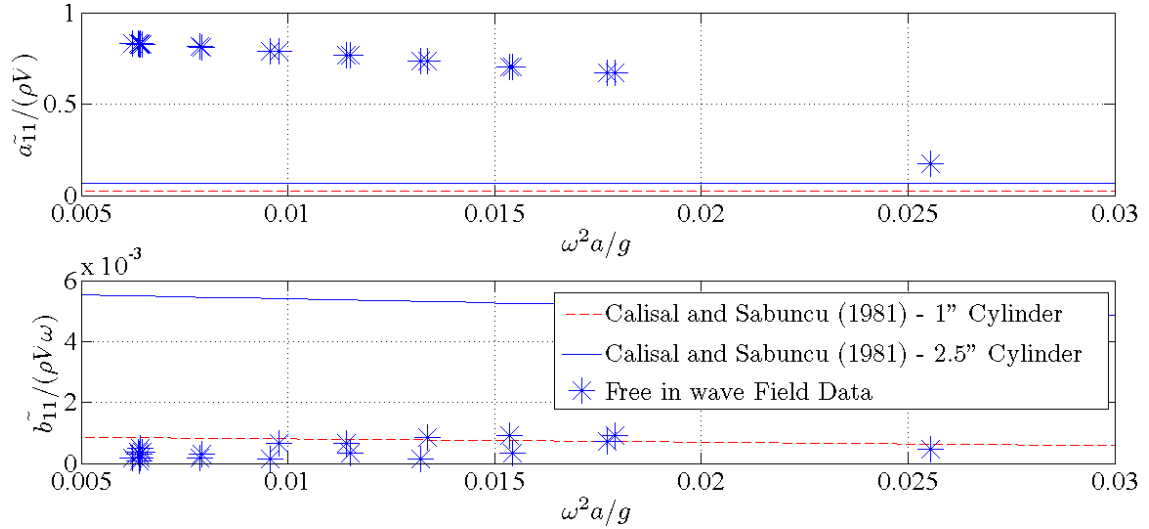


Figure 51 - Excitation Coefficients of Fixed Spar-only model in Wave Field

The added mass has a decreasing trend with increasing frequency, whereas the damping coefficient appears to have an increasing trend with increasing frequency. No data points with a wave frequency higher than 3.2rad/s are shown as the signal to noise ratio of the recorded force data was too poor to permit reliable data analysis.

5.4.4 Free Model in Wave Field

The Spar-only model configuration was allowed to freely oscillate in the wave field and the experimental process and hydrodynamic coefficient calculation methodology described in §4.4.4 was followed. The excitation coefficients were determined from the basic fitting tool in Matlab using a cubic solution from the fixed model experimental results. The excitation added mass and damping equations extracted were

$$\tilde{a}_{11} = (-1.5621 \times 10^5 \bar{\omega}^3 + 5291.3 \bar{\omega}^2 - 69.292 \bar{\omega} + 1.0981) \times \rho V \quad (5.3)$$

$$\tilde{b}_{11} = (-403.01 \bar{\omega}^3 + 15.649 \bar{\omega}^2 - 0.14428 \bar{\omega} + 0.00064872) \times \rho V \omega \quad (5.4)$$

The hydrodynamic coefficients \hat{a}_{11} and \hat{b}_{11} as defined in Table 22, are determined and plotted in Figure 52 against the numerical model for the two cylinders sizes comparable to the two main cross sectional diameters of the spar from Calisal & Sabuncu in [25].

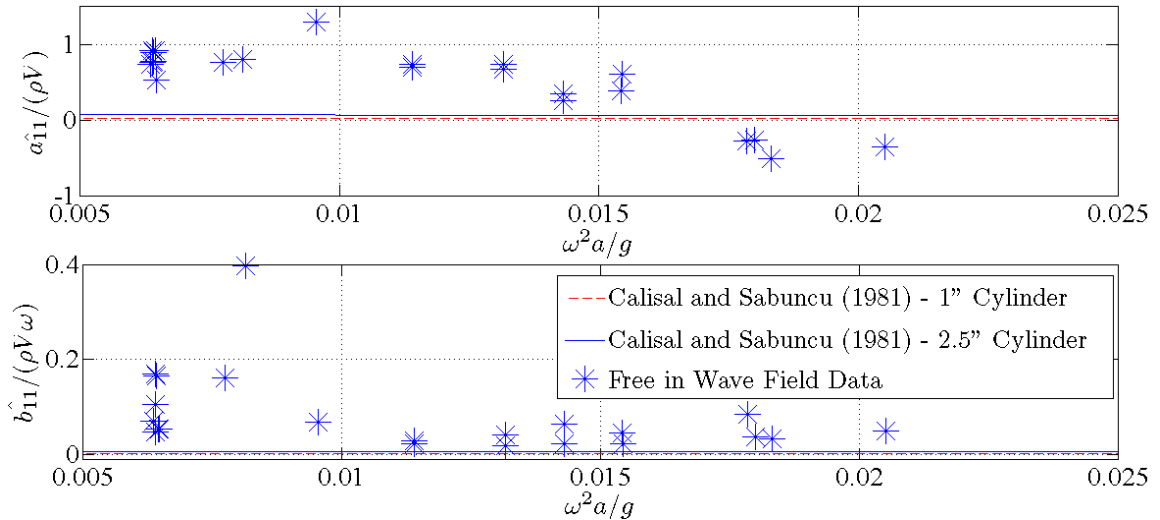


Figure 52 - Reaction Coefficients of Free Spar-Only model in Wave Field

The spar-only model configuration results indicate that the geometry of the spar generates noticeable discrepancies from the theoretical models of a simple cylinder of either the 1" or 2.5" diameters.

The free body in wave experiments with the spar geometry exhibited some of the same detrimental features as found in the cylinder experiments. Visible in Figure 53, steady state motion was not always achieved in the duration of the test. For waves of frequencies greater than 2.4rad/s, the horizontal loading was believed to be affecting the system hydrodynamics. The evidence for this effect came at the end of the trials when the waves stopped. The model amplitude of oscillation increased as the horizontal load decreased with the end of the generated waves, as observed on the right of the vertical line displayed at 68s in Figure 53. The excessive horizontal loading was not able to be compensated for by the air bushings, and bearing friction is added to the system.

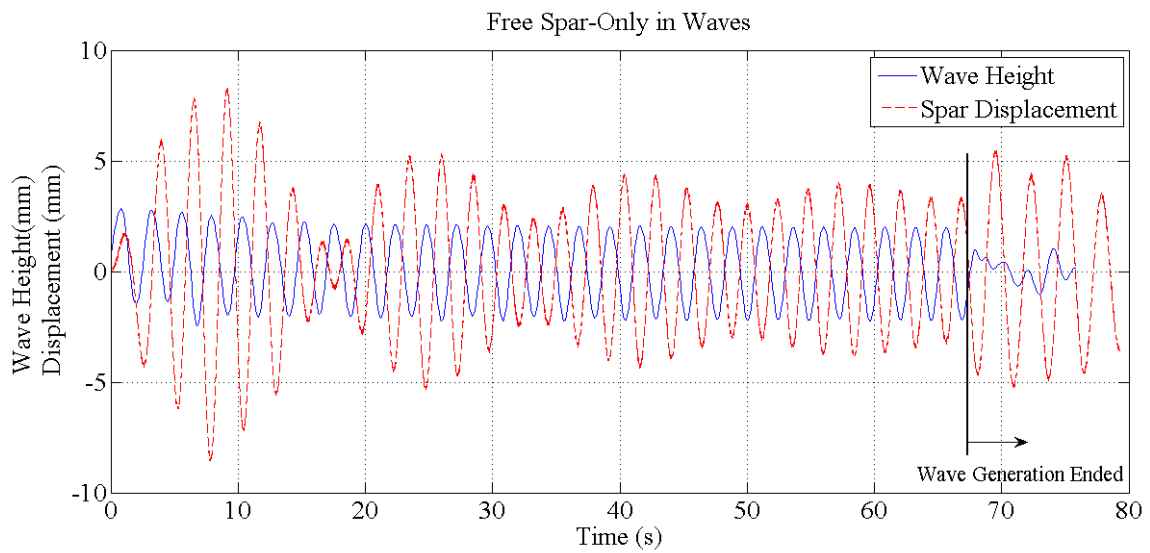


Figure 53 - Sample of Experimental Errors: Spar-only model at 2.6rad/s

Notably, the damping coefficient is affected by the wave amplitude, as was originally determined in the free body in quiescent trials shown in Figure 47. The spar oscillated with a magnified body oscillation with respect to the wave amplitude.

5.5 Spar-Float Model Configuration

The hydrodynamic coefficients listed in Table 23 were identified using the four experimental methods detailed in §4.4. The spar-float model is shown in Figure 54.

Table 23 - Experimentally determined hydrodynamic coefficients for a spar-float model

<i>Experimentally Determined Coefficients</i>	<i>Experimental Method</i>	<i>Description</i>	<i>Frequency Tested</i>
\hat{a}_{12}	Free in Quiescent	Reaction Added Mass for Spar-Float configuration	Natural Frequency
\hat{b}_{12}	Free in Quiescent	Reaction Damping Coefficient for Spar-Float configuration	Natural Frequency
\hat{a}_{12}	Forced in Quiescent	Reaction Added Mass for Spar-Float configuration	2.3-5.6 rad/s
\hat{b}_{12}	Forced in Quiescent	Reaction Damping Coefficient for Spar-Float configuration	2.3-5.6 rad/s
\tilde{a}_{12}	Fixed in Waves	Excitation Added Mass for Spar-Float configuration	1.3-2.7 rad/s
\tilde{b}_{12}	Fixed in Waves	Excitation Damping Coefficient for Spar-Float configuration	1.3-2.7 rad/s
\hat{a}_{12}	Free in Waves	Reaction Added Mass for Spar-Float configuration	1.3-2.7 rad/s
\hat{b}_{12}	Free in Waves	Reaction Damping Coefficient for Spar-Float configuration	1.3-2.7 rad/s

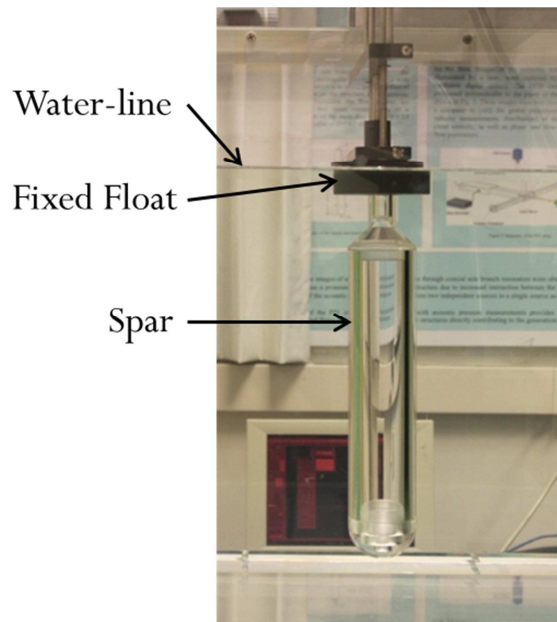


Figure 54 - Spar and Float combination

5.5.1 Free Oscillations in Quiescent Fluid

The experimental process for a free body with initial displacement in quiescent fluid was repeated for the spar again, but with the float present in a fixed position. The model configuration is shown in Figure 38(c). The lumped hydrodynamic coefficients \hat{a}_{12} and \hat{b}_{12} were calculated from the motion data using the process detailed in §4.4.1. The hydrodynamic coefficients are plotted in Figure 55 against the numerical model from Calisal and Sabuncu in [25] for the two main cross sectional diameters of the spar.

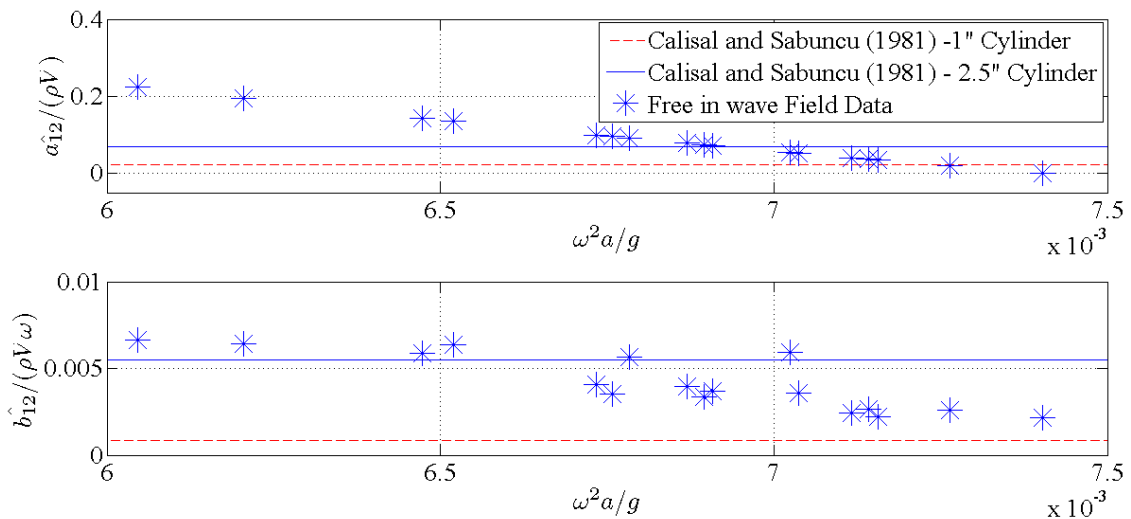


Figure 55 – Hydrodynamic Coefficients for Free Spar-Float model in Quiescent Fluid

Both the added mass and damping coefficients demonstrated a linear attenuation as frequency increase. The spar-only and spar-float test results are compared in §5.6.1.

5.5.2 Forced Oscillations in Quiescent Fluid

The spar in the spar-float model configuration, shown in Figure 38 (c), was forced to oscillate over a range of frequencies. The hydrodynamic coefficients \hat{a}_{12} and \hat{b}_{12} were calculated utilizing the methodology discussed in §4.4.2. The results of the forced spar-

float model trial are plotted in Figure 56 against the numerical model predictions for the 1" and 2.5" diameter cylinders from Calisal & Sabuncu in [25]. In addition, close-up views of the added mass and damping coefficients are provided in Figure 57 and Figure 58 respectively.

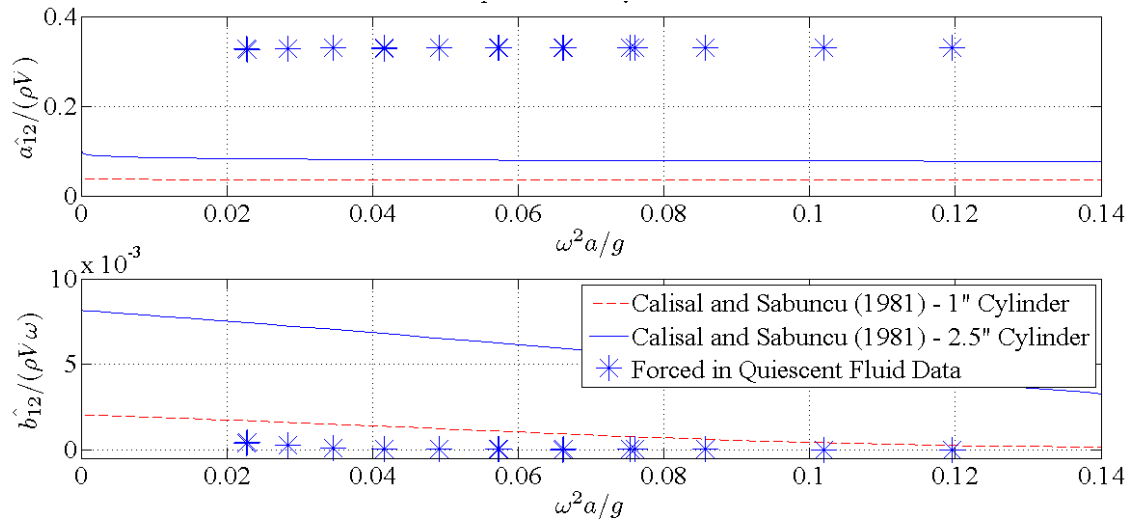


Figure 56 - Reaction Coefficients for Forced Spar-Float model in Quiescent Fluid

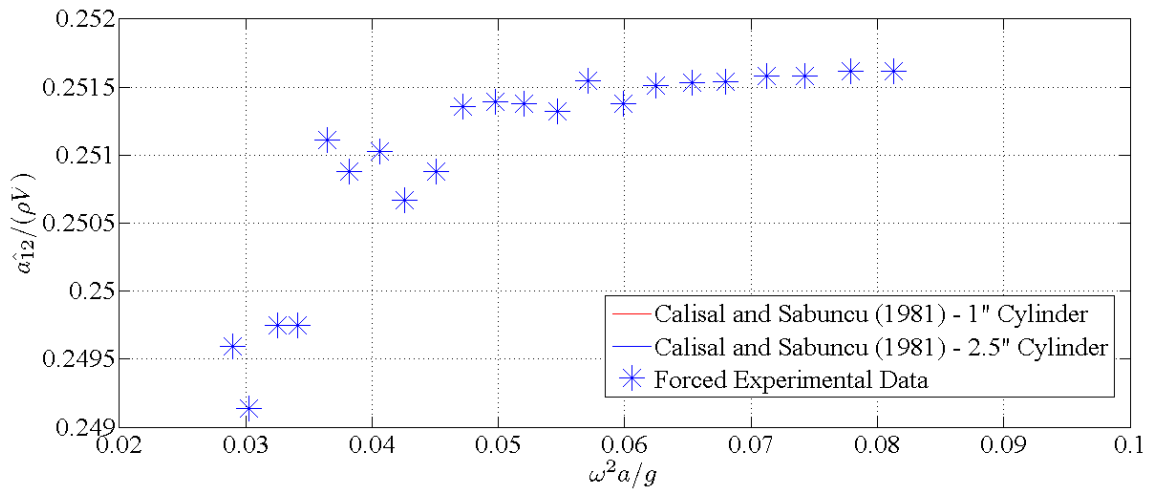


Figure 57 - Forced Spar-Float in Quiescent Fluid: Added Mass

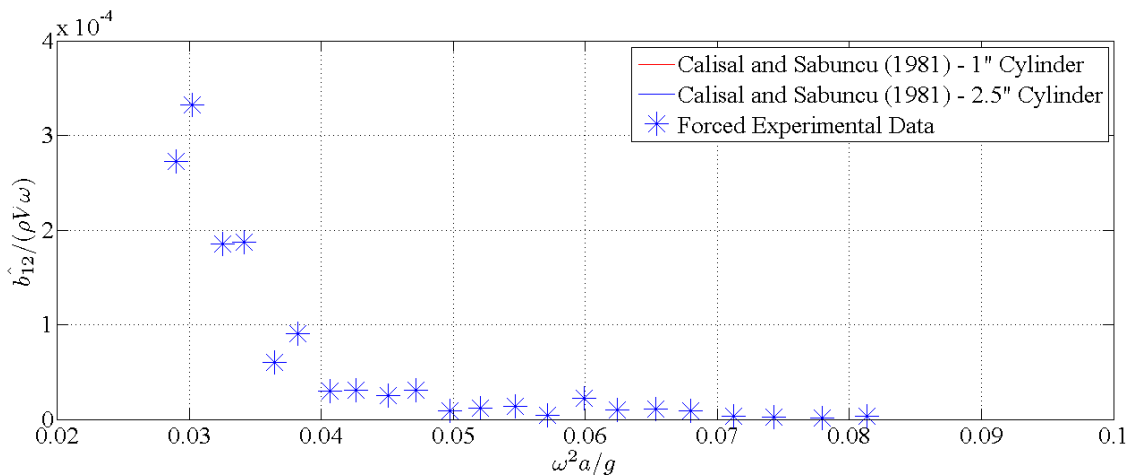


Figure 58 - Forced Spar-Float in Quiescent Fluid: Damping Coefficient

The spar-float model configuration results indicate that the geometry of the spar generates enough discrepancy between the theoretical models of a simple cylinder of either size. The added mass appears to have a parabolic like curve which increases with frequency, with a non-dimensional added mass asymptote nearing 0.3302. The damping coefficient appears to follow a parabolic like curve which decreases with frequency although at a very low value. The spar-only and spar-float test results are compared in §5.6.2.

5.5.3 Fixed Model in Wave Field

The Spar-float model configuration was fixed in the wave field and the experimental process and hydrodynamic coefficient calculation methodology of §4.4.3 was followed. The lumped hydrodynamic coefficients \tilde{a}_{12} and \tilde{b}_{12} were determined and plotted in Figure 59 against the numerical model predictions for the 1" and 2.5" diameter of Calisal & Sabuncu in [25]. In addition, close-up views of the added mass and damping coefficients are provided in Figure 60 and Figure 61 respectively.

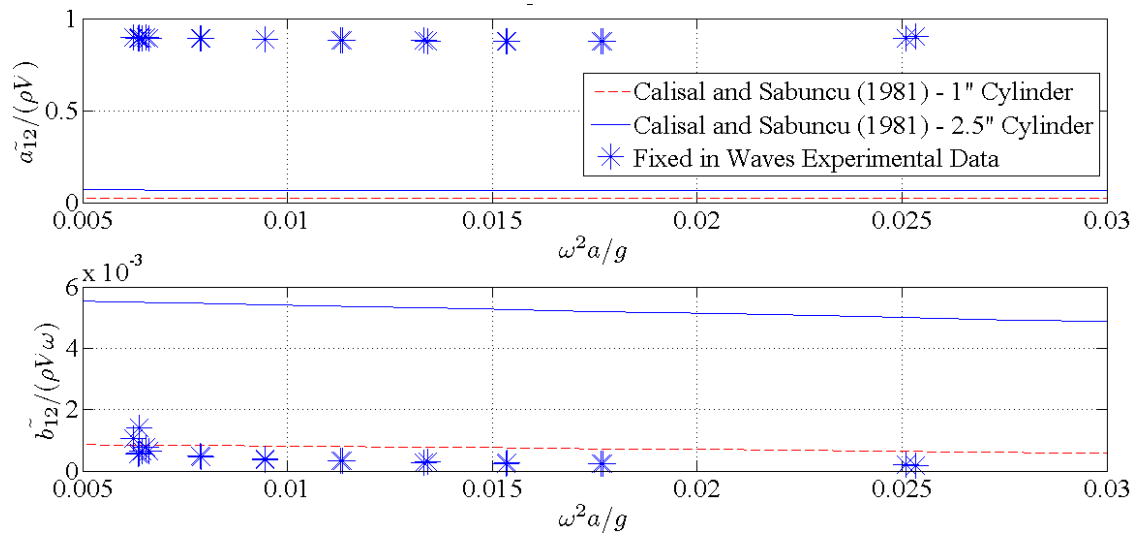


Figure 59 - Excitation Coefficients of Fixed Spar-Float model in Wave Field

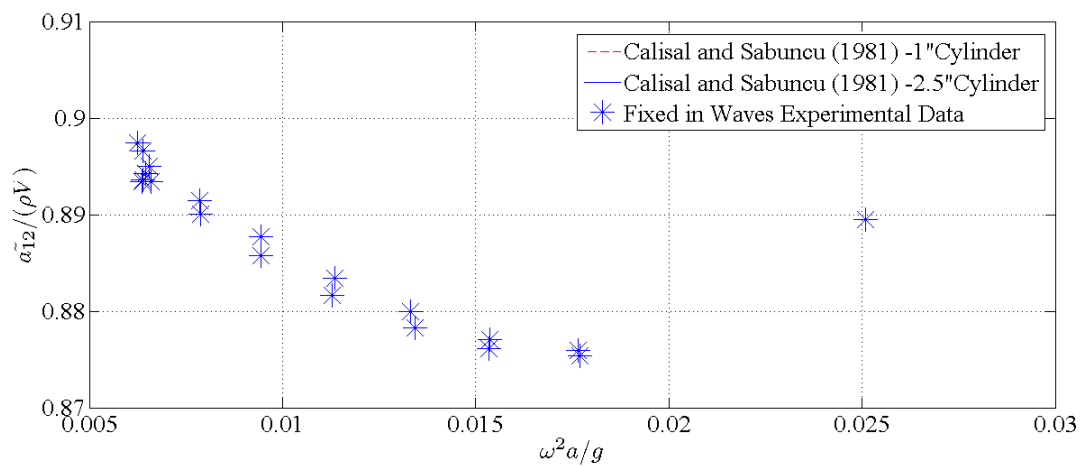


Figure 60 - Fixed Spar-float model in Waves: Added mass

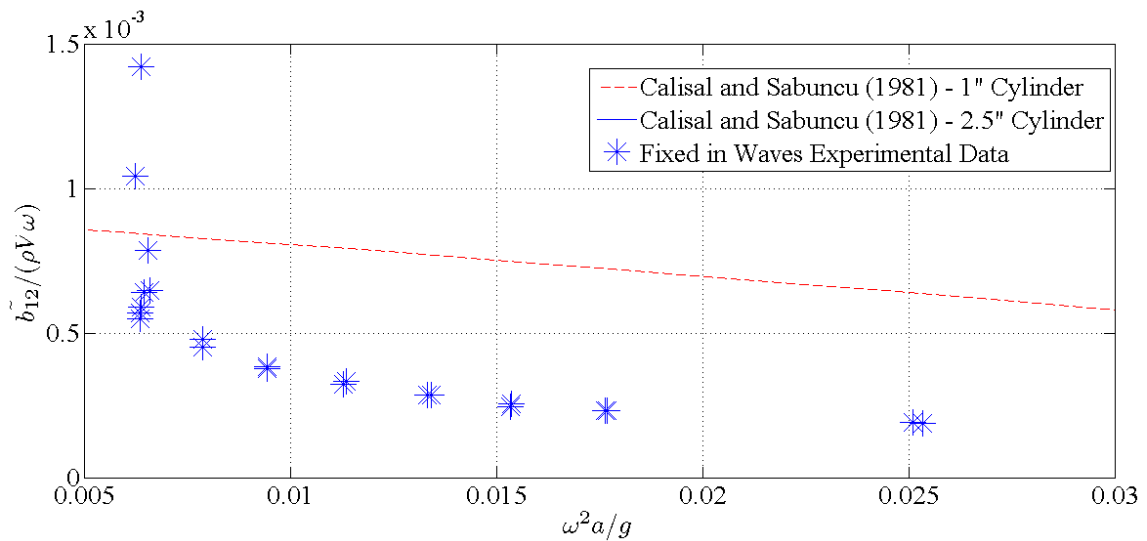


Figure 61 - Fixed Spar-float model in Waves: damping coefficient

The added mass and damping coefficients have a decreasing trend as frequency increases. No data points with a wave frequency higher than 3.2rad/s are shown as the signal to noise ratio of the recorded force data was too poor to permit reliable data analysis. Multiple wave heights at the same frequency were trialed, as can be seen in these results with the left most cluster of data points. This scenario shows that there is an amplitude dependant damping term. The spar-only and spar-float test results are compared in §5.6.3.

5.5.4 Free Model in Wave Field

The spar in the spar-float model configuration was then allowed to freely oscillate in the wave field. Using the experimental process and hydrodynamic coefficient calculation methodology described in §4.4.4, the reaction coefficients were re-identified. The excitation coefficients applied in that identification were determined from the basic fitting tool in Matlab using a 4th degree polynomial and a cubic solution from the fixed model experimental results. The non-dimensional excitation added mass and damping equations used were

$$\tilde{a}_{12} = (1.1897 \times 10^6 \bar{\omega}^4 - 62189 \bar{\omega}^3 + 1274.1 \bar{\omega}^2 - 13.557 \bar{\omega} + 0.94371) \times \rho V \quad (5.5)$$

$$\tilde{b}_{12} = (-123.75\bar{\omega}^3 + 7.2827\bar{\omega}^2 - 0.14596\bar{\omega} + 0.0012229) \times \rho V \omega \quad (5.6)$$

The lumped hydrodynamic coefficients \tilde{a}_{12} and \tilde{b}_{12} are determined and plotted against the numerical model for the two cylinders sizes comparable to the two main cross sectional areas of the spar from Calisal & Sabuncu in [25] as shown in Figure 62 with a close-up view of the added mass coefficient in Figure 63 .

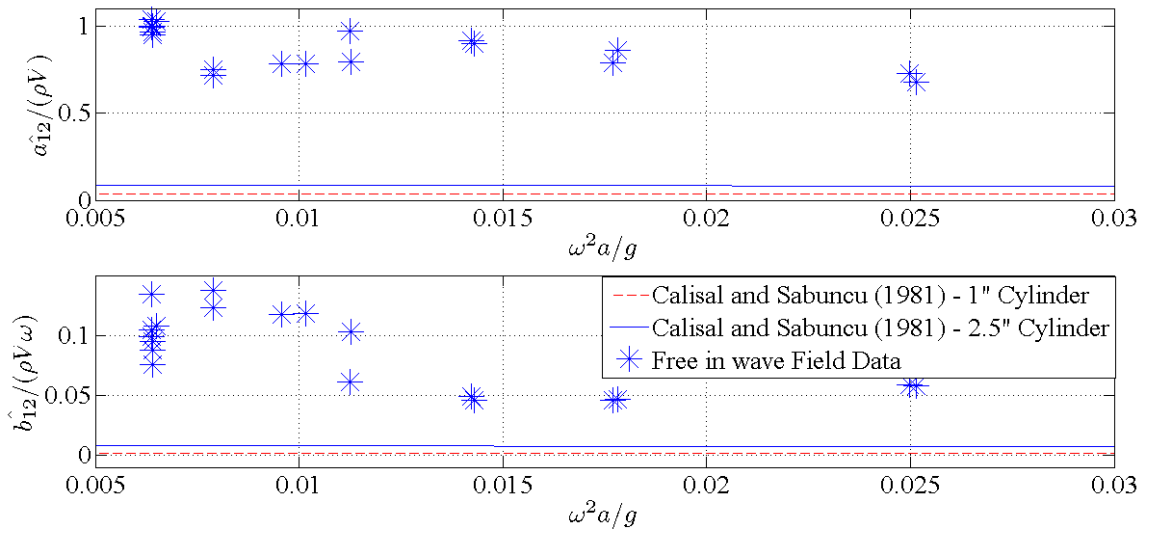


Figure 62 - Reaction Coefficients of Free Spar-Float model in Wave Field

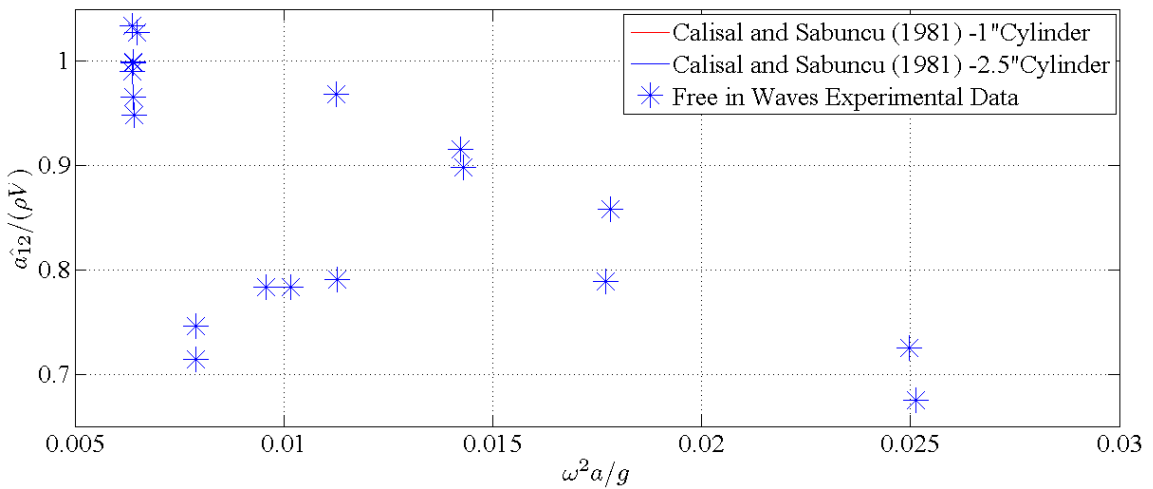


Figure 63 - Free Spar-Float in waves: Added Mass

The free experiments with the spar-float model exhibited some of the same detrimental features as found in the cylinder experiments. Steady state motion was not always achieved in the duration of the test. As with the spar-only model tests, a horizontal loading impacted the oscillation amplitudes of the spar model with the addition of bushing friction forces.

Of note, the range of coefficient values reported at some frequencies, as found in the left most cluster of data points of Figure 62 and Figure 63, demonstrates the impact of the different in wave amplitudes achieved in separate tests with a common frequency. As with the cylinder, and spar-only model, the spar-float model oscillates at an amplitude greater than that of the wave. At times the spar model amplitude was three times greater than that of the wave.

5.6 Spar-Only model to Spar-Float model Comparisons

5.6.1 Free Oscillations in Quiescent Fluid

An important component of this work is the comparison between the spar-only model, and the spar-float model configurations, which is shown in Figure 64. For both configurations the added mass appears to follow a similar decreasing trend with increasing frequency but with a market frequency offset between the two trends. The added mass is also slightly higher for the spar-only model, whereas the damping coefficient is higher for the spar-float model. Both the damped and natural frequencies of the spar-float model were slightly higher than those found in the spar-only model tests.

In contrast to the added mass the trends of the damping coefficient do not appear to align, as the spar-only model configuration does not appear to follow a trend, whereas the spar-float model configuration is like the added mass, and maintains a decreasing damping coefficient with increasing frequency. From Figure 64 we can see that the interaction of the float with the spar should not be neglected or ignored in the estimation of the hydrodynamic coefficients.

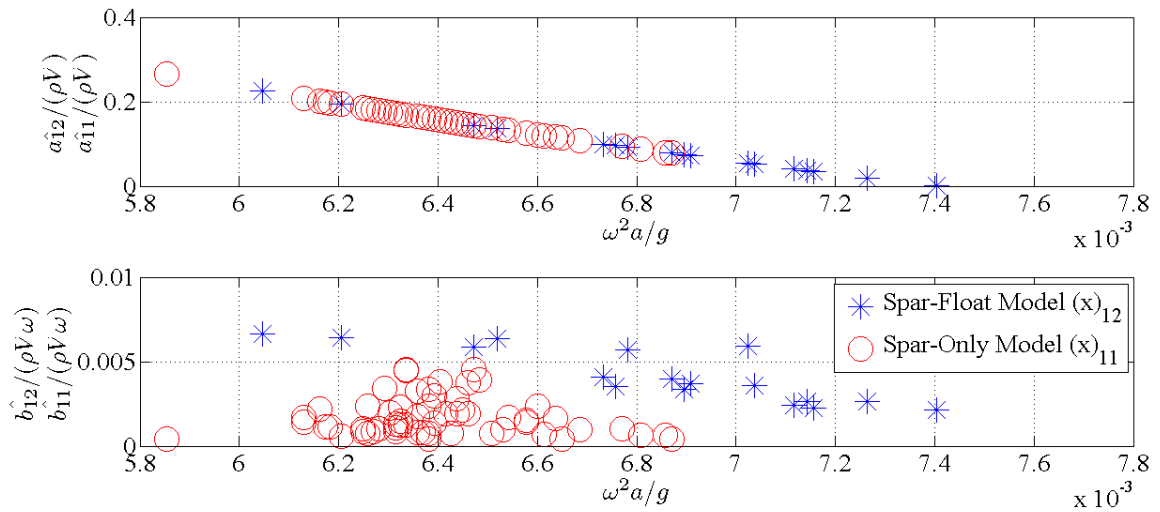


Figure 64 - Hydrodynamic Coefficients for Spar-only model and Spar-float model configurations for free, naturally damped system in Quiescent Fluid

5.6.2 Forced Oscillations in Quiescent Fluid

For the forced oscillations in quiescent fluid, the comparison between the spar-only model configuration and the spar-float model configurations is shown in Figure 65. Both models maintain a similar parabolic like trend as frequency increases, where the added mass is increasing, and the damping coefficient is decreasing. The spar-float model has a slightly lower added mass coefficient, while the damping coefficient is mostly lower than the spar-only model. At higher frequencies the asymptote may be found to be the same.

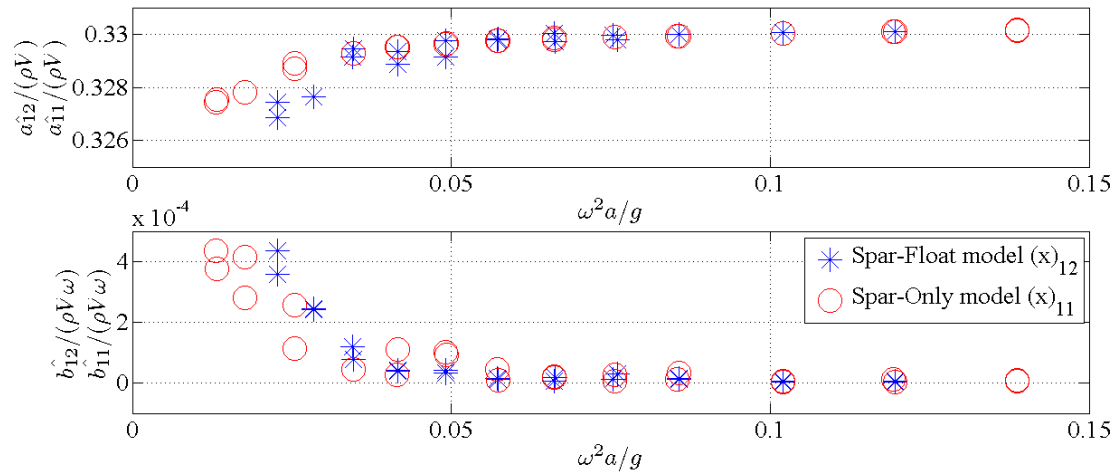


Figure 65 - Hydrodynamic Coefficients for Spar-only model and Spar-float model configurations for forced model in Quiescent Fluid

5.6.3 Fixed Model in Wave Field

For the fixed models in a wave field, the comparison between the spar-only model configuration and the spar-float model configuration is shown in Figure 66.

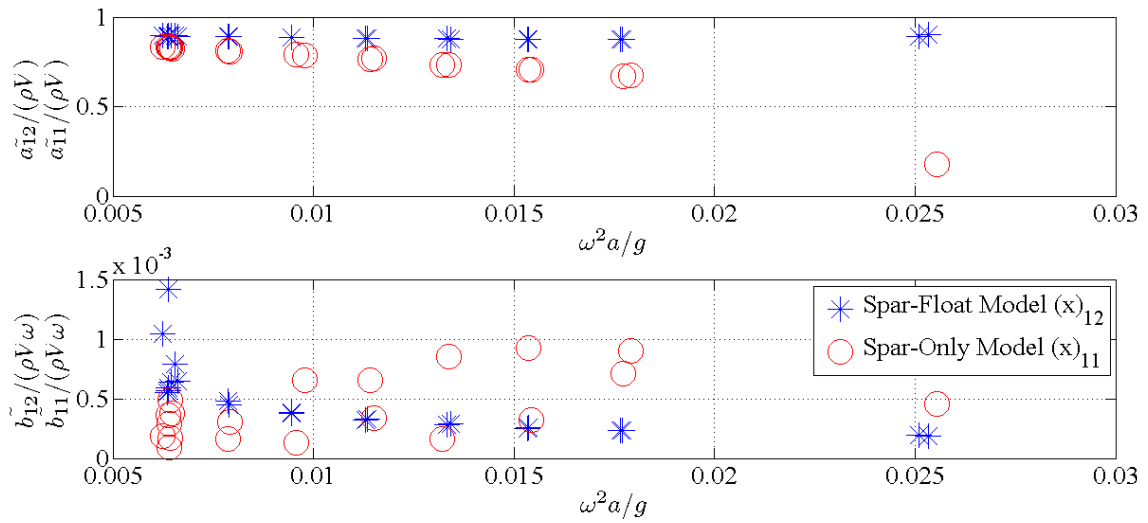


Figure 66 - Hydrodynamic Coefficients for Spar-only model and Spar-float model configurations for fixed model in Wave Field

The excitation added mass appears to be higher with a slightly decreasing trend for the spar-float model configuration in comparison to the spar-only model configuration with a steeper slope decrease with increasing frequency. However, the excitation damping coefficient appears to be lower for the spar-float model configuration at the higher frequencies but lower in the lower frequencies. The damping coefficients have a reverse trend, the spar-only model increases while the spar-float model decreases with increasing frequency.

5.6.4 Free Model in Wave Field

For the free models in a wave field, the comparison between the spar-only model configuration and the spar-float model configuration is shown in Figure 67.

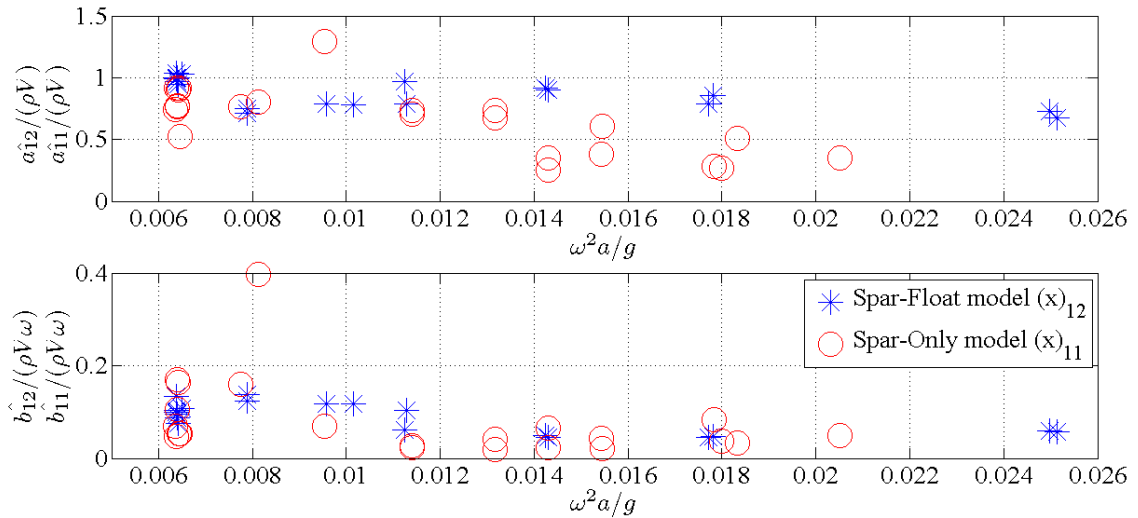


Figure 67 - Hydrodynamic Coefficients for Spar-only model and Spar-float model configurations for Free body tests in Wave Field

The added mass appears to be lower with an indiscernible trend for the spar-only model configuration in comparison to the spar-float model configuration. The damping coefficient appears to be higher for the spar-float model configuration, again with a relatively indiscernible trend. As discussed in §5.4.4 and §5.5.4, some experimental disturbances were noted, and the data points may be representative of some of these errors as a result.

As mentioned in §5.4.4, it should be noted that the difference in frequency range is due to the oscillations of the spar either hitting the bottom of the tank as was found in some scenarios, or in that the spar no longer oscillated as the horizontal loading of the waves was higher than could be compensated by the air bushings.

5.7 Reaction Force Comparison: Forced in Quiescent Fluid vs. Free in Wave Field

Comparison is made between the results of the forced oscillation experimental setup for the reactive forces and the free model in wave field experimental setup for the reactive forces. The cylinder configuration results are shown in Figure 68, the spar-only model

configuration results are shown in Figure 69 and the spar-float model configuration results are shown in Figure 70. The comparison between all three geometries shows varying degrees of separation, and disagreement between results. Since the reaction coefficient data generated in the forced model in quiescent water tests showed clean trends, and relatively little noise between successive data points in Figure 65, the reactive coefficients are presumed to be the more accurate data set. As the methodology behind resolving the reactive forces in a wave field also requires an input of excitation coefficients calculated from a separate experiment, it is difficult to determine if the difference between the quiescent fluid and generated wave tests is a result of errors within the excitation methodology, or due to the free motion of the oscillating body in the wave field. It is noted that the motion often did not reach steady state in many of the tests, as well as the number of other experimental issues discussed in §5.3.4.

Some of the differences can be contributed to the fact that the forced oscillations were set at a consistent displacement throughout the trials, whereas the wave experiments were attempted to be at consistent wave amplitude, and resulted in a variety of body oscillation amplitudes. Investigation into the effect of amplitude of body oscillation was not a specific goal of this research and was not investigated further.

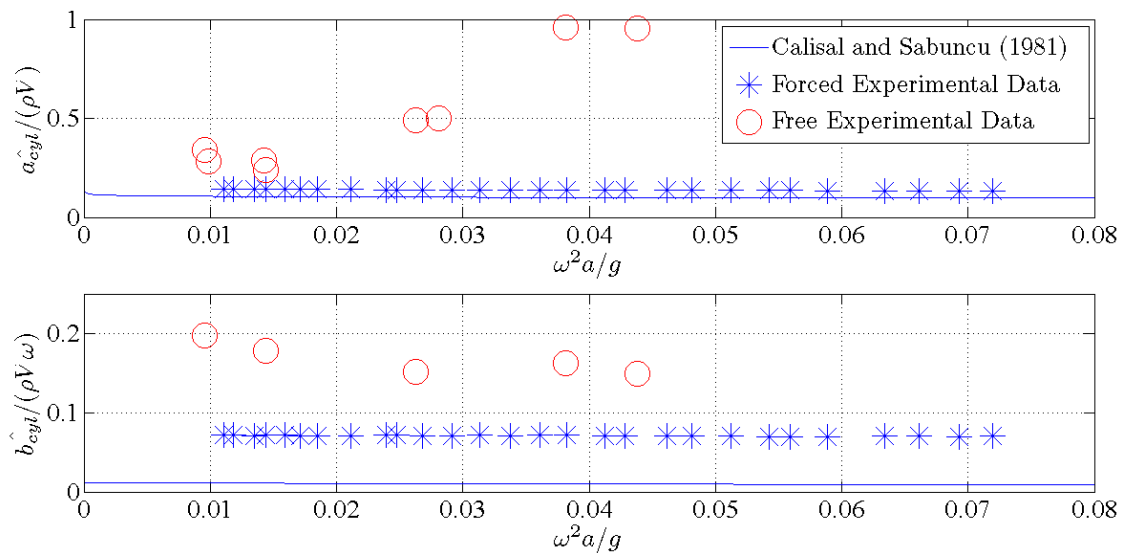


Figure 68 – Reactive Hydrodynamic Coefficients of Cylinder, comparison between forced and free in wave field tests

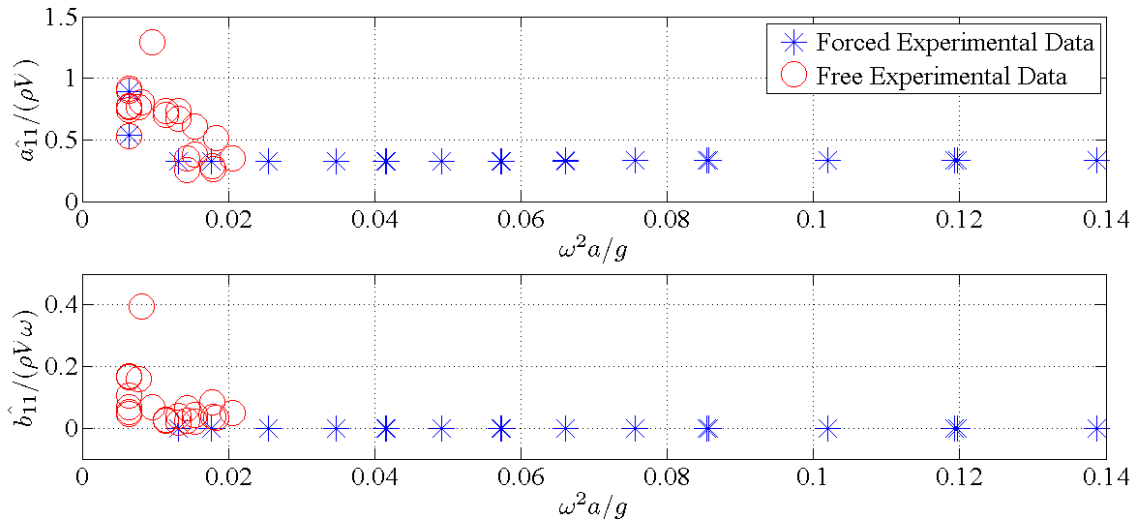


Figure 69 – Reactive Hydrodynamic Coefficients of Spar-only model, comparison between forced and free in wave field tests

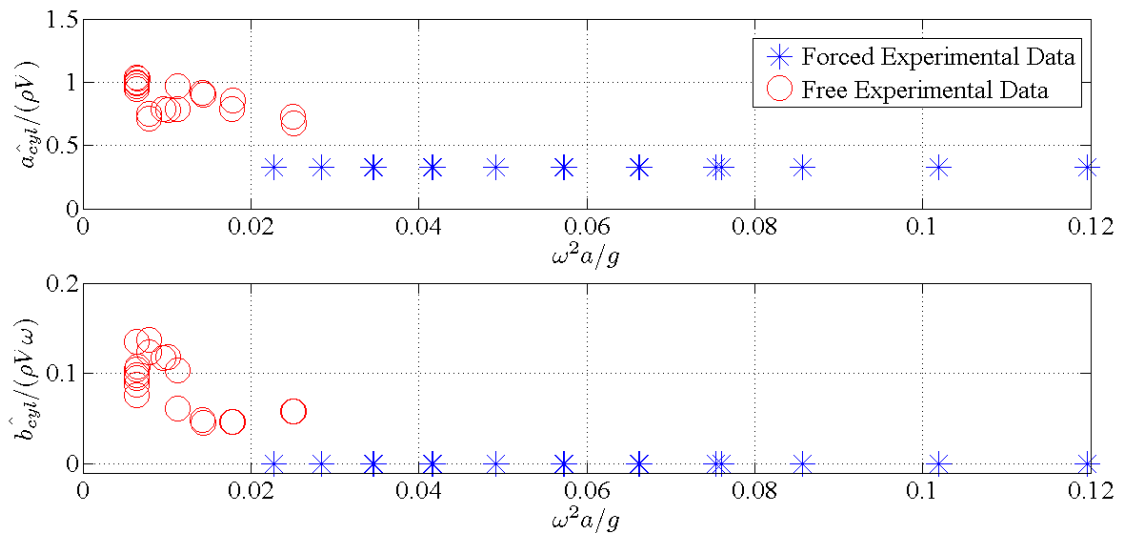


Figure 70 – Reactive Hydrodynamic Coefficient of Spar with float, comparison between forced and free in wave field tests

The comparison between the forced oscillations and the wave field test setups shows the importance of the wave field versus a strictly forced determination of hydrodynamic coefficients as it represents the more realistic body oscillations created by a wave field in particular for a multi-body system. However, it is noted that further investigation is

required on the body oscillation amplitude versus the applied wave field in order to determine the appropriate trending of the coefficients with respect to frequency.

Chapter 6: Conclusions and Recommendations

The series of experiments performed were multipurpose; to develop a testing facility for initial small scale experiments, and to obtain an initial understanding of the hydrodynamic coefficients of the selected wave energy converter geometry. There are a number of issues that were identified and would be of benefit to the development of the testing facility as well as the characterization of hydrodynamic coefficients.

6.1 Test Setup

6.1.1 Wave Maker Operation

A wave making facility was developed and it was found that the test facility although for extremely small scale, was found to have reasonable results worthy of evaluation over a frequency range, although it is necessary to understand the operating range and limitations of the individual scaled models utilized. The piston wave maker was successful in developing reasonably sinusoidal waves with simple programming, and no wave reflection was recorded or observed in the time scale of the experiments.

6.1.2 Model Guides and Forcing Mechanism

The utilization of the torsional load cell with a moment arm to magnify heave forces is key to the operation of the test facility as the forces generated are extremely small scale. It was found that in some cases, the magnification or moment arm could have been increased, as there was a limited frequency range for some models due to the forces not being within the range of the load cell.

The use of air bushings is significant in that it reduces the friction forces of the linear guide system. Although, further investigation may find that there may be some residual friction forces remaining, due to the inability to achieve the desired system pressure of 60-100psi. By increasing the number of linear guides and air bushings, it may be

possible to observe further data points in the wave field that were not able to be achieved due to high horizontal loading.

The four experimental procedures utilizing a simple cylinder were found to agree with the numerical model of Calisal and Sabuncu insofar as the data collected in this work was within the error observed between the model of [25] and other independently acquired experimental data. The experimental apparatus can be assumed to be sufficient to be utilized to determine hydrodynamic of various scaled models, in free oscillation, in simple forcing, or wave field experiments.

One of the drawbacks of the experimental setup was the use of separate computers and programs to operate the wave maker and various data collection requirements for wave field, forces, and body displacement. This required the alignment of the datasets manually as the starting points of the various data sets were not automatically time synchronized. It is recommended that in future work a LabView program is developed that can control the wave maker and record the multiple data sets in one single program thread as this will ensure a common datum for the time series.

It would be beneficial to future researchers to develop a Wave Height/Frequency and Wave maker Stroke lookup table for ease of consistent wave generation. Although the theoretical model in Table 15 for the stroke requirements is available, an accurate table for this specific wave maker will be beneficial to maintain a more consistent wave height for a range of frequencies.

Although functional, the VisualEyz 3D camera was found to be in excess of the displacement measurement requirements as the program generated data that required conversion to a Matlab program which proved time consuming. As only the heave motion of the models (a single degree of freedom) was required to be measured, another simpler transducer would be recommended. The VisualEyz will be useful for future work that investigates pitch, roll or any combination of the degrees of motion applicable to floating point absorbers, but it is overkill for a single degree of motion analysis.

The test facility validation was conducted with only one cylinder size, this does not generate a broad range of comparison for small scale, and it is recommended to consider varying cylinder diameters and depths analogous to those shown in [25] and those from other experimental facilities for a broader comparison. In order to utilize shallower or smaller diameter cylinders, a lighter guide system will be required; this can be done with the simple redesign of the guide system to accommodate, as this size to buoyancy condition was not considered during the initial design phase.

The extension arm connection components were made up of a combination of bolted components that were disconnected and reassembled a number of times while the test facility was utilized by other researchers. In order to remove any possible side effects from the assembly and disassembly of the extension arms, a single component extension arm should resolve any discrepancies found if required for future work.

6.1.3 Validation of Facility and Experimental Methods

The facility was validated with the use of a simple cylinder for all four experimental methods. The simple cylinders hydrodynamic coefficients were found to be in reasonable agreement with the theoretical model for reactive coefficients developed by Sabuncu and Calisal in [25] and similar trends were observed between the experimental data collected in this work and the model based predictions. It must be noted that ideal match up was not expected as such match up was not seen in comparisons of the theoretical model to other experimental data in [25]. The model of [25] is used here as it is one of the very few that are discussed in the literature and it was available for use in the current work.

Both the experimentally determined reactive added mass and damping coefficients are found to be higher than the theoretical model. This observation was corroborated by independently acquired experimental data as presented in [25]. The experimentally determined excitation loading is found to be higher than the theoretical model for both the added mass and damping coefficients as well.

6.2 Hydrodynamic Coefficients of Point Absorbing Wave Energy Converter Model Geometry

A first run of experiments was conducted for the selected WEC geometry in order to determine the linear lumped parameter hydrodynamics for both the spar-only and spar-float models. The experimental data was compared to the existing numerical model from [25] for the hydrodynamics of a simple cylinder in order to determine the suitability of existing numerical models such as [25] for the WEC spar hydrodynamics.

The experiments have proven that the theoretical model for a simple cylinder is not suitable for use for a complex geometry such as the WEC spar and spar-float combinations.

The selected point absorbing WEC spar geometry was found to have an increase in added mass and a decrease in damping coefficients with an increase in frequency for the forced reactive experimental method. When in comparison to the theoretical model of [25] the coefficients were significantly higher for added mass, and lower for damping than for a simple cylinder of either 1” or 2.5” diameters. The addition of the float showed very little difference in higher frequencies, but a higher added mass and lower damping coefficients at the lower frequencies in the forced reactive experiments.

The excitation experiments showed that the added mass of both the spar-only and spar-float models decreased with increasing frequency, but the spar-only model added mass was higher over the range of frequencies tested. The damping coefficient maintained differing trends between spar-only and spar-float models, one decreasing, the other increasing respectively, with the spar-float model being higher at the lower frequencies, but lower at the higher frequencies.

The comparison of reactive hydrodynamic coefficients as determined in the forced and the free model in generated wave experiments did not follow any particular trend between cylinder, spar-only model and spar-float model configurations. As the wave

field experiments did not have a significant number of useable data points, this particular comparison would benefit from further development of the wave experiments including a better understanding of the body motions and therefore constraints to the systems over the desired frequency and amplitude range. Therefore, in order to obtain the desired datasets, initial trials would need to be conducted in order to determine the wave frequencies and amplitudes that generate what oscillation frequency and amplitude of the selected body configuration, to be used in conjunction with forced model data; again, look up tables would be beneficial. With this preliminary data, the test can be conducted with the appropriate wave inputs to generate a consistent trend, as was not deliberated prior to this research. As some experiments did not reach steady state motion, longer trial lengths would need to be conducted.

6.3 Spar Design Considerations

The design and functionality consequences of the experimentally determined hydrodynamics are evaluated based on geometry of combined components, and over a range of frequencies.

6.3.1 Geometric Effects: Spar Versus cylinder

The reactive forcing results shown in Figure 48 for the spar-only model forced in quiescent fluid, with comparison to two cylinders of a matching diameter to the two main cross sections of the spar; the surface piercing and the lower bulb. The theory under predicts the added mass and over predicts the damping coefficients of a single cylinder of either size when compared to the complex spar designed system, where considerations are needed to be made for the hemisphere on the bottom of the spar, and the 45° taper between cylinder steps.

The comparison of the spar-only model against a single cylinder model of a size in conjunction with the spar body leads to the conclusion that a simplified model of a

single cylinder cannot be used in place of a more complex theoretical model or experimental results for a complex shape such as the spar.

6.3.2 Geometric Effects: Combination of spar and float

The effect on added mass and damping coefficients by adding the float are found to differ depending on the forced reactive loading arrangement and the wave excitation arrangements. Figure 64 through Figure 67 show the comparisons between the different experimental methods and the spar-only and the spar-float model configurations.

The reactive added mass coefficients follow a similar parabolic trend for both models and converge at the higher frequencies, where at the lower frequencies the spar-only model has a higher added mass. The reactive damping coefficient again follows similar parabolic trends converging at the higher frequencies, but the spar-float model is higher at the lower frequencies.

The excitation added mass appears to be higher with a slightly decreasing trend for the spar-float model configuration in comparison to the spar-only model configuration with a steeper slope decrease with increasing frequency. However, the excitation damping coefficient appears to be lower for the spar-float model configuration at the higher frequencies but lower in the lower frequencies. The damping coefficients have a reverse trend, the spar-only model increases while the spar-float model decreases with increasing frequency.

The comparison of the spar-only model against a spar-float model leads to the conclusion that the spar-only model should not be used without a more complex theoretical model or experimental results for the combined effects of the presence of the float. Further work will need to be conducted for both excitation and reaction forces to include the motion of the float as it will absorb some of the wave loading forces as well as generate waves of its own, respectively.

6.3.3 Frequency and Amplitude Effects

It is visible in all experiments that frequency does impact the resulting hydrodynamic coefficient. In the reactive, forced in quiescent fluid experiments the frequency trends are parabolic in nature. The excitation wave loaded experiment coefficients appear linear but differ from increasing and decreasing depending on the model type and the coefficient.

It was found that the hydrodynamic coefficients were also impacted by differing wave heights. This was not investigated in depth as it was not a primary goal of this work, but should be considered in future work. The excitation added mass coefficient increases with wave height, whereas the excitation damping coefficient decreases with wave height.

Changes in the point absorber geometry can be evaluated in future work in order to optimize the hydrodynamic forces. A redesign of the float, with new buoyant materials would allow further investigation into the effect on the 2-DOF system when both bodies are allowed to oscillate. Further experimentation could include a combination of linear air bearings to be incorporated in order to evaluate the hydrodynamic coefficients for a combination of modes of motion, including pitch.

The hydrodynamic coefficients of the point absorbing wave energy converter under investigation does require experimental evaluation as the design is further developed and improved upon due to its unique geometry. The addition of the float to the spar is found to impact the overall hydrodynamic coefficients, and differently between the reactive and excitation methodologies: forced in quiescent fluid and free wave field experiments. The wave field experiments are the more realistic evaluation and therefore contain the more appropriate data sets, however the data sets developed did not contain consistent inputs and contained some detrimental errors, and therefore the output cannot be used to compare trends. As the geometry of the WEC is refined, future tests should be conducted with the test setup recommendations previously listed, in order to obtain

the hydrodynamic coefficient profiles over the desired frequency ranges and wave amplitude ranges.

Bibliography

- [1] "<http://www.iea.org/textbase/nppdf/free/2006/weo2006.pdf> accessed 15/01/2012".
- [2] "<http://nrtee-trnee.ca/wp-content/uploads/2011/08/Getting-to-2050-low-res.pdf> accessed 15/01/2012".
- [3] G. Timilsina, D. Czamanski and J. Prince, "Renewable Energy Technology in Canada: Current Status and Future Projects," Canadian Energy Research Institute, 2005.
- [4] "http://www.oregonwave.org/wp-content/uploads/Task-4.3.2-EPRI-WaveWatch-III-Review_Implementation-Plan.pdf accessed 15/01/12".
- [5] "<http://nrtee-trnee.ca/wp-content/uploads/2011/06/Energy-Based-Carbon-Emissions-FullReport-eng.pdf>".
- [6] A. Muetze and J. G. Vining, "Ocean Wave Energy Conversion – A Survey," *IEEE*, vol. 00, no. December, pp. 1410-1417, 2006.
- [7] M. French, "On the difficulty of inventing an economical sea wave," *Proc. IMechE*, vol. 220, no. Part M: J. Engineering for the Maritime Environment, pp. 149-155, 2006.
- [8] R. Aggidis, V. Chaplin and A. George, "An Investigation into Power from Pitch-Surge Point-Absorber Wave Energy Converters," *IEEE, Clean Electrical Power*, no. 21-23 May 2007, pp. 520 - 525, 2007.
- [9] J. Falnes, "Optimum control of oscillation of wave-energy converters, 1993. "Annex Report B1: Device fundamentals/Hydrodynamics", an annex to the main

report "Wave Energy Converters: Generic Technical Evaluation Study".

- [10] S. Salter, J. Taylor and a. N. Caldwell, "Power conversion mechanisms for wave energy.," *Proc. IMechE*, vol. 216, no. Part M: Journal of Engineering for the Maritime Environment, pp. 1-27, 2002.
- [11] G. Bacelli, J. Ringwood and J. Gilloteaux, "A control system for a self-reacting point absorber wave energy converter subject to constraints," Milano Italy, 2011.
- [12] P. Ricci, J. Lopez, M. Santos, J. L. Villate, P. Ruiz-Minguela, F. Salcedo and A. F. de Falcão, "Control Strategies for a simple Point-Absorber Connected to a Hydraulic Power Take-off," Uppsala, Sweden, 2009.
- [13] K. Schlemmer, F. Fuchshumer, N. Böhmer, R. Costello and C. Villegas, "Design and Control of a Hydraulic Power Take-off for an Axi-symmetric Heaving Point Absorber," Southampton, UK, 2011.
- [14] S. Beatty, Analysis and Development of a Three Body Heaving Wave Energy Converter, Victoria BC: M.A.Sc. Thesis, University of Victoria, 2009.
- [15] R. Dean and R. Dalrymple, "Water Wave Mechanics for Engineers and Scientists," Englewood Cliffs, New Jersey, Prentice-Hall, 1991.
- [16] J. Newman, Marine Hydrodynamics, Cambridge: The MIT Press, 1977.
- [17] T. Falnes and D. Bjarte-Larsson, "Long-Wavelength Approximation of Wave Force on Two-Body Axisymmetric System," Trondheim, Norway, 2001.
- [18] O. Kalen, A study of the change in the wave field due to the presence of wave energy converters, Gothenburg: University of Gothenburg, 2010.
- [19] G. De Backer, M. Vantorre, R. Banasiak, C. Beels and J. De Rouck, "Numerical Modelling of Wave Energy Absorption by a Floating Point Absorber System," in

Proceedings of 17th International Offshore and Polar, Portugal, 2007.

- [20] T. Soulard, M. Alves and A. Sarmento, "Force Reacting Principle Applied to Heave Point Absorber Wave Energy Converter," in *Proceedings of the 19th International Offshore and Polar Engineering Conference*, Osaka, Japan, 2009.
- [21] M. Vantorre, R. Banasiakb and R. Verhoevenb, "Modelling of hydraulic performance and wave energy extraction," *Applied Ocean Research* 26, p. 61–72, 2004.
- [22] M. Bhinder, C. G. Mingham, D. M. Causon, M. T. Rahmati, G. A. Aggidis and R. V. Chaplin, "A Joint Numerical and Experimental Study of a Surging Point Absorber," in *Proceedings of the ASME 28th International Conference on Ocean, Offshore and Arctic Engineering*, Honolulu, Hawaii, 2009.
- [23] Z. Hu, D. M. Causon, C. G. Mingham and L. Qian, "Numerical Wave Tank Study of a Wave Energy Converter in Heave," in *Proceedings of the 19th International Offshore and Polar Engineering Conference*, Osaka, Japan, 2009.
- [24] R. Yeung, "Added mass and damping of a vertical cylinder in finite depth waters.," *Applied Ocean*, vol. 3, pp. 119-133, 1981.
- [25] T. Sabuncu and S. Calisa, "Hydrodynamic Coefficients for Vertical Cylinder," *Ocean Engng.*, vol. 8, pp. 25-63, 1981.
- [26] S. Calisal and T. Sabuncu, "Hydrodynamic Coefficients for Vertical Composite Cylinders," *Ocean Engng*, vol. 11, no. 5, pp. 529-542, 1984.
- [27] S. Calisal and T. Sabuncu, "A Generalized Method For the Calculation of Hydrodynamic Forces on Discontinuous Vertical Cylinders," *Ocean Engng*, vol. 20, no. 1, pp. 1-18, 1993.

- [28] J. Calisal and S. M. Mikkelsen, "An Experimental Study of the Hydrodynamics of Cylindrical Structures," *Marine Structures*, vol. 6, pp. 259-277, 1993.
- [29] S. Mavrakos, "Hydrodynamic Characteristics of Floating Toroidal Bodies," *Ocean Engng*, vol. 24, no. 4, pp. 381-299, 1997.
- [30] J. Mercier, "Hydrodynamic Forces on Some Float Forms," vol. 5, no. 4, 1971.
- [31] S. Mavrakos, "Hydrodynamic coefficients in heave of two concentric surface-piercing truncated circular cylinders," *Applied Ocean Research*, vol. 26, p. 84-97, 2004.
- [32] K. Ruehl, Time-Domain Modeling of Heaving Point Absorber Wave Energy Converters, Including Power Take-O, Corvallis, OR: Oregon State University, 2011.
- [33] M. Eriksson, J. Isberg and M. Leijon, "Theory and Experiment on an Elastically Moored Cylindrical Buoy," vol. 31, no. 4, 2006.
- [34] C. Villegas and H. van der Schaaf, "Implementation of a Pitch Stability Control for a Wave Energy Converter," in *The European Wave and Tidal Energy Conference*, South Hampton UK, 2011.
- [35] S. Beatty, B. Buckham and P. Wild, "Modeling, Design and Testing of a Two-Body Heaving," 2007.
- [36] R. Bracewell, Frog and ps frog: a study of two reactionless ocean wave energy converters, PhD Thesis, Lancaster: Lancaster Univeristy, 1990.
- [37] G. De Backer, M. Vantorre, K. De Beule, C. Beels and J. De Rouck, "Experimental Investigation of the Validity of Linear Theory to Assess the Behaviour of a Heaving Point Absorber at the Belgian Continental Shelf,"

Honolulu, Hawaii, USA, 2009.

- [38] J. Cruz, M. Rea, A. Sarmiento, G. Thomas and R. Henderson, *Ocean Wave Energy: Current Status and Future Perspectives*, Bristol, UK: Springer Berlin Heidelberg, 2006.
- [39] R. Sorensen, *Basic Wave Mechanics for Coastal and Ocean Engineers*, Lehigh University: Wiley-Interscience, 1993.
- [40] C. Hiles, *On the Use of Computational Models for Wave Climate Assessment in Support of the Wave Energy Industry*, Victoria: M.A.Sc. Thesis, University of Victoria, 2010.
- [41] S. Beatty, C. Hiles, R. Nicoll, J. Adamson and B. Buckham, "Design synthesis of a wave energy converter," 2009.
- [42] G. Payne, "Guidance for the experimental tank testing of wave energy converters," University of Edinburgh, Edinburgh, 2008.
- [43] M. Tasuno and P. Bearman, "A visual study of the flow around an oscillating circular cylinder at low Keulegan-Carpenter numbers and low Stokes numbers," *Journal of Fluid Mechanics*, vol. 211, pp. 157-182, 1990.
- [44] J. O'Kane, A. Troesch and K. Thiagarajan, "Hull component interaction and scaling for TLP hydrodynamic coefficients," vol. 29, 2002.
- [45] O. Madsen, "On the Generation of Long Waves," *Journal of Geophysical Research*, vol. 76, no. 36, pp. 8672-8683, 1971.
- [46] E. F. G. v. Daalen, *Numerical and theoretical studies of water waves and floating bodies*, Amsterdam: Ph.D Dissertation, 1993.

- [47] M. McCormick and D. Kraemer, "Long-wave Approximations of the added-mass and radiation damping of a heaving, vertical, circular, cylindrical in waters of finite depth," *Maritime Emergency Management: The Journal of Ocean Technology*, vol. 1, no. 2, pp. 58-66, 2006.
- [48] "http://oreg.ca/web_documents/oreg_the_role_of_fits.pdf".
- [49] R. Taghipour, *Efficient Prediction of Dynamic Response for Flexible and Multi-Body Marine Structures*, Trondheim: Norwegian University of Science and Technology, 2008.
- [50] "<http://www.iea.org/textbase/nppdf/free/2006/weo2006.pdf>," [Online]. [Accessed 15 03 2012].
- [51] "<http://nrtee-trnee.ca/wp-content/uploads/2011/08/Getting-to-2050-low-res.pdf>," [Online]. [Accessed 15 01 2012].
- [52] "http://www.oregonwave.org/wp-content/uploads/Task-4.3.2-EPRI-WaveWatch-III-Review_Implementation-Plan.pdf accessed," [Online]. [Accessed 15 01 2012].
- [53] M. Vantorre, R. Banasiakb and R. Verhoeven, "Modelling of hydraulic performance and wave energy extraction by a point absorber in heave," *Applied Ocean Research*, vol. 26, pp. 61-72, 2004.
- [54] S. Joo, W. Schultz and A. Messiter, "Uniformly valid solutions to the initial-value wavemaker problem," *The University of Michigan Program in Ship Hydrodynamics*, 1989.

Appendix A

Wave Data over range of frequencies 1.6 rad/s to 6.8 rad/s

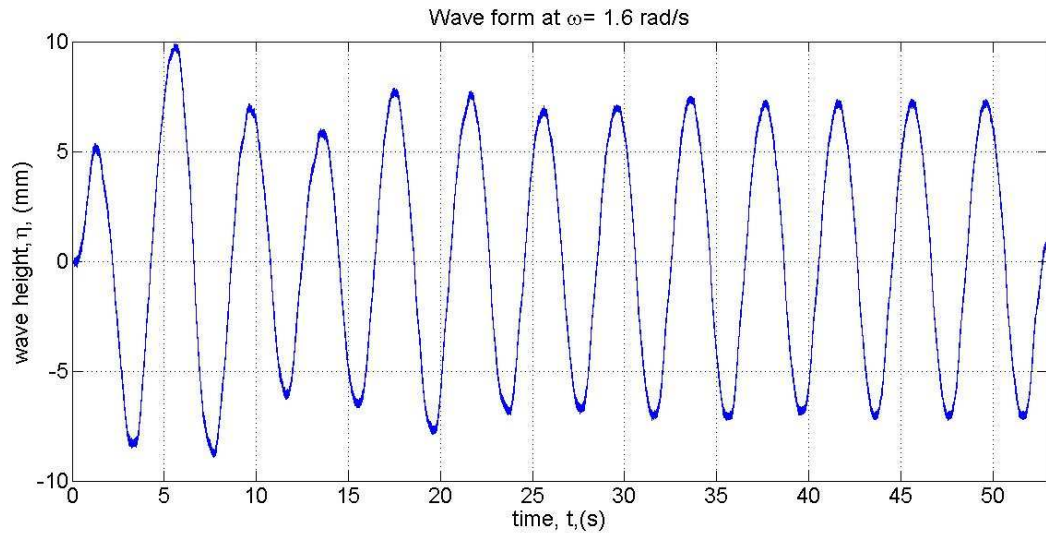


Figure 71 - Wave Form at 1.6rad/s

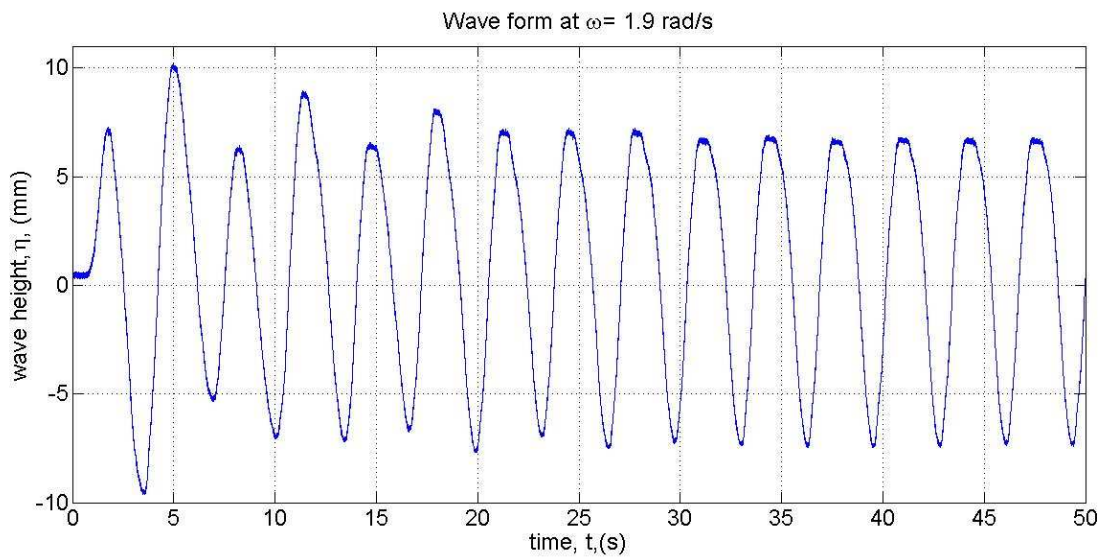


Figure 72 - Wave Form at 1.9rad/s

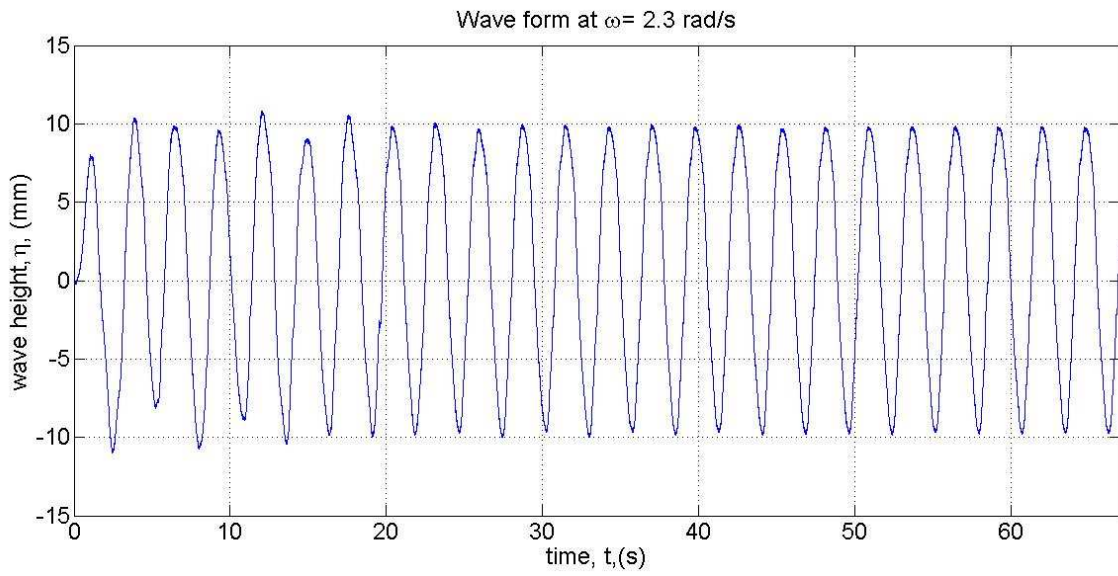


Figure 73 - Wave Form at 2.3 rad/s

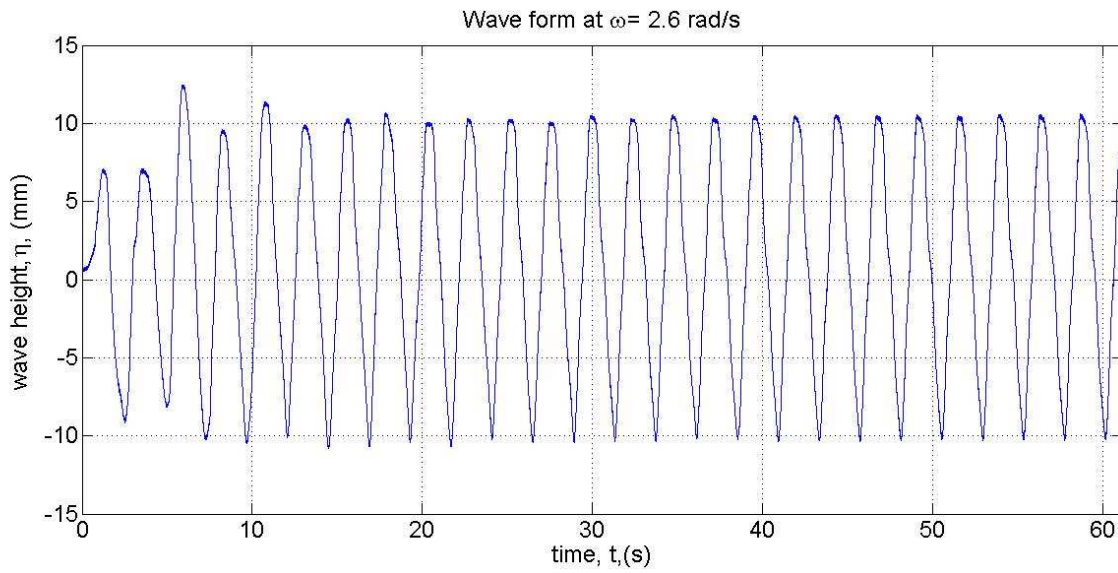


Figure 74 - Wave Form at 2.6rad/s

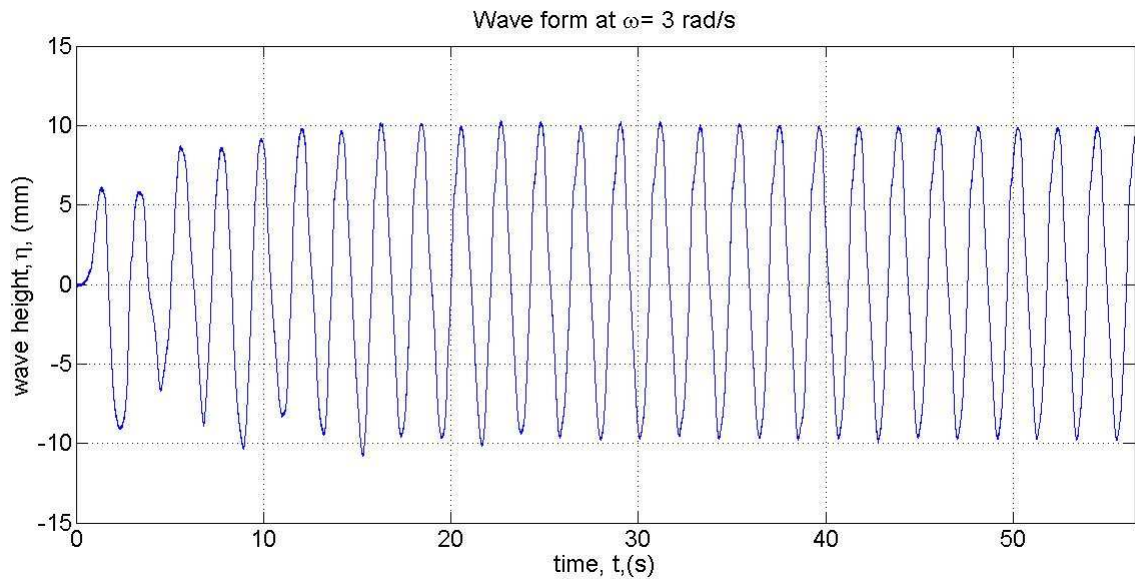


Figure 75 - Wave Form at 3.0 rad/s

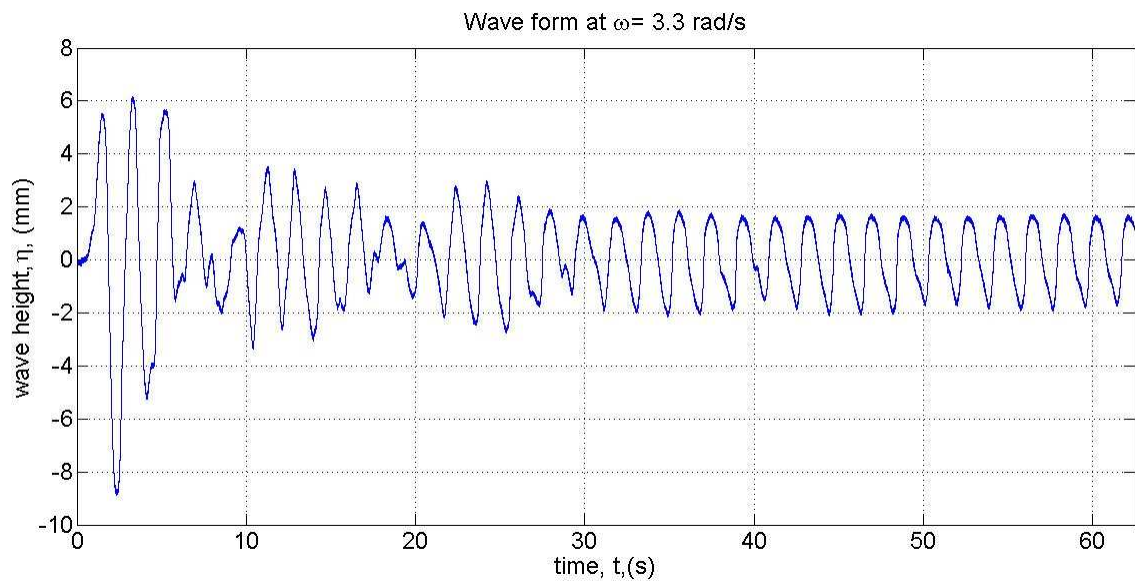


Figure 76 - Wave Form at 3.3 rad/s

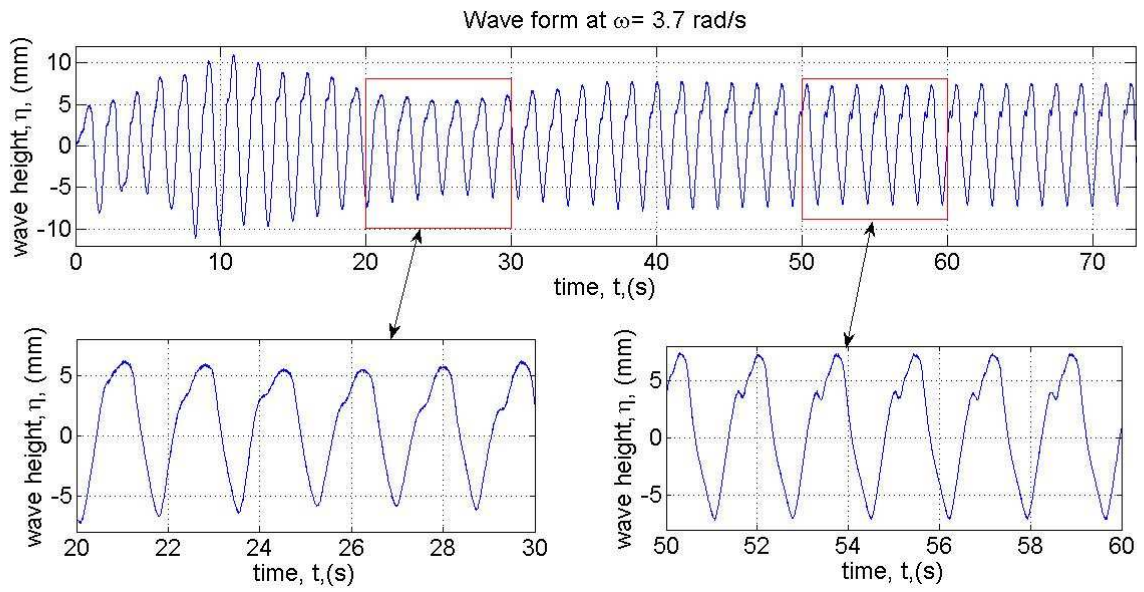


Figure 77 - Wave Form at 3.7 rad/s

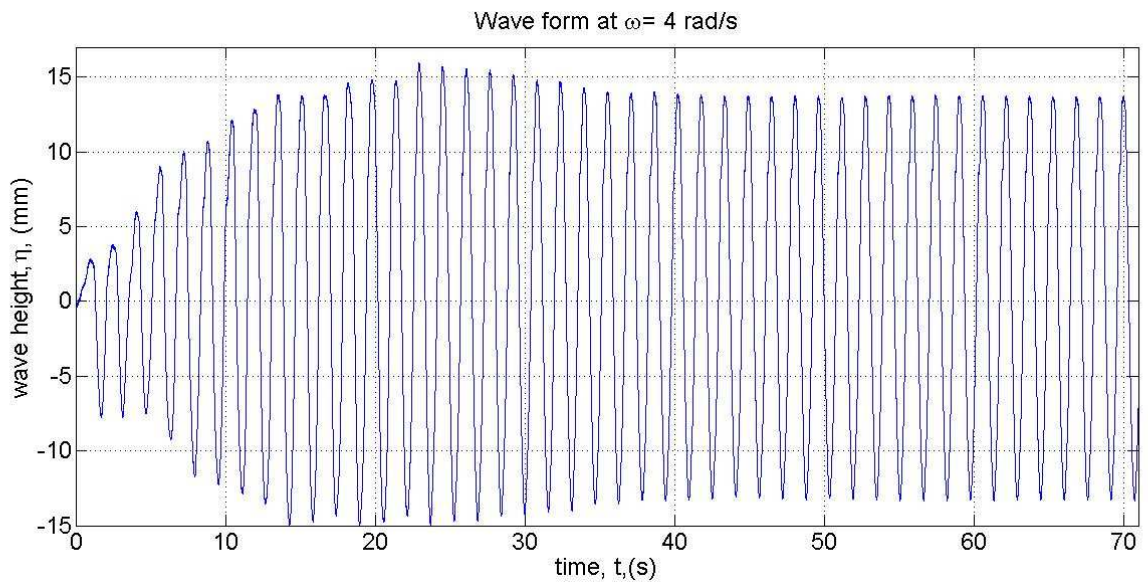


Figure 78 - Wave Form at 4.0 rad/s

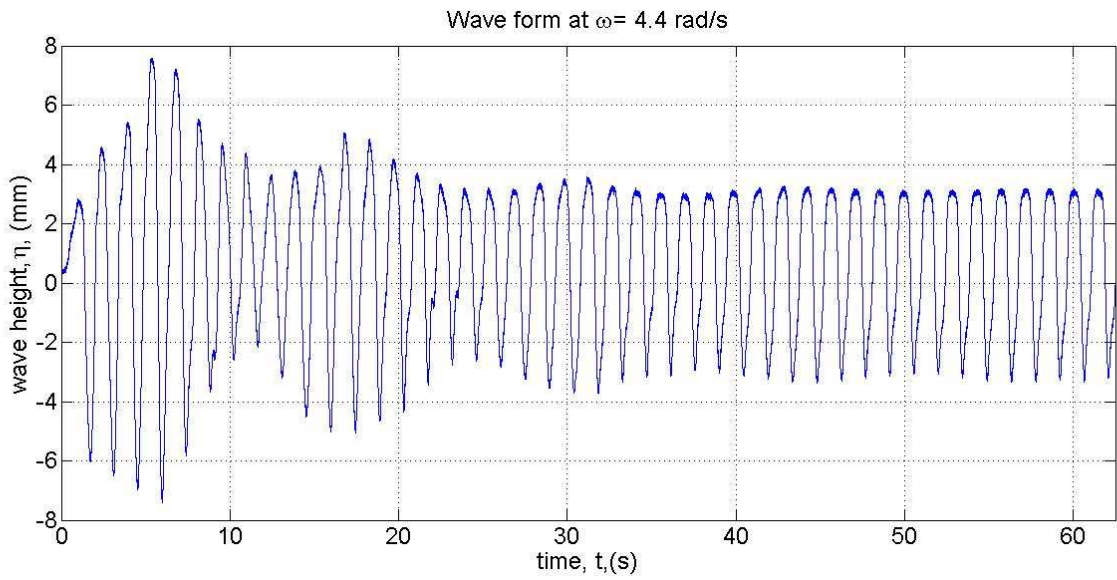


Figure 79 - Wave Form at 4.4rad/s

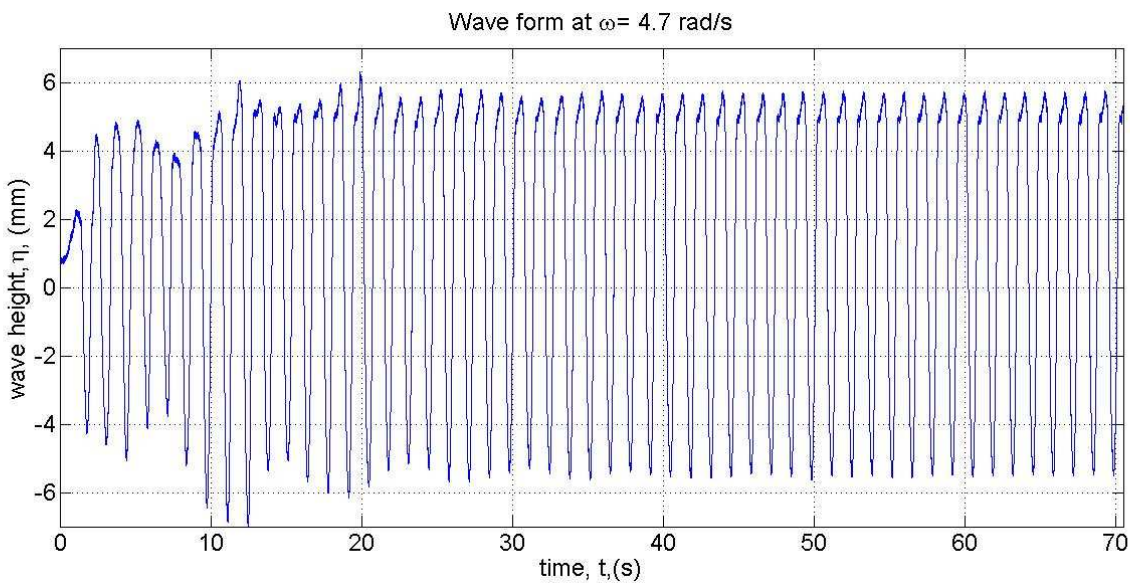


Figure 80 - Wave Form at 4.7 rad/s

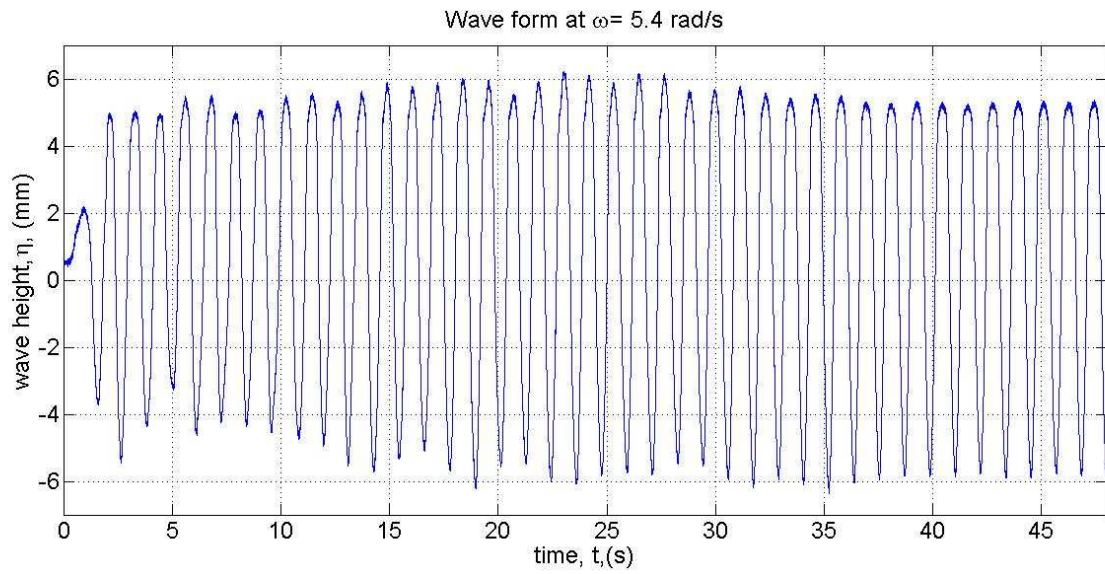


Figure 81 - Wave form at 5.4 rad/s

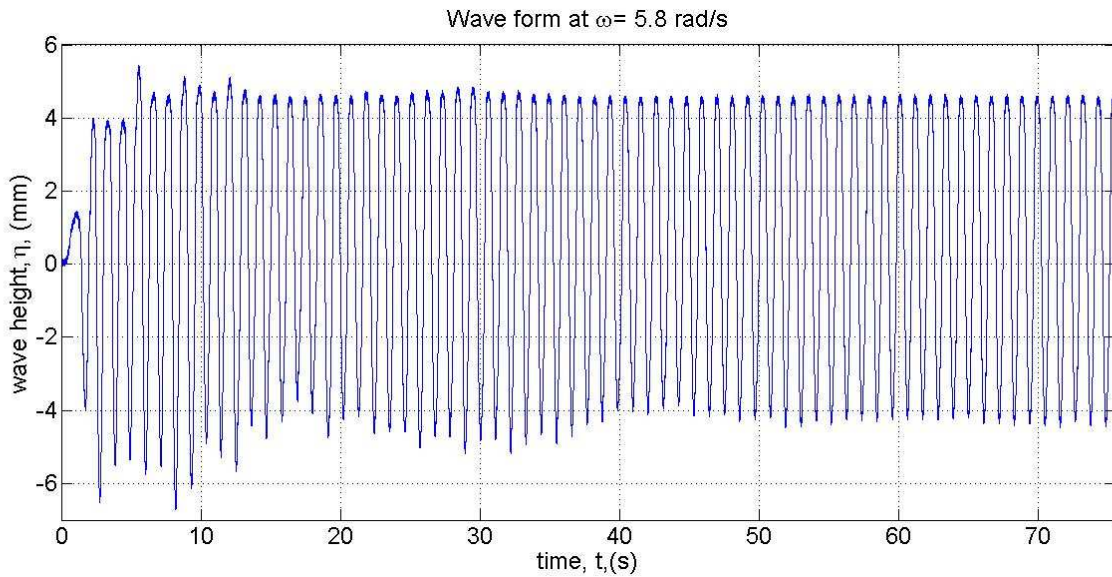


Figure 82 - Wave Form at 5.8 rad/s

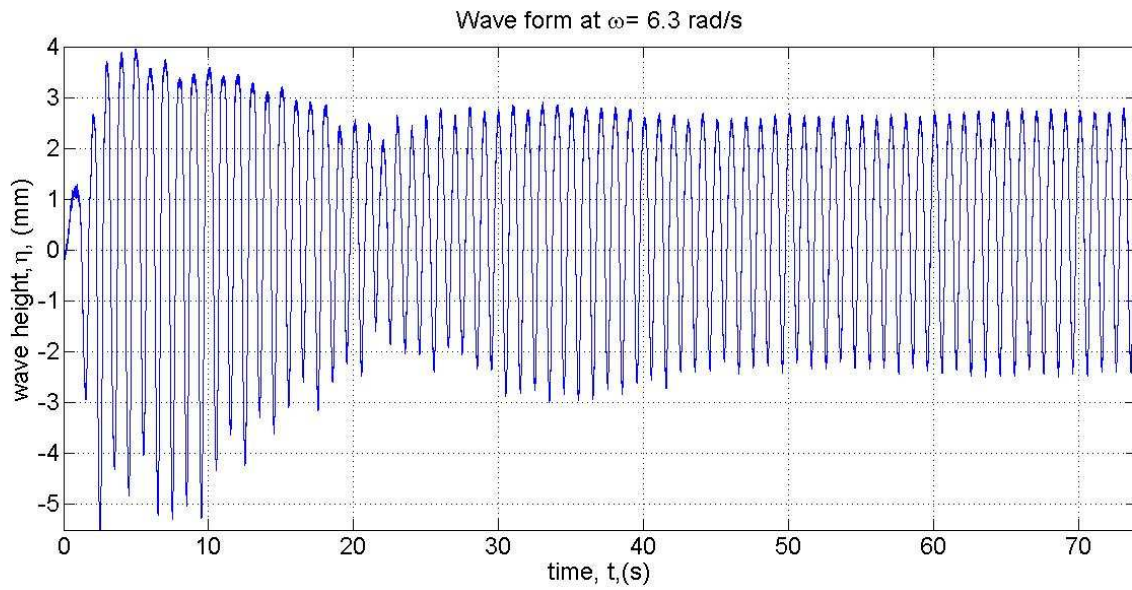


Figure 83 - Wave Form at 6.3 rad/s

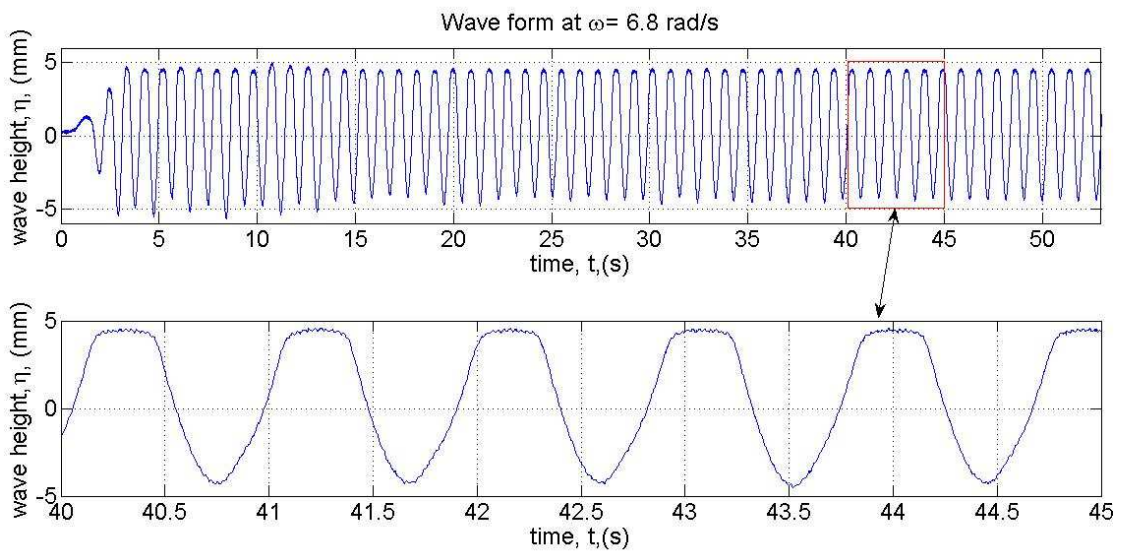


Figure 84 - Wave Form at 6.8 rad/s